WIDEBAND ELECTRICAL IMPEDANCE SPECTRO-TOMOGRAPHIC IMAGING

Manoochehr Nahvi

Submitted in accordance with the requirements
for the degree of Doctor of Philosophy

The University of Leeds
School of Electronic and Electrical Engineering

August 2008

The candidate confirms that the work submitted is his own and that appropriate credit has been given where reference has been made to the work of others.

Acknowledgements

Praise to God Almighty, the most compassionate and the most merciful.

In loving memory of my parents.

My warmest thanks goes to my project supervisor Professor B. S. Hoyle, for mentoring me throughout my years as a student. A simple acknowledgment is not enough to express the depth of my gratitude for all the patience and perseverance he has shown throughout these years. I am sincerely indebted to him for his continuous guidance, valuable advice and thoughtful discussion throughout my research. This thesis would not have been possible without his guidance and support, academically and otherwise.

I would like to thank Hossein, Mohsen, Mahdi, Reza, Nejat, Ali, Yaghoub and all the football crowd for helping me out in all the ways that they did.
I would like also to express my gratitude to David Cowell for our enlightening conversations and also I would not like to forget to thank Arif and Stephen.

I would like to express my gratitude to the Iranian Ministry of Science and Technology and the University of Guilan for providing me the scholarship to continue my study in abroad.

Lastly, to my family, for all their patience, support, understanding and love they provided me throughout these years, thank you. If not for your belief in me and the confidence you gave me, none of this would have been possible. Finally...

...to my wife Fereshteh and my sons Alireza and Shayan...

Abstract

The thesis addresses the augmentation of a conventional single frequency Electrical Impedance Tomography (EIT) system to form a wideband EIT (WEIT) system. Its contribution is to extend such systems to provide spectral information, but with the essential capability to match process dynamics. A novel method to achieve these aims is described in its key stages.

The underlying opportunity for this study is that process materials may show considerable change in their electrical properties in response to an injected signal over a wide frequency range. The use of this concept to demonstrate the construction of tomographic images for a range of frequency bands is described. These can then provide a deeper understanding and interpretation of a process under investigation.

The thesis presents an in-depth review of the characteristics of the various wideband signals that could be used for simultaneous spectral measurements. This includes an objective selection process that demonstrates that a Chirp signal form offers key advantages. It then addresses the details of the developed method and algorithms for WEIT systems that deploy a Chirp wideband excitation signal and a further aspect of the method, based on the time-frequency analysis, particularly wavelet transform, which is used to reveal spectral data sets. The method has been verified by simulation studies which are described. To provide measurements over a required frequency range a linear chirp is deployed as the excitation signal and corresponding peripheral measurements are synthesised using a 2D model. The measurements are then analysed using a wavelet transform algorithm to reveal spectral datasets which are exemplified in the thesis.

The thesis then examines the feasibility of the presented method through various experimental trials; an overview of the implementation of the electronic system is included. This provides a single-channel EIT chirp excitation implementation, in essence simulating a real-time parallel data collection system, through the use of pseudo-static tests on foodstuff materials. The experimental data were then analysed and tomographic images reconstructed using the frequency banded data. These included results illustrate the promise of this composite approach in exploiting sensitivity to variations over a wide frequency range. They indicate that the described method can augment an EIT sensing procedure to support spectroscopic analysis of the process materials.

Contents

List of Tables

List of Figures

List of Abbreviations

1-D	One Dimensional
2-D	Two Dimensional
3-D	Three Dimensional
AC	Alternating Current
ADC	Analog to Digital Converter
BW	Band Width
CWT	Continuous Wavelet Transform
DAC	Digital to Analog Converter
DC	Direct Current
DDS	Direct Digital Synthesis
DFT	Discrete Fourier Transform
EIT	Electrical Impedance Tomography
FEM	Finite Element Method
FFT	Fast Fourier Transform
$L^2(\mathbb{R})$	Finite Energy Function
MFEIT	Multi-frequency EIT
ML-PRBS	Maximum Length PRB
PRBS	Pseudo Random Binary Signal
RMS	Root Mean Square
SFEIT	Single-frequency EIT
SNR	Signal to Noise Ratio
STD	Standard Deviation

SQR	Signal to Quantisation noise Ratio
STFT	Short-Time Fourier Transform
VCCS	Voltage Controlled Current Source
WEIT	wideband EIT
WT	Wavelet Transform

Chapter 1

Introduction

Tomography techniques provide information of the internal materials distribution of a process from non-invasive measurements. Depending on the type of tomography, appropriate measurements are taken from a number of peripheral sensors [1]. They are then analysed in order to reveal process internal characteristics, for instance, by either reconstruction of cross-sectional images demonstrating a special distribution; or for the estimation of process parameters. In a simple process, one tomography technique may be able to deliver adequate information, whereas in a complex process a multi-mode system may lead to the estimation of key process parameters [2].

Electrical tomography is a type of tomography based on the electrical properties of materials. It was pioneered by medical scientists in the 1970's. This technique was then applied to process applications in the 1980's[3]. During recent years, electrical tomography has successfully moved from research to industrial applications, due to its relative simplicity, high speed, and low cost. There is growing interest in the application of electrical tomography to various industrial processes. Typical applications are pharmaceutical crystallisers [4], mixing reactions [5], separation and mixing processes, slurries measurements, gas-liquid separators, liquid-liquid flows[6], and also for real-time monitoring of pressure filters[7]. The level of interest in the application of electrical tomography is also evident from the latest World Congress on Industrial Process Tomography in

Bergen, Norway, 2007, for example, in solid-liquid suspensions[8], modelling of flow parameters [9] and study of slurry flow rate [10]. These examples show that electrical tomography has the capability of enhancing the understanding and interpretation of a wide range of target processes.

1.1 Motivation for this Research

A member of the electrical tomography family is electrical impedance tomography (EIT) which is suitable for the imaging of predominataly conductive processes, whereby various patterns of alternating current of a given frequency can be passed through the subject. A conventional single-frequency EIT system provides an estimate of the location of materials within an application space based upon conductivity contrast. A further major interest in many applications is the identification and characterisation of materials. A single-frequency EIT system can not fulfil this requirement but, in contrast, it may be realised through a multi-frequency EIT (MFEIT). This approach assumes, however, that materials may exhibit significant conductivity variation over some frequency range. It has been exploited in medical research for the characterization of human tissue, and also for the diagnosis of particular diseases using electrical properties, for instance, bioelectrical spectroscopy [11], multi-frequency imaging of respiratory changes[12], imaging brain function[13, 14], and detection of breast cancer[15, 16].

Applying the MFEIT concept may be also useful in industrial processes whose component materials offer a significant frequency-dependant contrast, and where the spectral information may then be employed to enhance the identification of the materials. The key point in the spectral study is that MFEIT systems must have the capability of data acquisition and processing to satisfy application process dynamics. Important factors for this requirement are the speed of response of the instrumentation, and the type of excitation signal. The current speed and accuracy performance of general electronic devices allow the implementation of high-speed EIT instrumentation. This allows the selection and design of an optimal excitation signal that will include the frequency range of interest, to excite the spectral variations; and will also allow the signal to be injected and corresponding data to be recovered within the requisite dynamic time interval.

1.2 Objectives of this Research

This thesis describes and details research work in the maturing technology of EIT. The key objective of this research is the augmentation of a conventional single-frequency EIT system to form a wideband EIT (WEIT) system. The research seeks to extend the performance of EIT systems to provide spectral information, but with the essential ability to operate within the process dynamics. This new capability for the measurement of spectral data potentially leads to the characterisation of materials, or component identification; or the estimation of the parameters of a process model. The underlying opportunity for this study is that process materials may show considerable variation in their electrical properties, in response to an injected signal over some frequency range. This concept has been deployed in the research to demonstrate the construction of tomographic images for a range of frequency bands that can provide a deeper understanding and interpretation of a process under investigation.

Since the performance of such extended EIT systems will be critically dependent upon the choice of excitation signal, the thesis also presents characteristics of the various wideband excitation signals that were assessed for their feasibility for use for simultaneous spectral measurement. It addresses the selected method which has been developed and the associated algorithms for WEIT. This deploys a Chirp wideband excitation signal and the wavelet transform to reveal spectral data sets from the measured results. The method is verified by simulation study in this research. The thesis also demonstrates the feasibility of the presented method on experimental data collected by exploiting an implemented single-channel EIT system designed and implemented for pseudo-static tests.

1.3 Overview of this Thesis

This thesis is organised in 7 chapters and an overview of their content follows. Following this introductory chapter, chapter 2 provides a brief overview of EIT systems. It illustrates a typical framework for the EIT method including forward and inverse problem aspects. It then describes an overview of typical EIT hardware.

Chapter 3 provides a review and critical comparison of excitation signals capable of exploitation in a WEIT system. This begins with a background review of multi-frequency EIT(MFEIT) followed by a description of the factors that influence the selection of the optimal form and parameters of a wideband signal. The chapter finally presents a comparison of the presented signals and concludes that deploying a Chirp signal in a WEIT system is advantageous compared with the other possible signal forms.

Chapter 4 is devoted to the methods that can be deployed to extract the required temporal parameters from the chirp signal. It provides a short review of the time-frequency transforms including short-time Fourier transform (STFT) and wavelet transform (WT). Based on the complex continuous wavelet transform (CWT), algorithms developed to extract precise temporal values of Chirp are described. This is carried out by using the ridge phenomenon and the determination of optimum wavelet parameters. The performance of the algorithms is then described based upon an evaluation through simulations on a RC network model of a process.

Chapter 5 addresses the augmentation of a conventional EIT to form a wideband EIT system. For this purpose a novel method using the selected Chirp excitation is proposed and implemented. In this chapter, the method is described and its verification is demonstrated. This begins with a brief description of the concept of spectro-tomography. The performance of the method is examined through various simulations which are illustrated. The methods for the analysis of the spectral tomographic data are finally presented by simulation.

Chapter 6 describes the verification of the proposed method through an experimental feasibility study. An overview of the implementation of the electronic system is included. This provides an brief description of the aspects of the single-channel EIT system exploited for the experimental trials. Various experimental tests, conducted by a resistive paper simulant and also a 16-electrode EIT rig, are illustrated. The chapter ends with a review of the experimental data sets and their analysis, illustrating tomography images reconstructed over the frequency range of interest.

Finally, chapter 7 presents a summary of the achievements of the research with an overview of the most important results. This chapter concludes with suggestions for further development for this specific research area and also suggestions for more general future work.

Chapter 2

Electrical Impedance Tomography

2.1 Summary

Electrical impedance tomography(EIT) is a technique that produces impedance distribution images by using a set of peripheral measurements whilst various geometrically different current patterns are passed through the subject. Figure 2.1 shows a general structure of an EIT system. The measurements are collected by hardware and are then utilised by EIT software to produce tomography images. The EIT software includes two separate aspects which are concerned with EIT

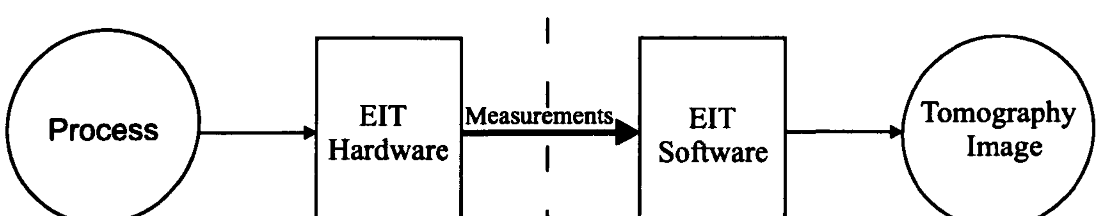

Figure 2.1: General structure of EIT system.

physical modelling(typically called forward solver) and image reconstruction(or inverse solver). In this chapter, after a brief review on the EIT inverse solver and its relation to the overall EIT problem, various issues related to the EIT forward modelling and image reconstruction are briefly presented. The remainder of the chapter is devoted to a consideration of the necessary hardware for a EIT system.

2.2 EIT as Inverse Problem

An observation model of a general physical process can be described by:

$$y = F(x) + v \tag{2.1}$$

where F is an operator which maps the vector x, the cause, into the vector y, the effect, and v the is the vector of errors. For instance, in a physical process x is unknown physical parameters which have to be estimated and y denotes observations. The problem of determination of causes from effects is called *inverse problem*. Inverse problems typically are ill-posed [17, 18, 19, 20]. This means that they don't satisfy all or a part of Hadamard's well-posedness conditions. According to these conditions, a problem is called well-posed if[17]:

- For each y a solution exists;
- For each y the solution is unique;
- The solution x depends continuously on the y.

EIT is in essence an inverse problem in which the admittivity distribution inside a medium is estimated by using a set of boundary measurements. In this problem, small variations of boundary measurements can result in large changes of inverse admittivity solution; and conversely large changes of interior admittivity may cause small measurement changes. Thus, the EIT inverse problem is unstable and sensitive to the measurement noise and errors [21]. According to the Hadamard conditions, this means that in EIT there is no continuous relation between solution and measured data and hence EIT problem is considered an ill-posed problem[22, 18]. The procedure to find the solution to an EIT problem is also known as image reconstruction. The typical block diagram for this is shown in figure 2.2. In this diagram, the *forward solver*, based on the process mathematical model, results in a set of boundary voltages $U(\gamma_i)$ for some admittivity distribution γ_i. These voltages together with the experimental measured data set are utilised for the purpose of the *inverse solver* to estimate an approximation of the unknown admittivity distribution. Incorporating *prior knowledge*

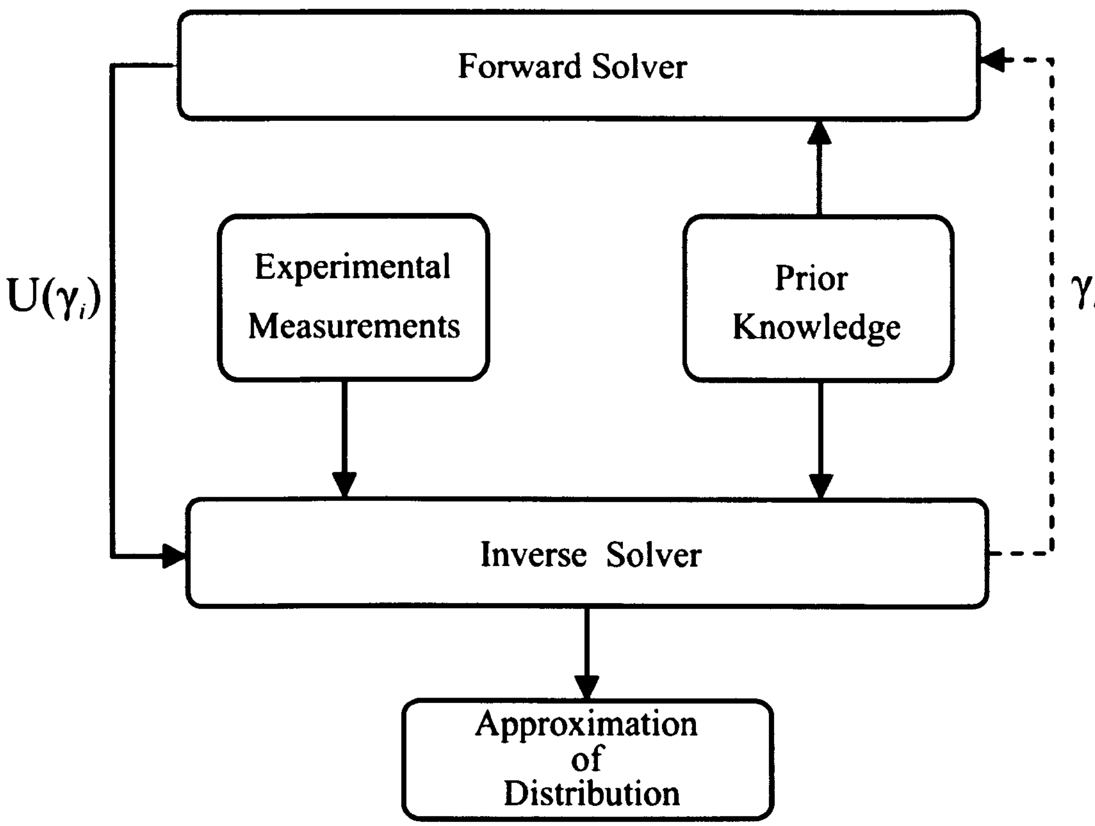

Figure 2.2: Typical block diagram for the EIT Inverse problem.

in the forward and inverse solvers has a vital role on estimating the solution. A priori information will typically include structural information, and conductivity values of process materials [23].

2.3 Forward Modelling

Forward modelling provides a critical contribution to the speed and accuracy of the EIT inverse solver. The Forward modelling concerns the calculation of boundary measurements based on a model of the process and its conductivity distribution. The EIT mathematical model must be a precise translation of the physical process and in good agreement with experimental tests. The model must consistently represent the geometry and the effects of the electrode characteristics [24, 25, 26]. The detailed overview of forward modelling is presented in the remainder of this section.

2.3.1 Electromagnetic Principle of EIT

To describe the electromagnetic theoretical foundation of EIT, it may be beneficial to explain what it is meant by conductivity and permittivity which describe a material in terms of its specific electrical behaviour. The conductivity, σ, is a proportional factor between current density, j, and applied electric field, E, in a relation which is based on *Ohm's law*:

$$j = \sigma E \tag{2.2}$$

The permittivity, ϵ, is a factor proportional between the electric flux density, D, to the external electric field intensity. This is given by:

$$D = \epsilon E = \epsilon_0 \epsilon_r E \tag{2.3}$$

here ϵ_0 is permittivity of free space and ϵ_r is relative permittivity of the material. In practice, permittivity is given by an experimentally measurable relative value ϵ_r which is dimensionless.

In a medium which contains materials with significant conductivity or permittivity or both of these properties; the relation between electric field, magnetic field, current density and charge density are linked by *Maxwell's equations* [27, 28]. In the absence of internal current source, the time-variant forms of these equations are expressed by:

$$\nabla \times E = -\frac{\partial B}{\partial t} \qquad \text{Faraday's law} \tag{2.4a}$$

$$\nabla \times H = j + \frac{\partial D}{\partial t} \qquad \text{Ampere's law} \tag{2.4b}$$

$$\nabla \cdot D = \rho \qquad \text{Gauss's law} \tag{2.4c}$$

$$\nabla \cdot B = 0 \qquad \text{No magnetic monopoles} \tag{2.4d}$$

where B is magnetic flux density, H is magnetic field, j is conductive electric current density in the absence of internal source and ρ is charge density. The *Time-harmonic* versions of these equations are also given by:

$$\nabla \times E = -i\omega B \tag{2.5a}$$

$$\nabla \times H = j + i\omega D \tag{2.5b}$$

In these equations, ω is angular frequency in radian and all vectors and scalar quantities are phasors. Over a low frequency range, the electromagnetic field is assumed to be negligible. As a result of this assumption $\nabla \times E = 0$ and for the electric potential u the expression $E = -\nabla u$ is still valid. By substituting this into equation (2.5b) and taking its divergence, a second-order differential equation for the potential u is obtained:

$$\nabla \cdot \gamma \nabla u = 0 \tag{2.6}$$

where γ is called the admittivity of the medium and given by $\gamma = \sigma + i\omega\epsilon$ at angular frequency ω. The real part of γ indicates DC conductivity which is the movements of free charges and frequency independent while the imaginary part shows *a.c.* conductivity that is the effect of dielectric property and frequency dependent. For a particular application it may be reasonable to compare the real and imaginary parts at a certain frequency. In effect, when $\sigma \gg \omega\epsilon$ then the material is more conductive whereas materials are more reactive when $\sigma \ll \omega\epsilon$. Based on the values of σ and ϵ_r of the materials in a particular application, an appropriate technique may be selected[29].

Equation (2.6) expresses the main equation for the EIT inverse problem. This equation together with a mathematical model of the boundary conditions are known as the electrode model which is the subject of the next section.

2.3.2 Electrode Model

To deliver a unique solution to (2.6) one needs to incorporate an appropriate mathematical model of the boundary conditions and supply sufficient boundary restrictions [30]. For accurate modelling it is also necessary to consider issues including discretisation, shunting effect and contact impedance [25, 31, 21, 32]. The discretisation is subject of the next section. The shunting effect implies that the potential on the electrode is constant. This effect can be considered by equation (2.7b). The contact impedance is effective impedance of interface between the electrode and the object. This is considered in the (2.7c). The model which includes all of these issues is usually called the electrode model. A detailed study of the various models can be found in [25, 31, 26]. The most accurate model is termed a *complete electrode model.* This model consists of equation (2.6) in association with the following equations:

$$\gamma \frac{\partial u}{\partial n} = 0 \qquad \text{between electrodes} \tag{2.7a}$$

$$\int_{e_l} \gamma \frac{\partial u}{\partial n} = I_l \qquad \text{on the electrode } e_l,\ l = 1, 2, \ldots, L \tag{2.7b}$$

$$u + z_l \gamma \frac{\partial u}{\partial n} = V_l \qquad \text{on the electrode } e_l,\ l = 1, 2, \ldots, L \tag{2.7c}$$

where n is outward unit normal, L is the number of electrodes, e_l is lth electrode, I_l is injected current to the lth electrode, V_l is voltage on the lth electrode and z_l is effective contact impedance of the lth electrode. For the existence of a solution, the charge conservation law must be included in equations (2.7):

$$\sum_{l=1}^{L} I_l = 0 \tag{2.8}$$

For a unique solution it is also necessary to have a common reference for the electrodes potentials. This can be expressed by:

$$\sum_{l=1}^{L} V_l = 0 \tag{2.9}$$

In [31] it has been proved that the complete model has a unique solution. This model is commonly used in EIT forward modelling, for instance, it has been exploited by many researchers [25, 26, 31, 32].

2.3.3 FEM Discretisation

The Finite element method (FEM) is a numerical method to find an approximate solution to a set of partial differential equations. Any complicated geometry of is discretised into the finite number of elements. These elements can have simple shapes such as a triangle in 2-D and hexahadron in 3-D domains. Each element is specified by its nodes and faces [33]. In EIT, due to various geometry and interior inhomogeneities, the FEM is employed to find the solution to the complete electrode model illustrated in the previous section. FEM modelling for the 2-D and 3-D EIT problem has already been conducted and can be found in [32, 34, 35, 36].

There are two main steps to solve a problem with FEM. The first step is to derive the variational or so-called weak form of the original problem. For this, a partial differential equation system and all other associated conditions are reconfigured to form a variational formulation. The next step is to exploit FEM for the discretetisation of the weak form on a finite domain. The solution of a problem,

u, can be approximated by FEM as:

$$u(x) = \sum_{i=1}^{N_n} \alpha_i \phi_i(x) \tag{2.10}$$

here N_n is the number of nodes and $\phi_i(x)$ is the basis function on the i^{th} node. The approximation voltage on the boundary electrodes U is described by:

$$U = \sum_{j=1}^{L-1} \beta_j n_j \tag{2.11}$$

where L is the number of electrodes and n_j is a basis function. The basis functions chosen n_j are set to $n_1 = [1, -1, 0, ..., 0]^T$ and $n_2 = [1, 0, -1, 0, ..., 0]^T \in \mathbb{R}^{L\times 1}$ and so on. In the equations (2.10) and (2.11) coefficients α_i and β_j are unknown and must be determined. In [32, 35] it has been proved that by substituting the u and U in the weak formulation results, the FEM system equations is constructed as:

$$Ab = f \tag{2.12}$$

where $b = (\alpha, \beta)^T$ and $\alpha = [\alpha_1, \alpha_2, \cdots, \alpha_{N_n}]$ and $\beta = [\beta_1, \beta_2, \cdots, \beta_{L-1}]$ and also $f = (\mathbf{0}, \tilde{I})^T$ in which $\mathbf{0}$ is $1 \times N_n$ vector and $\tilde{I} = \{I_1 - I_2, I_1 - I_3, \cdots, I_1 - I_L\}$, I_l is the enjectted current and $l = 1, \cdots, L$. Therefore, the approximate solution for the potentials on the nodes and electrodes, b, can be determined by $b = A^{-1}f$. In (2.12) the FEM system matrix A is:

$$A = \begin{bmatrix} B & C \\ C^T & D \end{bmatrix}$$

where[32]

$$B(i,j) = \int_{\gamma} \sigma \Delta\phi_i \cdot \Delta\phi_j dx + \sum_{l=1}^{L} \frac{1}{z_l} \int_{e_l} \phi_i \phi_j ds \tag{2.13a}$$

$$i, j = 1, 2, \cdots, N_n$$

$$C(i,j) = -(\frac{1}{z_1} \int_{e_1} \phi_i ds - \frac{1}{z_{j+1}} \int_{e_{j+1}} \phi_i ds) \tag{2.13b}$$

$$i = 1, 2, \cdots, N_n, \; j = 1, 2, \cdots, L-1$$

$$\begin{aligned} D(i,j) &= \sum_{l=1}^{L} \frac{1}{z_l} \int_{e_l} (n_i)_l (n_j)_l ds \\ &= \begin{cases} \dfrac{|e_1|}{z_1} & i \neq j \\ \dfrac{|e_1|}{z_1} + \dfrac{|e_{j+1}|}{z_{j+1}} & i = j \end{cases} \end{aligned} \tag{2.13c}$$

In equation (2.13a) s is a boundary measure and in equation (2.13c) $|e_j|$ is the area of the j^{th}electrode, and $i, \; j = 1, 2, \cdots, L-1$.

2.3.4 Forward Solver

The solution to the system equation (2.12) is usually known as the forward solution. For this, the admittivity distribution γ and the injected current must be known. In (2.12) A is a sparse, symmetric as shown in figure 2.3, as an example. For the real admittivity distribution, A is real while it is complex for complex admittivity. This implies the type of methods which can be exploited. For the real case the Cholesky [34] method gives the exact solution. However, in the complex case, since A is not positive definite, the Cholesky method cannot be used. In this case, LU factorisation method [34]is able to provide the solution. In this method, the matrix A is expressed by two upper and lower triangular matrices. In this thesis the publicly available 2-D EIDORS suite [37] is selected

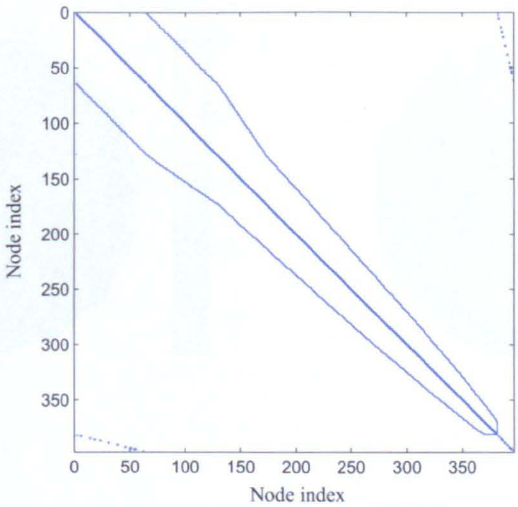

Figure 2.3: Sparsity of the FEM system matrix A, where the number of nodes N_n=381, L=16, the number of matrix elements: 156816 and nonzero elements: 2656.

as the base system to implement the algorithms. There are two reasons for this selection. Firstly, many researchers report the use of the EIDORS libraries which imply the validation of this software, for instance, the 3-D EIDORS solution has been verified by 2-D EIDORS [38]. Secondly, the open source provision of this package gives the possibility of its convenient adaption to fit a particular application. In this software, existing Matlab [39] routines for the Cholesky and LU factorisation are deployed for the real and complex admittivity distribution, respectively.

To illustrate the solution of the forward solver a numerical example of electric potential on a circular conductive medium containing an inclusion is considered. In figure 2.4, which shows the potential distribution when the current is injected through electrodes 4 and 12. Since the inclusion is more conductive, it can clearly be seen that the equipotential lines are changed in the location of the inclusion. This is the reason that the EIT methods are classified as soft-field tomography. The forward simulation was also conducted for various different values of the conductivity σ and similar boundary conditions. The corresponding boundary voltages are shown in figure 2.5. This figure shows that the large

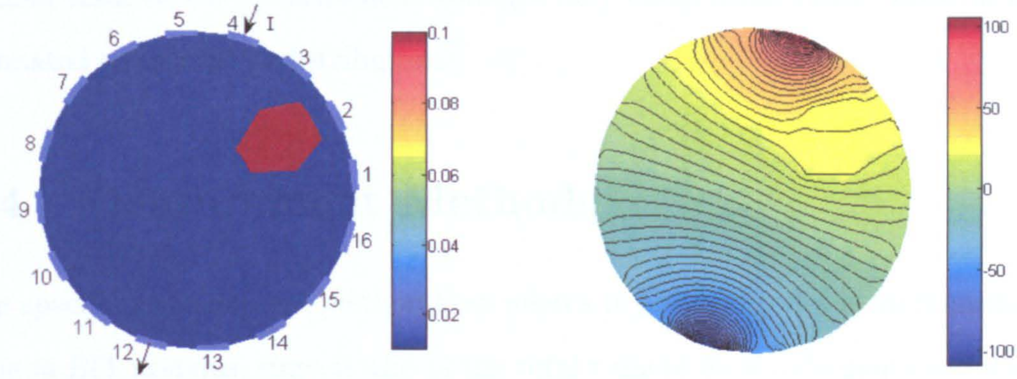

(a) (b)

Figure 2.4: (a) A Conductive disk with $\sigma_m = .01(S/m)$ and an inclusion object with $\sigma = 10\sigma_m$ when $I = 1A$, and with 16 electrodes distributed evenly around the circumferences, (the colourbar in S/m), and (b) the potential distribution (the colourbar in V) (b).

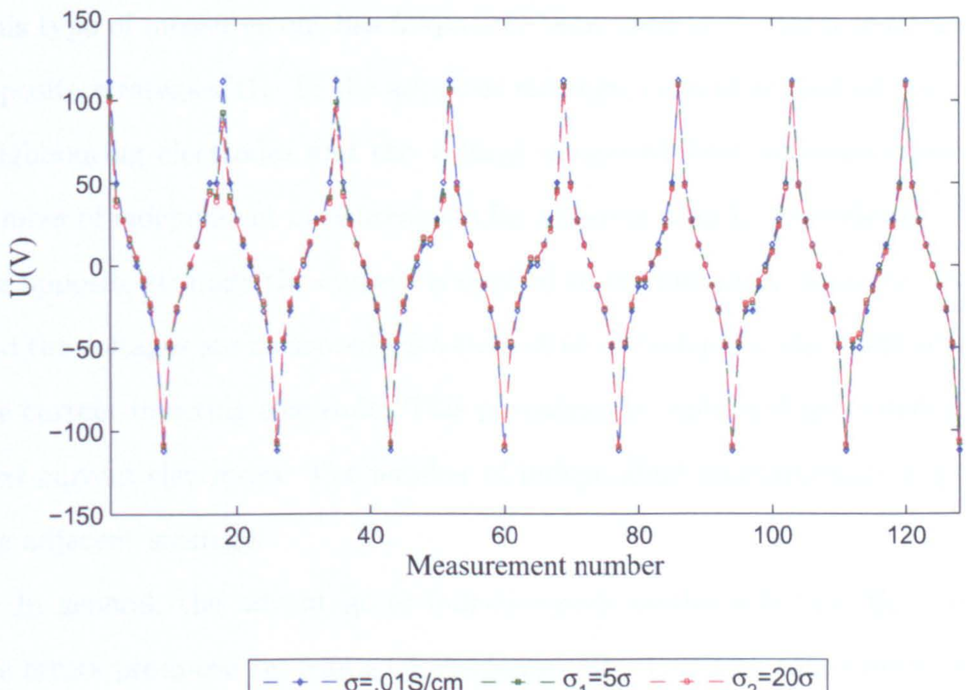

Figure 2.5: A complete set of boundary voltages for different cases of the system in figure 2.4 consisting of: the homogeneous medium, $\sigma_m = .01(S/m)$ and with inclusion $\sigma_1 = 10\sigma_m$ and $\sigma_2 = 20\sigma_m$.

changes in the inclusion object conductivity appear as small potential changes on the boundary. This is consistent with the ill-posedness of the EIT, that is a small error in the measurement voltages may cause a significant error in the estimated conductivity distribution.

2.4 Measurement Methods

The specific measurement method that relates to the electrodes is an important issue in EIT systems, since it affects the total time of data collection procedure, hardware requirements, quality of tomography images and their reconstruction computation time [40, 41]. There are two principal measurement methods consisting of: four-electrode and multiple drive method.

In four-electrode methods, the current is applied to two electrodes and the voltages are measured on all other electrodes except the so-called excitation ones. This type of measurement has frequently been used in the form of adjacent and opposite strategies[41]. In the adjacent strategy, current is applied through two neighbouring electrodes and the voltage measured from successive pairs. The number of independent measurements for a system with L electrodes is $\frac{L(L-3)}{2}$. In the opposite strategy the current is applied to diametrically opposite electrodes, and the voltages are measured with respect to the reference electrode adjacent to the current-injecting electrode. This procedure is continued by switching to the next current electrodes. The number of independent measurements is similar to the adjacent strategy.

In general, the advantage of four-electrode methods is that they minimize the errors produced by contact impedance [32]. For both four-electrode forms, the adjacent method needs minimal implementation hardware.Since the current density in the periphery of the process is bigger than in the central part, it gives better sensitivity to the conductivity changes in this peripheral region. In contrast, in the opposite method the current goes through the central part of the process and causes larger and more even current density, resulting in better sensitivity in this region and less sensitivity to changes in the periphery [42, 41, 40].

The multiple drive method features multiple current sources that excite all electrodes simultaneously and the voltages are measured on the same electrodes. Gisser[43] introduced an approach to find an optimum current pattern that results in maximum voltage difference on the electrodes. He introduced *distinguishability* as a measure of the current patterns' ability to distinguish between two conductivities. For two conductivities σ_1 and σ_2, the distinguishability δ is defined [42, 44] by:

$$\delta = \frac{||R(\sigma_1)I - R(\sigma_2)I||}{||I||} \tag{2.14}$$

where R is a function of conductivity, I is current pattern applied to the medium and $||\cdot||$ is L^2 norm. Equation (2.14) is influenced by several factors including the injected current, the size and number of electrodes and measurements strategy . The optimal current pattern can be obtained by maximising the value of (2.14). However, in practice distinguishability is related to the unknown conductivity distribution, and hence the best current density cannot be calculated in advance. Instead, it may be calculated by an adaptive procedure [42, 21]. The multiple source method gives the most accurate images. Compared to the four-electrode methods, the hardware complexity and sensitivity to contact impedance are accounted as drawbacks of this method. The errors due to the multiple source method are discussed in [45, 40].

2.5 Jacobian Calculation

The reconstruction algorithm usually involves the calculation of the Jacobian matrix. This matrix expresses how a small conductivity change within the medium contributes to the electrode voltages. Thus for its calculation the derivatives of the electrode voltages must be calculated with respect to the conductivity of each element. Depending on whether admittivity is real or complex, the Jacobian will also be different for these two cases. For the real admittivity distribution [32] by using (2.12) the derivative of voltage vector b with respect to the j^{th} element is given by:

$$\frac{\partial b}{\partial \rho_j} = \frac{\partial A^{-1} f}{\partial \rho_j} = -A^{-1}\frac{\partial A}{\partial \rho_j} b \tag{2.15}$$

where

$$\frac{\partial A(l,k)}{\partial \rho_j} = -\frac{1}{\rho_j^2}\int_{\Delta_j} \Delta\varphi_l \Delta\varphi_k dx \quad j = 1, \cdots, N_e \ , \quad l,k = 1, \cdots, N_n \tag{2.16}$$

here N_e is the number of elements, and Δ_j denotes the element that the derivative is calculated with respect to. The sensitivity of the boundary voltages U in regard to the element j ($\frac{\partial U}{\partial \rho_j}$) can then be extracted from (2.15). This gives the j^{th} column of the Jacobian matrix. To complete the Jacobian, this procedure is repeated on all elements to form the Jacobian matrix J [32]:

$$J = \begin{bmatrix} \frac{\partial U_1^1}{\partial \rho_1} & \frac{\partial U_1^1}{\partial \rho_2} & \cdots & \frac{\partial U_1^1}{\partial \rho_{N_e}} \\ \vdots & \vdots & \vdots & \vdots \\ \frac{\partial U_L^1}{\partial \rho_1} & \frac{\partial U_L^1}{\partial \rho_2} & \cdots & \frac{\partial U_L^1}{\partial \rho_{N_e}} \\ \vdots & \vdots & \vdots & \vdots \\ \frac{\partial U_1^k}{\partial \rho_1} & \frac{\partial U_1^k}{\partial \rho_2} & \cdots & \frac{\partial U_1^k}{\partial \rho_{N_e}} \\ \vdots & \vdots & \vdots & \vdots \\ \frac{\partial U_L^k}{\partial \rho_1} & \frac{\partial U_L^k}{\partial \rho_2} & \cdots & \frac{\partial U_L^k}{\partial \rho_{N_e}} \end{bmatrix} \tag{2.17}$$

where k denotes the k^{th} driving current pattern. In (2.17) each row is called a sensitivity map, which describes the sensitivity of each element with respect to the particular measurement. Since J is sparse and ill-conditioned the numerical solution to the EIT inverse problem is unstable. The common remedy to overcome this problem is the utilisation of regularization which will be briefly illustrated in the next section.

In the case of complex admittivity, the measurement voltages U are also complex and both conductivity and permittivity contribute to the real and imaginary parts of the electrode voltages. Therefore, the Jacobian can be formed as [38, 46]:

$$J = \begin{bmatrix} J_R^\sigma & J_R^\epsilon \\ J_I^\sigma & J_I^\epsilon \end{bmatrix} \tag{2.18}$$

where J_R^σ and J_R^ϵ are the sensitivity of real part of U in respect to the conductivity, and permittivity, respectively, and J_I^σ and J_I^ϵ are the sensitivity of the imaginary part of U with respect to the conductivity and permittivity respectively. These are expressed by:

$$J_R^\sigma = \frac{\partial U_R}{\partial \sigma} \tag{2.19a}$$
$$J_R^\epsilon = \frac{\partial U_R}{\partial \epsilon} \tag{2.19b}$$
$$J_I^\sigma = \frac{\partial U_I}{\partial \sigma} \tag{2.19c}$$
$$J_I^\epsilon = \frac{\partial U_I}{\partial \epsilon} \tag{2.19d}$$

In the 2-D EIDORS, in order to solve forward and inverse problems, the real and imaginary parts of admittivity of elements are formed in one vector as $\gamma = [\sigma \quad \epsilon] \in \mathbb{R}^{2N_e}$, and similarly for the measurement voltages as $U = [U_R \quad U_I] \in \mathbb{R}^{2M}$. By these formulations, the real and imaginary images are embedded in one reconstruction procedure.

2.6 EIT Image Reconstruction

In this section the basics of EIT image reconstruction, and also an overview of typical algorithms, are briefly described. The importance of image reconstruction is that the images contain information on the distribution of the constituent parameters, and thus their correctness is of crucial importance both quantitatively and qualitatively. In EIT, the deterministic observation model given by (2.1) can be rewritten for the EIT inverse problem as:

$$V_{meas} = U(\gamma) + v \tag{2.20}$$

here V_{meas} is the measurement potential vector on the peripheral electrodes; U is the forward model that gives the computed boundary potential for some admittivity distribution γ; and v denotes the additive noise and measurement error. The unknown vector γ must be estimated such that the potential V_{meas} on the electrodes matches the ones computed by the forward model. The conventional method for this is to find γ such that it minimizes the least square error expressed by [32, 47]:

$$E(\gamma) = \|V_{meas} - U(\gamma)\|^2 \tag{2.21}$$

where $U(\gamma)$ and $V_{meas} \in \mathbb{R}^M$ and M is total number of measurements. Due to the ill-posedness of EIT problems the methods of (2.21) do not lead to a stable solution. To overcome this difficulty, regularisation techniques must be exploited. A popular method for this is the regularised Gauss-Newton method [48]. An alternative approach is to use the conjugate gradient method, which inherently applies regularisation through their iterative procedures [34, 49]. In addition to its ill-posedness, the EIT problem is also non-linear, and thus $U(\gamma)$ must also be linearised.

Based on the admittivity contrast, the methods for EIT inverse problems can be classified into two main categories. Problems with small admittivity contrast are usually solved by a one-step computation, while the iterative methods are exploited where the admittivity variation is large. The solution to these two types of problems have been widely studied in the literature and different methods have been presented for example in [32, 23, 48, 47, 50, 51, 34, 52, 1, 21, 53, 54, 55]. A typical example, for the first category, is the one-step Newton method which is deployed, for instance, in NOSER [47], and for the second category are non-linear Tikhonov regularised Gauss-Newton and non-linear Conjugate gradient methods. In this research, the non-linear Tikhonov regularised Gauss-Newton method has been utilised for the reconstruction purpose. The reconstruction using this method is much faster than that of non-linear Conjugate gradient method [34]. In the following section, the Tikhonov regularised Gauss-Newton method is briefly illustrated.

2.6.1 Tikhonov Regularised Gauss-Newton Method

This method is one of the most common methods in the EIT inverse problem. The main advantage of this method is the capability of incorporating a priori information about the problem solution [18]. For large variation of admittivity, the non-linear form of this method can be utilised to minimize the regularised form of (2.21). This is expressed by the function $E(\gamma)$ as [32, 48]:

$$E(\gamma) = \|V_{meas} - U(\gamma)\|^2 + \alpha \|L(\gamma - \gamma_0)\|^2 \tag{2.22}$$

where α is regularisation parameter, L is the regularisation matrix, and γ_0 is the initial prediction for the admittivity vector. The problem (2.22) is solved iteratively. In each step the problem is linearised in the neighbourhood of the admittivity distribution of the previous step, and the forward approximation U and Jacobian matrix J are updated. Thereby, at the $(i+1)^{th}$ step $U(\gamma_{i+1})$ can be linearised by substituting its approximation around γ_i as:

$$U(\gamma_{i+1}) = U(\gamma_i) + J(\gamma_{i+1} - \gamma_i) \tag{2.23}$$

Here J denotes the Jacobian at the i^{th} step. Therefore, the linearised form of (2.22) can be written as:

$$E(\gamma_{i+1}) = \left\|\hat{V}_{meas} - J\gamma_{i+1}\right\|^2 + \alpha \|L(\gamma_{i+1} - \gamma_0)\|^2 \tag{2.24}$$

where $\hat{V}_{meas} = V_{meas} - U(\gamma_i) + J\gamma_i$. At each iteration the solution to the equation (2.24) is given by:

$$\gamma_{i+1} = \gamma_i + (J^T J + \alpha L^T L)^{-1}[J^T(V_{meas} - U(\gamma_i)) - \alpha L^T L(\gamma_i - \gamma_0)] \tag{2.25}$$

The iterations are usually terminated by evaluation of *Morozov*'s criterion, defined by $||V_{meas} - U(\gamma)||^2 < Er$, where Er is the level of measurement noise. In practice, to perform iteration (2.25) one also needs to estimate the initial admittivity distribution. However, this is unknown in most applications. For a homogeneous distribution it has been shown that γ_0 can be determined by using V_{meas} and minimization of $||V_{meas} - U(\gamma_0)||^2$ [32].
The above reconstruction method results in the absolute admittivity distribution. In general, any method for absolute reconstruction is known as ***absolute*** or *static* imaging. This type of imaging also delivers the structural information regarding the features inside the process.

In the linear case, where the admittivity changes are small, the absolute admittivity can be reconstructed provided that the the initial distribution is known. Alternatively, the admittivity changes can also be reconstructed. This is known as *difference* imaging, in which the tomography images are reconstructed by utilising two measured data sets at two different instants of time [56]. This type of imaging is an alternative way of estimating the initial admittivity distribution. The linear EIT inverse problem is defined as:

$$\delta V = \delta U = J\delta\gamma \tag{2.26}$$

In this equation $\delta V = V_2 - V_1$, $\delta U = U(\gamma_2) - U(\gamma_1)$ and $\delta\gamma = \gamma_2 - \gamma_1$. One of these two points is considered as a reference at which the Jacobian matrix must also be calculated. The solution, $\delta\gamma$, for the minimization of function $||\delta V - J\delta\gamma||^2$ is obtained by the regularisation method and expressed by:

$$\delta\gamma = (J^T J + \alpha L^T L)^{-1} J^T \delta v \tag{2.27}$$

In both linear and non-linear cases, α is very important in the performance of the reconstruction. By setting an appropriate regularisation factor the effect of the regularisation can be traded off for the influence of the measurement noise on the solution. The methods for the selection of the regularisation parameter are discussed in [18, 35].

2.7 Quasi-static and Multi-frequency Imaging

In a similar way to difference imaging, the tomography image can be reconstructed by taking the measurements at two different frequencies, one of which is considered a reference image. The resulting image therefore, does not show features that do not have frequency-dependent characteristics; and parts with greater changes appear with higher contrast. This type of imaging was initially introduced for medical EIT in [57] and is known as *quasi-static.*

In *multi-frequency* imaging, the frequency-dependent behaviour of process features are investigated, but here it is necessary to perform measurements over a range of frequencies. In principle, these measurements would be performed within a very short time interval, such that the process features remain identical over the interval. The values of tomography images may then be used to estimate the parameters of an appropriate model, for instance, the Cole model [58] for liquid chemical substances, which has also been used in medical EIT to characterise tissues in spectral terms[11, 59, 12, 60, 61]. The multi-frequency methods will be reviewed in the next chapter.

2.8 EIT Hardware

The general block diagram of an EIT system structure is shown in figure 2.6. In order to collect a set of measurements, the process peripheral electrodes are linked to either the excitation or measurement circuitry by multiplexers controlled by the control system. This is conducted according to the defined measurement protocol as described earlier in section 2.4. Due to its relative simplicity, the single- source approach has been widely used by researchers, for instance, in [59, 41, 62, 63, 64]. In this method, the current waveforms are distributed to pairs

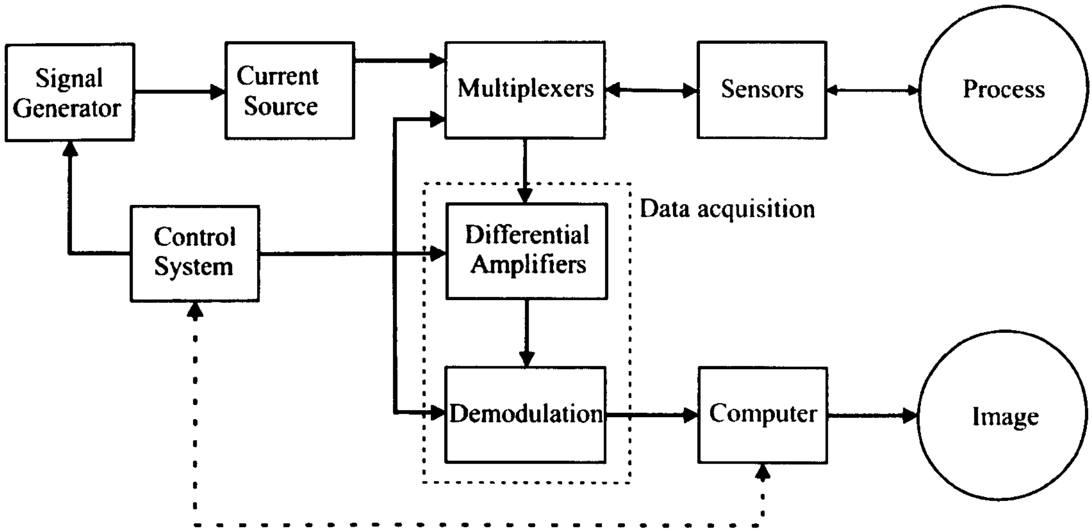

Figure 2.6: Basic block diagram of EIT system.

of electrodes through switching multiplexers, and consequently measurements are collected on the rest of electrodes. The measurements can be conducted either sequentially or in parallel. The sequential system needs less hardware, but the drawback is that its total acquisition time is much longer than that of parallel systems.

In the multiple-source method, however, the number of sources and electrodes are equal and each electrode can have different current value according to the current pattern [65]. The patterns is usually designed to perform optimal experiments [21]. These systems are more complex in comparison with the single-source method. Multiple-source systems have been used in a small number of research projects, for example, in [66, 67, 68].

2.8.1 Electrodes

Sensor electrodes in an EIT system must be in electrical contact with the medium inside the process. The electrodes' size and their positioning are important factors, since they affect the accuracy of measurements and in turn the reconstructed images. In EIT systems the electrodes are usually of equal size and also the same electrodes are utilised for excitation and measurement. Further details on the size of electrodes can be found in [30] and also various types of electrode structures have been introduced in [40, 69].

2.8.2 Signal Generation

Owing to the influence of signal quality on the performance of the current source and consequently on the quality of the measured data set and reconstructed images, signal generation is considered an important element in EIT systems. The signal generator must provide a stable signal in terms of amplitude and phase during the data acquisition time. The signal must also be spectrally pure and preserve the required specification over its frequency range [70, 71].

The most recent EIT systems are designed by using a *direct digital synthesis* (DDS) device as the main core of a highly stable and accurate signal generator. For example [64, 16] report DDS-based signal generation controlled by a digital signal processor (DSP). The basic block diagram of the DDS signal generator [72] is shown in figure 2.7. As the diagram shows, the phase accumulator increments

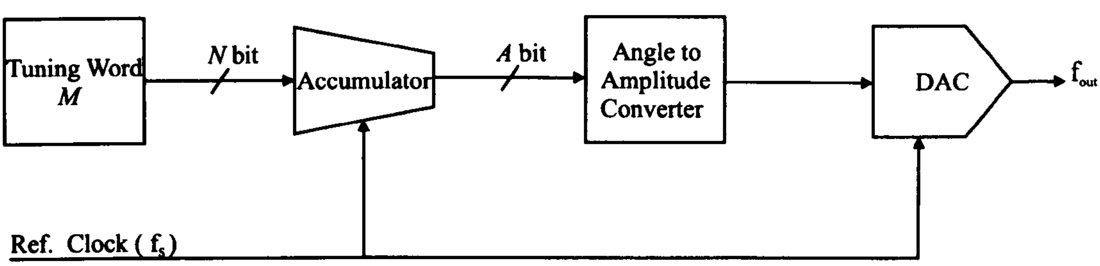

Figure 2.7: Basic block diagram of the DDS generator.

its value by a phase step in each clock pulse. The output of this accumulator is then translated to the amplitude information of the *sine* wave. This is then converted to the analog signal by the output digital to analog converter (DAC). The output frequency f_{out} can be determined by :

$$f_{out} = \frac{M(f_s)}{2^N} \tag{2.28}$$

here M is the frequency tuning word in binary, N is the length of the phase accumulator and f_s is the clock frequency.

Available DDS devices provide the possibility of tuning to a micro-hertz resolution. They also offer fast in tuning of output frequency. Furthermore, ageing and temperature drift don't affect the output frequency. For instance, devices such as AD9856 and AD9852 have high performance, functionality, small size and reasonable prices [72, 73].

As discussed later in the chapter 3 the Chirp form was selected as the excitation signal. To generate this signal the DDS technique has been used. The structure of the Chirp-based system will be described in Chapter 6 where the details of an experimental feasibility study will also be described.

2.8.3 Current Source

The current source is a circuit that theoretically is able to preserve the current inside a load without any dependency on the load itself. This is, however, practically achievable only when its output impedance is infinity [74]. In EIT systems for the same reasons as mentioned for the signal generator, having a current source with high accuracy and stability over the load dynamic range and also frequency range is highly desirable. In practice, due to non-ideal behaviour of electronic devices and stray capacitances, it is not possible to build a current source having an ideal infinite impedance. They are, therefore, built such that they meet the requirements for a specific application. The typical values for industrial applications are given in [1]. In these applications, the current source is required to be applicable to a wide range of conductivities and also the current amplitude is different depending on the application, for example 30 mA as reported in [41]. In medical EIT, however, the range of conductivity of human tissues and also patient safety are limiting factors for the design of the current source. They are designed to supply typically $0.1 - 5$ mA amplitude and have adequate output impedance to deliver current to loads in the range of 100 Ω-10 kΩ [65].

In addition to the above specifications, the current source must be stable over the desired frequency range. This is more important for the multi-frequency EIT (MFEIT) systems. The MFEIT methods will be presented in the next chapter.

In general, there are two main methods to implement a current source for EIT systems: voltage-controlled current source (VCCS); and current sense controlled voltage sources (CSVS) [70]. The most commonly used category is the VCCS, in which ideally the output current must linearly follow the input voltage and remain stable over load and frequency range. These current sources are constructed using either high quality operational or transconductance amplifiers. A variety of designs have been reported. Figure 2.8 shows some examples of VCCS circuits.

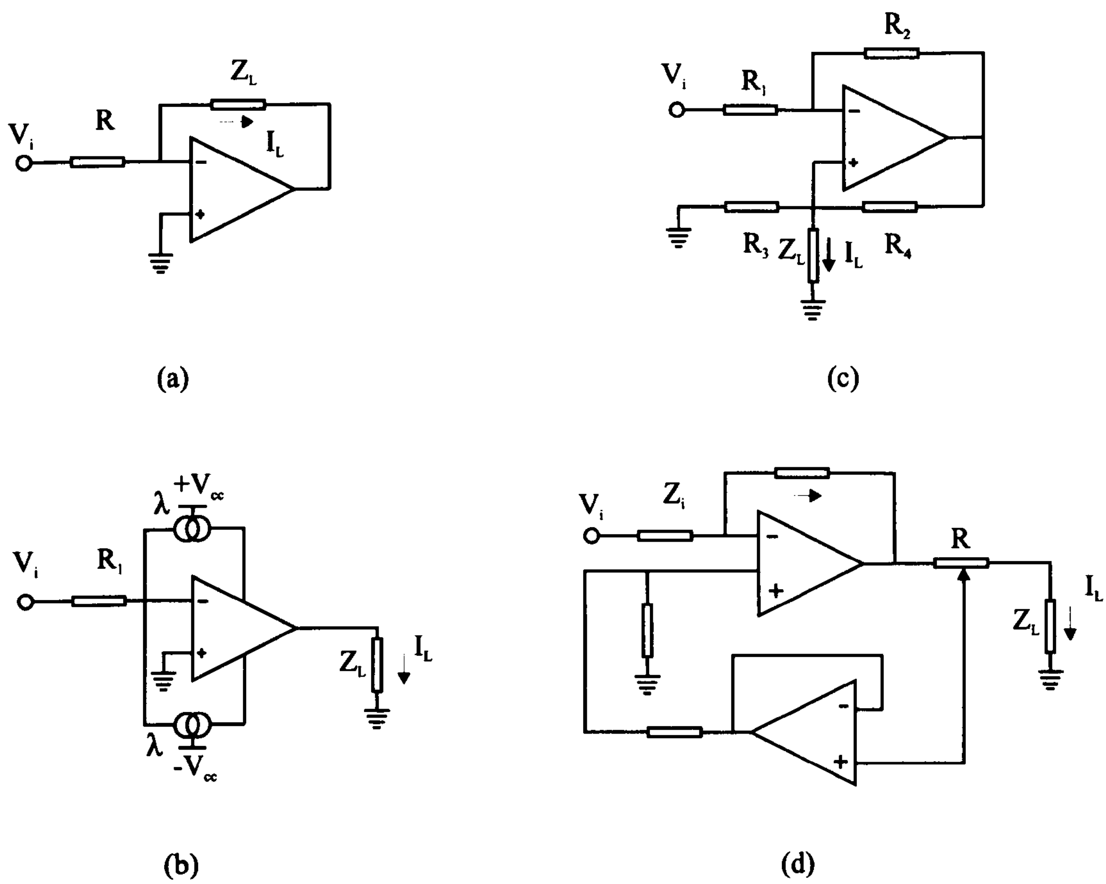

Figure 2.8: Examples of VCCS: (a) floating load current source, (b) supply-current sensing current source, (c) Howland current source and (d) dual op-amp current source.

Floating load current source, shown in figure 2.8a, is a simple form of the VCCS current source. The load in this current source can be coupled by using a transformer. In medical applications this is necessary due to safety reasons [65]. This circuit cannot be utilised for an earthed load, or where a multiple-current-source system is needed [75]. Figure 2.8b shows a supply-current sensing current source [76, 77]. In this current source the change in load current is mirrored to the inverting input of the op-amp, and therefore the load current is adjusted accordingly. The output impedance of this type of current source was reported to be about 290 KΩ at 160 kHz. Cook [67] has also reported a high precision VCCS compensated by a network parallel to the load and controlled by computer. Thus, the output impedance of the current source was better than 50 MΩ at 30 kHz. However, its major drawback is that it has limited bandwidth. A high bandwidth modified Howland current source for medical application was reported by Ross [78] and is shown in outline in figure 2.8c. It is compensated by using a generalized impedance converter (GIC) in parallel with the output load. This approach results in a simulated output impedance better than 2 GΩ over the discrete frequencies between 100 Hz and 1 MHz, while the biggest experimental impedance was 143 MΩ at 1 kHz. The major disadvantage of this method is a long procedure of current adjustment. This makes it difficult to use this current source with a multi-frequency EIT system. The modified Howland current source was also utilised in the Sheffield MK3.5 system [79]. The current source delivers a peak-to-peak current of approximately 850 μA for simultaneous frequency excitation, and has a maximum output impedance of 750 kΩ at 10 kHz. Dickin and Wang [41] also developed a dual op-amp current source, shown in outline in figure 2.8d, for industrial application. Their design is able to deliver 30 mA peak-to-peak current over the discrete frequency range between 75 Hz and 153.6 kHz and the maximum output impedance was 2.5 MΩ at 76.8 kHz.

Some researchers report the use of transconductance amplifiers. The advantages of using transconductance amplifiers are less peripheral circuitry, stability over frequency and load range. They have also wide bandwidth and thus the possibility of application to both sequential and simultaneous MFEIT systems.

Their disadvantages are the limitation of the output impedance and maximum output current. Yerworth [13] reported a current source using CCII01, in UCLH Mark 1b, which operates from 225 Hz to maximum frequency 77 kHz with output impedance (537 kΩ || 28 pF). The operational amplifier AD844 [80] has also been used to build the current source, for instance, in [81, 62, 64]. In this wide-band amplifier the slewing (TZ) pin provides a high impedance node accessible for compensation purposes. This special internal structure make possible the use of AD844 as a VCCS. Casas [62] designed a current source by employing the AD844 for the frequency range between between 10 kHz and 250 kHz. The output impedance was greater than 1 MΩ in parallel with 5 pF capacitance [81]. Wang[64] also used a AD844 in his EIT system. To achieve higher output current a parallel structure of eight AD844s have been implemented. The output impedance was about (750 kΩ || 18 pF).

Voltage sources have also been employed for the EIT excitation. In this approach, the electrodes are driven by a voltage source and the input current is rapidly sensed to control the amplitude of the input voltage accordingly. For instance, Hartov [82] achieved a bandwidth of 12.1 MHz by using AD817 as a voltage driver. Employing a voltage source has the advantages of simpler implementation and less sensitivity to noise [83, 84]. This method, however, inherently cannot be used for the simultaneous multi-frequency system.

2.8.4 Data Acquisition

The data acquisition block of figure 2.6 provides the necessary measurements with sufficient accuracy. As the figure shows, the acquisition block has two essential parts: the voltage measurement circuitry and the demodulation part, which are briefly given in following sections.

2.8.4.1 Voltage measurements

The main factors influencing the design of the measurement circuitry may be summarised as: dynamic range, common mode rejection ratio (CMRR), sufficient gain and bandwidth and also noise consideration. Most EIT systems exploit the four-electrode measurement technique, where two electrodes are utilised for current excitation, and the others for the differential measurement. This method may decrease the dynamic range of voltages which impacts the specifications of the electronics, for instance, the CMRR of differential amplifier, the dynamic range of ADC and required gain [85, 86, 41, 65]. In addition, for an MFEIT system, it is required that the above features are stable over the desired bandwidth.

2.8.4.2 Amplitude and phase demodulation

The excitation signal in EIT is usually an *ac* sinusoidal current. In the measuring side, the sinusoidal measurements are demodulated in order to provide the required data sets for the reconstruction of the tomographic images. Depending on the purpose of the EIT system, the amplitudes, phases shift or both can be extracted. The most commonly used method exploited in EIT is *digital synchronous demodulation.* This technique is based on matched filter theory. It may be proved that such demodulators maximize signal to noise ratio(SNR) if the noise is Gaussian. An advantage of this technique is that it can be implemented using a digital signal processor (DSP) that gives the advantage of efficient measurement control by software. To implement this method, each measurement is multiplied by a reference sinusoidal waveform and its quadrature counterpart, and then averaged over a certain number of samples. This procedure results in real and imaginary parts of measured voltages which are used to determine the amplitudes and phase shifts. A simpler version of digital synchronous demodulation was implemented in [82] by direct calculation of phase shift using simultaneous sampling of reference and measured signal. The detailed theory of this method is illustrated in [87, 88].

2.9 Conclusion

In this chapter an overview of EIT system has been given. It described a typical procedure for EIT problem including forward and inverse solvers. Then, it has briefly explained the typical EIT hardware.

Chapter 3

Wideband Excitation Signals for MFEIT

3.1 Summary

This chapter is devoted to the excitation signals for MFEIT. First, a review of previous multi-frequency systems is presented. Key factors in the selection and design of excitation signals are then addressed in terms of the characteristics of the various wideband excitation signals that could be used for simultaneous spectral and spatial tomography measurements. Signals investigated include: Pulse, Sinc, Maximal length pseudo random binary sequence and Chirp forms. Their features are presented in terms of a response simulation on an electrical network. Finally, a concluding comparison of the wideband signals is presented.

3.2 A Review on MFEIT

A number of arrangements have been investigated and described in the literature. Here we review comparative papers including their stated application interests. Demonstrations of significant frequency dependent behaviour in live tissue, in response to a sinusoidal signal, have motivated trials of multi-frequency EIT for medical applications [57, 56, 89]. Griffiths highlighted the advantages of multi-frequency imaging by utilising data obtained at two frequencies to enhance static images of an abdominal cross-section. Others report the use of MFEIT in order to characterise and aid diagnosis of particular disease conditions. Brown [12] has explored multi-frequency imaging of respiratory changes; Soni *et al* [61] have used MFEIT for breast cancer studies; and Romsauerova *et al* [90] have explored multi-frequency examination of an adult head. Few publications report industrially based trials. The potential of multi-frequency signals for industrial process tomography was reported by Beck *et al* [6]; Barlow *et al* [91] reported a study of a mixed mineral suspension using four-electrode impedance spectroscopy and concluded that it may be possible to reconstruct composition data map subject to the availability of adequate multi-frequency data over the desired frequency range. Zimmermann *et al* [92] has also reported the use of the MFEIT for soils and sediments analysis.

Table 3.1 provides a summary of reported MFEIT systems. The highest bandwidth features in the system reported by Hatler *et al* [16] while is able to sense data from signals whose frequency can be selected continuously up to 10 MHz. Most systems in the table employ similar excitation methods which are able to apply single source in a discrete sequential manner over the desired frequency range. Two systems are able to deliver measurements simultaneously at different frequencies. They have exploited compound sinusoidal signal as excitation. The Barcelona system [59] is reported as able to simultaneously excite and sense voltages at two selectable frequencies up to 1 MHz. The Sheffield Mk3.5 [93] system is support measurements at 30 discrete frequency points from 2 kHz to 1.6 MHz simultaneously. As indicated in the table 3.1 most MFEIT systems are intended for medical applications.

Table 3.1: Summary of available multi-frequency EIT system (M: Medical, I: Industrial, SS: Sequential Sinusoid and CS: Compound Sinusoid).

Authors	System name	Application	Frequency range	Method	Image/Sec
Riu[59]	Barcelona	M	8 kHz-1 MHz	CS	n/a
Blad[75]	Lund	M	1 kHz-1 MHz	SS	n/a
Zhu[66]	OXPACT-III	M	10 kHz-160 kHz	SS	25
Record[84]	Keele	M	10 kHz-3 MHz	SS	4.8
Casas[62]	TIE-4sys	M	10 kHz-250 kHz	SS	25
Dickin[41]	Manchester	I	8 kHz - 1 MHz	SS	25
Metherall[93]	Shefield MK3b	M	9.6kHz-1.2 MHz	SS	33
Primrose[63]	ITS 2000	I	75 Hz- 153.6 kHz	SS	25
Hartov[82]	n/a	M	1 kHz-1 MHz	SS	n/a
Wilson[79]	Shefield MK3.5	M	2kHz-1.6 MHz	CS	25
Arpinar[94]	n/a	M	10 kHz-100 kHz	SS	n/a
Yerworth [13]	UCLH Mark 1b	M	225 Hz and 77 kHz	SS	3
Halter [16]	n/a	M	10 kHz-10 MHz	SS	n/a
Qiu [95]	ITS M3000	I	1 kHz-15 MHz	SS	25
Wang [16]	ITS z8000	I	10 kHz-320 kHz	SS	1000

3.3 Design and Selection of Wideband Signals

The MFEIT systems are implemented with a consideration of data acquisition and processing, to satisfy application process dynamics. In medical applications dynamic issues may be concerned with patient motion, in the industrial case they arise , for instance, due to motion of component materials. Thus, the multi-frequency of any spectral study must be capable of delivering excitation and sensing data within the desired frequency range and within an acceptable time period so as to capture application dynamic data. The design of an optimal excitation signal is therefore highly desirable.

The MFEIT approaches which rely upon a staggered set of discrete frequency signals are intrinsically slow and this will inevitably limit applications to those which have correspondingly slow dynamic features. In contrast the speed and accuracy of modern electronic devices and new approaches offer the possibility of wideband signals which promise improved performance in multi-frequency systems. For optimal performance a signal must be selected and tailored to suit the application, including known aspects of the process used and its constituent materials. The type and specification of an excitation signal will influence its spectral content, the overall speed of data acquisition, the signal analysis necessary to recover useful measured data, and the hardware and software implementation and resulting system costs. The detailed design of the signal must address its type, bandwidth, spectral resolution, duration and amplitude.

The bandwidth of the excitation signal can be set from the process maximum and minimum relaxation time: τ_{max} and τ_{min}, respectively. Bandwidth $\Delta\omega$ for the excitation signal can then be inferred [96] from the inequality:

$$\frac{1}{\alpha_1 \tau_{max}} \leq \Delta\omega \leq \frac{\alpha_2}{\tau_{min}} \tag{3.1}$$

where α_1 and α_2 are arbitrary factors that include appropriate margins to set the bandwidth so that it exceeds that of the process.

The spectral resolution requirement is linked to the needs of a particular application in terms of the need to extract specific process changes or a material identification from a spectral signature.

Figure 3.1 shows a hierarchical classification of the multi frequency methods based on the type of excitation signal. The excitation can be applied either in form of discrete sequential Sinusoid waveform or using the simultaneous form. Most of the MFEIT systems reviewed above use the first approach: in which one value from a discrete set of signal frequencies covering the selected bandwidth is selected, and the data acquisition procedure is then repeated to cover the range, typically in increasing order. This method is the simplest form of MFEIT. The corresponding hardware structure can be a simple development on a conventional single frequency EIT system, provided that the electronic subsystems are programmable and are able to extend to the required bandwidth.

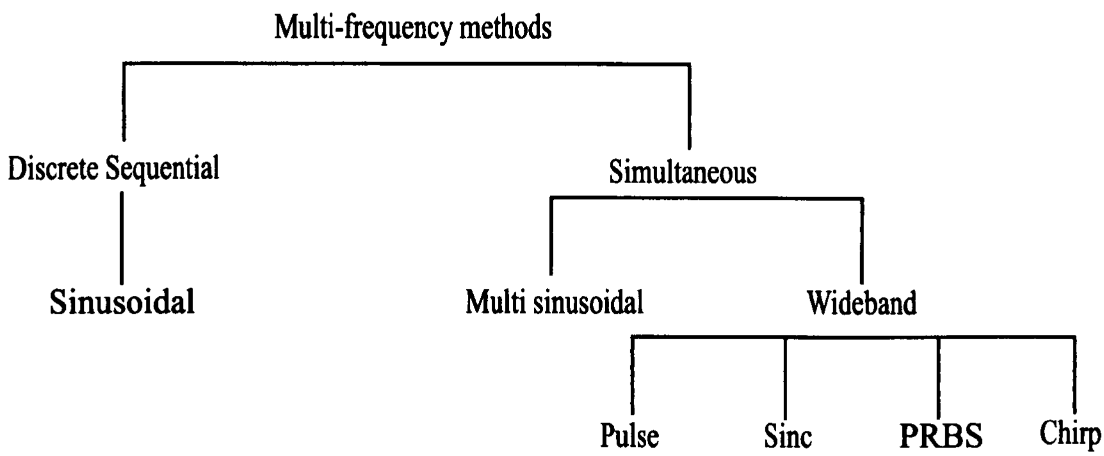

Figure 3.1: Hierarchy of multi-frequency methods.

A simple MFEIT, using the discrete sequential approach of figure 3.1, would therefore have to offer sufficient spectral points to provide the requisite resolution. Thus this method will be very time consuming and it is not applicable to process with fast dynamic.

To overcome these disadvantages the simultaneous MFEIT methods of figure 3.1 may be deployed. Their common approach is to deliver measurements over a spectral range coupled with the prospect of adequate dynamic performance. The Multi-sinusoid method noted in figure 3.1 is implemented by summing a number of separate sinusoidal signals at different frequencies to form either a composite signal, or a set of composite signals which can be used in sequence. Examples are described by [93] in their MK3a and MK3.5 systems. The wideband signals classified in figure 3.1 have the intrinsic capability to deliver broad spectral information. These signals include: Pulse, Sinc, Pseudo random binary sequence (PRBS) and Chirp.

3.4 Signals for Simultaneous Multi-frequency Excitation

The features of the MFEIT simultaneous methods summarised in figure 3.1, and their advantages and disadvantages, are explored in detail in the following sections. The first sections deals with the Multi-sinusoid method and the following sections address the four wideband methods: namely the Pulse, Sinc, PRBS, and Chirp methods respectively.

3.4.1 Multi-sinusoid Signal

The Multi-sinusoid signal is a deterministic, periodic signal produced by the summation of several sinusoid waveforms at desired frequencies. It can be defined as:

$$s(t) = \sum_{n=1}^{N} A_n \cos(\omega_n t + \phi_n) \tag{3.2}$$

where N is the number of frequency components, A_i is the amplitude, ω_n is angular frequency and ϕ_i is phase at each sinusoidal component. The Fourier transform of this signal is:

$$S(\omega) = \pi \sum_{n=1}^{N} A_n[\delta(\omega - \omega_n) + \delta(\omega + \omega_n)] \tag{3.3}$$

This signal therefore delivers a flat spectrum at each of the different frequencies provided that they have equal amplitudes. However, in the time domain, due to frequency and phase differences between sinusoidal components, the summed waveform contains large peaks and low amplitude points. These features can be described for a specific waveform in terms of its crest factor, defined in [97] as:

$$Cr = 10 \log \left(\frac{S_{max} - S_{min}}{2E_{rms}} \right) \tag{3.4}$$

where $E_{rms} = \sqrt{\sum_{n=1}^{N} A_n^2/2}$ is RMS value and S_{max} and S_{min} are the largest positive and negative values of $s(t)$. From equation (3.4) the Multi-sinusoid signal has a bigger crest factor C_r than that of the original components. A high crest factor causes problems in both excitation (input) and measuring (output) subsystems. In the excitation subsystem peak amplitudes may exceed the dynamic range of the input electronics. It may not always be possible to resolve this by scaling because of the resulting degradation of the small amplitudes. In the measurement subsystem a high crest factor degrades SNR of ADC stage which will probably be used. Figure 3.2 shows an example input and output voltage waveform from a simulation first order low pass RC network with a relaxation time τ of 10^{-5} s. The input signal was the composite signal formed by summing 20 sinusoidal waveforms with frequencies from 10 kHz to 200 kHz with zero initial phase difference in equation (3.2). In this example, the crest factor of the Multi-sinusoid waveform increased from 3 dB for each of the original components to 11.93 dB.

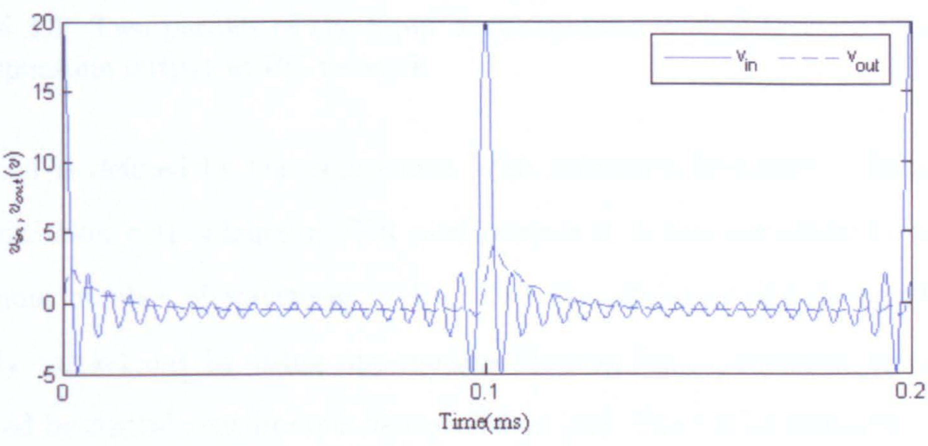

Figure 3.2: Two periods of the input multi-sinusoid and output of RC network.

Due to these impacts, the minimization of crest factor is important. Practical methods to minimize crest factor have been described in [98, 97, 99]. For instance Schroeder [98] presents a simple expression to determine suitable phase values for such equal amplitude sinusoid components, given by:

$$\phi_n = \phi_1 - \pi \frac{n^2}{N}; \qquad 2 \leq n \leq N \tag{3.5}$$

where, ϕ_n is the phase of n^{th} component. Figure 3.3 depicts the effect of applying the Schroeder method to the example described above whose input-output waveform is shown in figure 3.2. As illustrated the crest factor is reduced to 4.4 dB, a 7.53 dB reduction. In Multi-sinusoid excitation the measurement

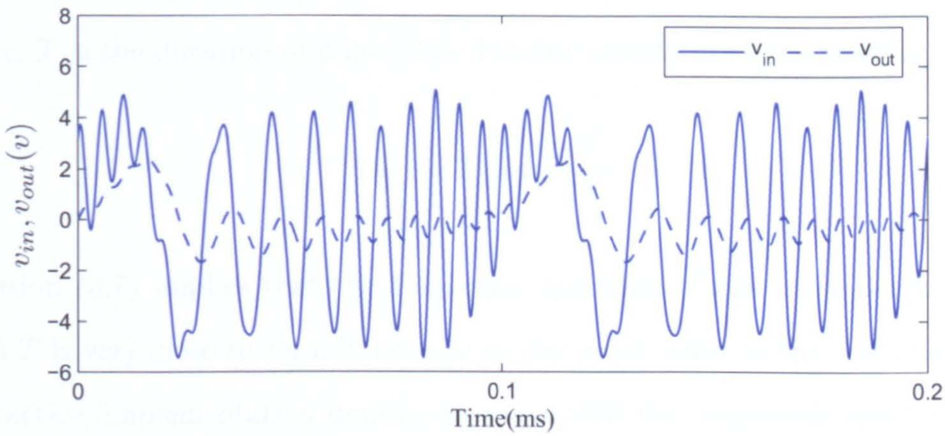

Figure 3.3: Two periods of the input multi-sinusoid with Schroeder phase and corresponding output of RC network.

duration is defined by the component with minimum frequency. To perform demodulation with adequate SNR performance it is also necessary to inject a minimum number of waveform cycles. The demodulation of this waveform is usually carried out by using appropriate filtering for a particular component followed by digital synchronous demodulation [88]. The major limitation of this signal is that it is not possible to add arbitrary number of sinusoidal waveforms together. A solution to this drawback was employed in [79]. In their MK3.5 system a hybrid method of simultaneous and sequential excitation was employed to increase the number of excitation frequencies. This approach increases the total measuring duration and the system complexity needed to implement the staged injection. Due to limitations mentioned above, high frequency resolution may not be achievable with this type of excitation. This disadvantage makes the multi-sinusoid waveform less attractive for the applications that need fine spectral information.

3.4.2 Pulse Signal

The rectangular pulse is defined [100] by:

$$s(t) = \begin{cases} 1, & |t| < T/2 \\ 0, & |t| > T/2 \end{cases} \tag{3.6}$$

where, T is the duration of pulse. The Fourier transform of the pulse is:

$$S(\omega) = TSinc(\frac{\omega T}{2\pi}) \tag{3.7}$$

Equation (3.7) implies that the frequency spectrum of the pulse becomes flat when T is very close to zero, in essence as the pulse tends to the delta function. In practice, implementation limitations mean that the magnitude spectrum will decrease with frequency. Figure 3.4 shows time and frequency domain response of a low pass network with relaxation time τ of 1 ms to a rectangular pulse with duration T of 1 ms. The function of equation (3.7) and the example shown in figure 3.4 demonstrate that the Pulse signal contains all frequencies within the range: $[\frac{-1}{T}, \frac{1}{T}]$ Hz. They also indicate the inverse relationship between the pulse duration and its bandwidth. From a signal design viewpoint they demonstrate that, to achieve a specified bandwidth, the duration of pulse must be modified, which in turn will affect the signal energy. To improve SNR it is therefore necessary to increase the amplitude of the pulse. In practice, this may not be always possible due to hardware dynamic range limitations and possible non-linear effects; the application process also may impose amplitude limitations. A further design disadvantage is the difficulty of adjusting the bandwidth for desired frequency range. The Pulse signal also includes a non-zero DC component which

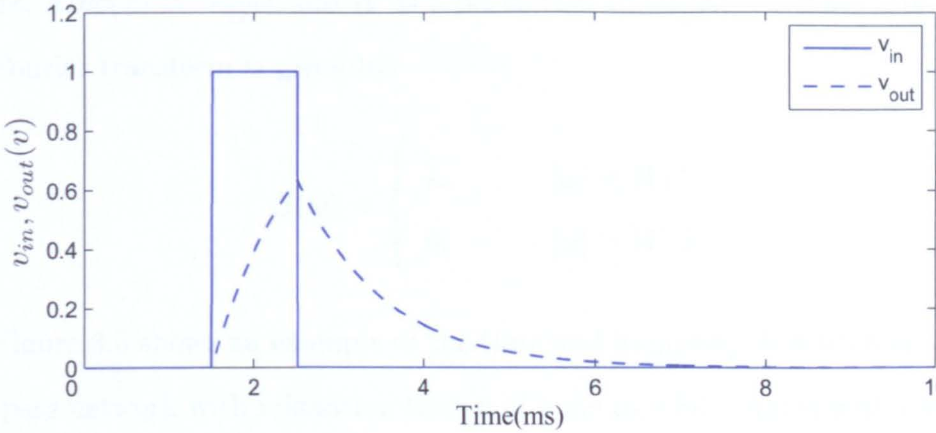

(a)

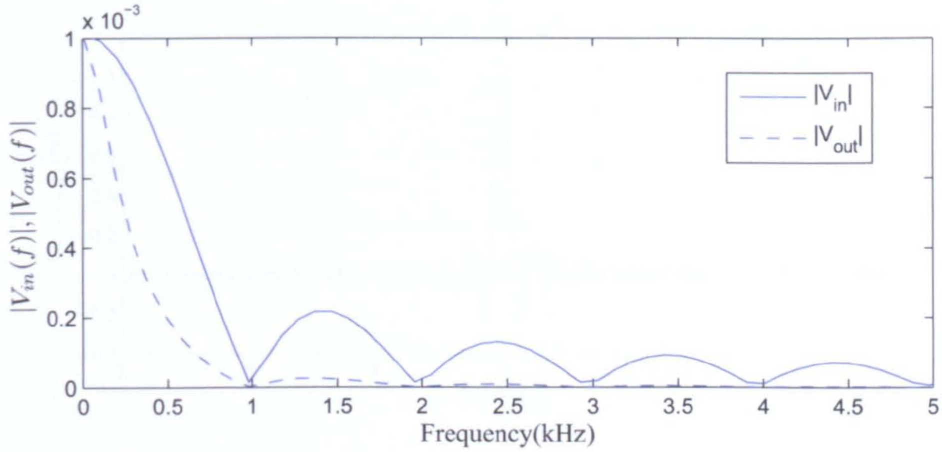

(b)

Figure 3.4: Pulse Excitation: time-domain waveforms (a) and frequency-domain magnitude (b).

may be undesirable. Several of these disadvantages may be avoided through the use of a modulated form of the pulse signal described in section 3.4.5.

3.4.3 *Sinc* Signal

The inverse relation of time and frequency domain suggests that the *Sinc* function can also be employed as an excitation in EIT system. This excitation function can be written [100] as:

$$s(t) = \frac{W}{2\pi} Sinc(\frac{Wt}{2\pi}) \tag{3.8}$$

where, $Sinc(x) = \frac{sin(\pi x)}{\pi x}$ and W is a parameter to adjust the main lobe of $s(t)$. Its Fourier transform is given by:

$$S(\omega) = \begin{cases} 1, & |\omega| < W/2 \\ 0, & |\omega| > W/2 \end{cases} \tag{3.9}$$

Figure 3.5 shows an example of the time and frequency domain response of a low-pass network with relaxation time τ of 1 ms to a Sinc signal with parameter W value of $(2\pi \times 10^4)$. As shown the desired flat frequency response is achieved

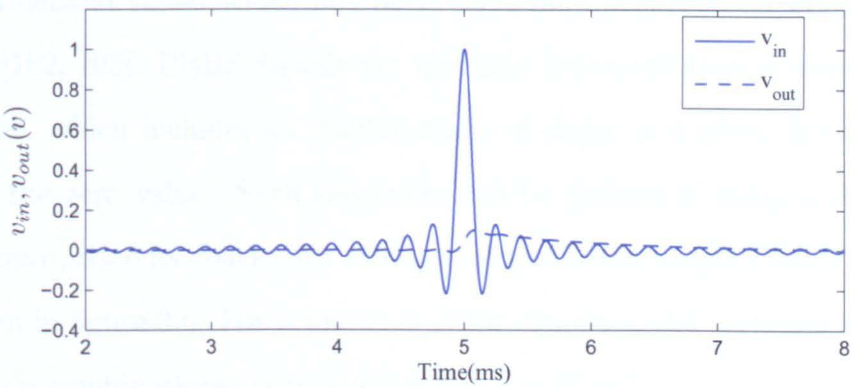

(a)

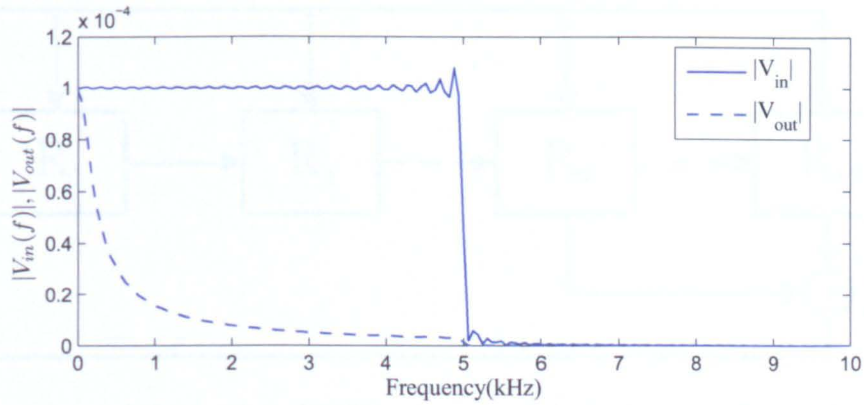

(b)

Figure 3.5: Sinc Excitation: time-domain waveforms (a) and frequency-domain magnitude (b).

and this offers a major advantage over pulse excitation. Unfortunately the Sinc signal has similar disadvantages to that of the Pulse. When W is increased (in the limit to infinity) the amplitude of the main lobe of the Sinc signal increases, but its width is reduced. In the frequency domain $S(\omega)$ is unity for all frequencies in the bandwidth. As noted above, it is not possible to make W arbitrarily large. Hence in terms of signal design it may be difficult to adjust the bandwidth and also obtain a requisite value of SNR by increasing the amplitude of the Sinc signal. Implementation is straightforward; for example as suggested in the design in [101].

3.4.4 Pseudo Random Binary Signal

The pseudo random binary sequence signal (PRBS) is a well known, deterministic, wideband signal which has been commonly proposed for system identification [102, 103]. PRBS Signals are typically generated from a maximal length sequence, which includes all combinations of digits in a given modulo-2 word, except the zero value. Such sequences can be generated using a shift register with appropriate feedback. An example of maximum length PRBS(ML-PRBS) is shown in figure 3.6. For n binary register elements, the sequence length L (of modulo-n combinations) is thus given by: $L = 2^n - 1$.

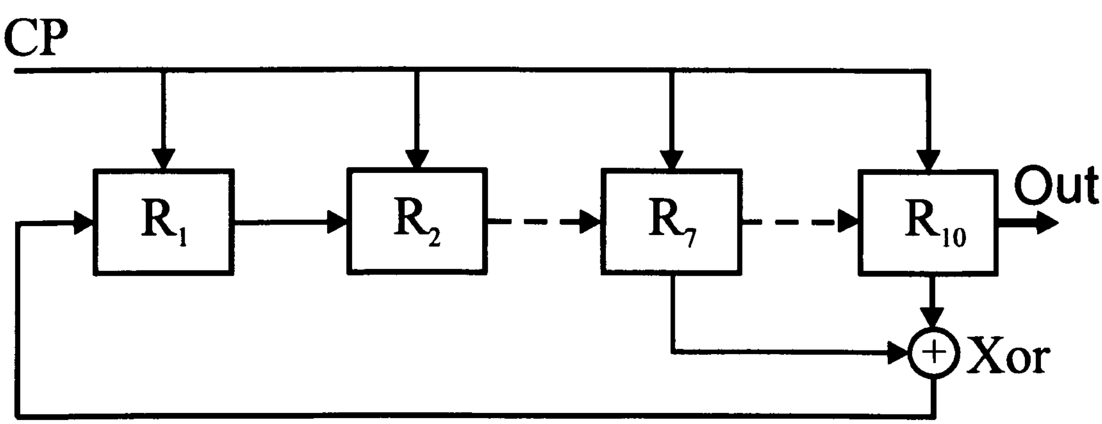

Figure 3.6: An ML-PRBS generator block diagram for n=10.

Since all combinations, except one, are present the average amplitude of the sequence is close to zero. The signal also has the valuable minimum crest factor of unity. In signal design terms the characteristics of the maximal length PRBS (ML-PRBS) signal can therefore be controlled by n and the sampling frequency f_s as determined by Nyquist considerations. The frequency range limits, f_{max}

and f_{min} can thus be calculated by:

$$f_{max} = \frac{f_s}{2} \tag{3.10}$$

$$f_{min} = \frac{f_s}{L} \tag{3.11}$$

The minimum frequency is also the frequency resolution. The bandwidth of this waveform covers a range from a very low frequency to half of f_s . Thus, concentrating the energy of signal on the desired frequency band is not possible with the ML-PRBS. As an example figure 3.7 shows the response of a RC network with a relaxation time τ of 10^{-5}ms to a ML-PRBS signal generated with parameters of sampling frequency f_s of 2 MHz generated from a maximal length sequence of n of 10. The most important advantage of ML-PRBS is that its

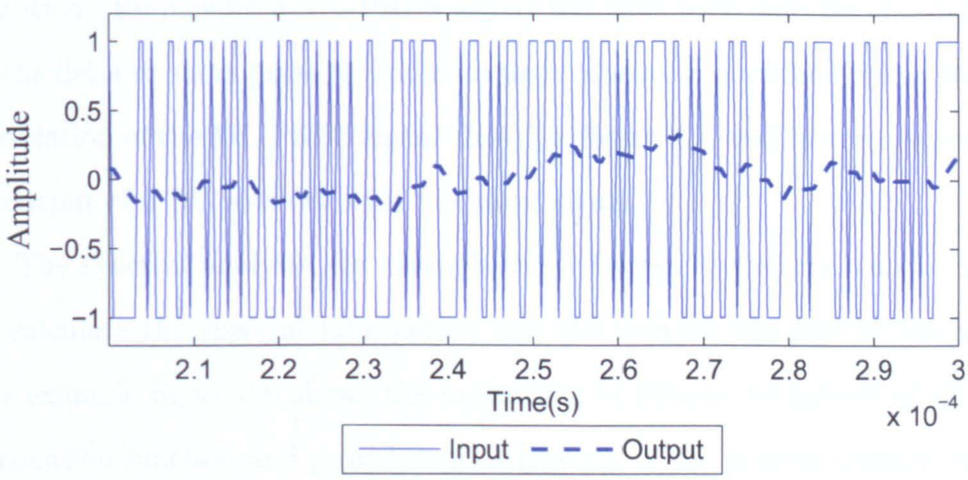

Figure 3.7: A portion of the input ML-PRBS and corresponding response of a RC network with $\tau = 10^{-5}$.

autocorrelation function is a close approximation of the delta function providing that the sequence is long. It can be shown that the cross-correlation, $R_{xy}(t)$ of input with output signal can be defined as:

$$R_{xy}(t) = h(t) * R_{xx}(t) \tag{3.12}$$

where, * denotes linear convolution and $R_{xx}(t)$ is the autocorrelation function. For the ML-PRBS signal $R_{xx}(t) = \lambda\delta(t)$. By substituting this expression in equation (3.12) the impulse response of the process can be determined [102, 104] as:

$$h(t) \approx \frac{1}{\lambda} R_{xy}(t) \tag{3.13}$$

where, λ is given by : $\lambda = \frac{1}{L}\sum_{n=1}^{L} R_{xx}(t)$. This is the simplest method leading to a good estimation of the process, provided that the sequence is long. It may be also possible to use methods based on the least square minimization [103]. Since this would be time consuming for a MFEIT system, the method based on equations (3.12) and (3.13) may be preferred.

Since the ML-PRBS signal delivers more energy to the process during measurement the method should offer a good SNR. The SNR can also be improved by using a longer length sequence at the expense of an increase in measurement duration. Employing a ML-PRBS signal will thus overcome the disadvantages of the delta or short pulse function discussed above. Figure 3.8 depicts the autocorrelation of the ML-PRBS signal shown in figure 3.7, and the cross-correlation of output of a RC network with the input signal.

The spectral analysis, for example via a Fourier transform, can be utilized to calculate the spectral information and the transfer function of the process. For example figure 3.9 shows the magnitude of Fourier transform of the cross-correlation function and provides an estimation of the process transfer function from equations (3.12) and (3.13).

Implementation of the ML-PRBS signal is straightforward. As it is periodic, it may be possible to perform a test with a signal composed of one sequence period. The duration of the measurement for one period $T = \frac{L}{f_s}$, varies depending on the length of the sequence and sampling frequency. The sequence length must be long to produce the impulsive autocorrelation function upon which the estimation process depends. This may produce a disadvantage in a long measurement time. A further disadvantage is that it is not simple to adjust the

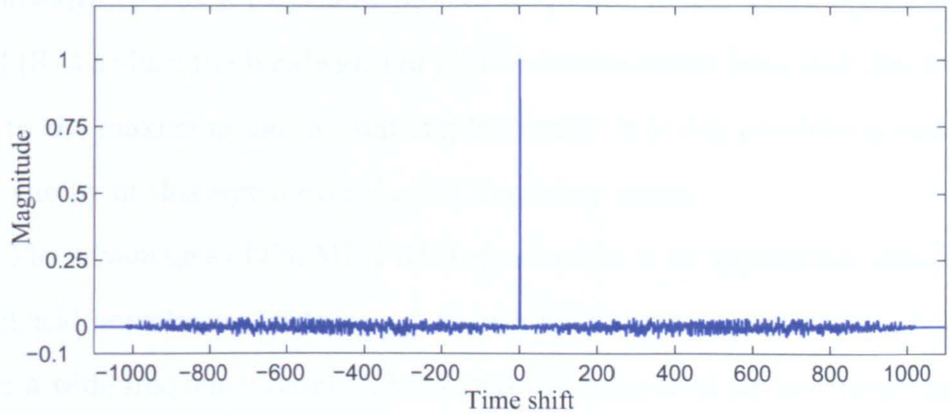

(a)

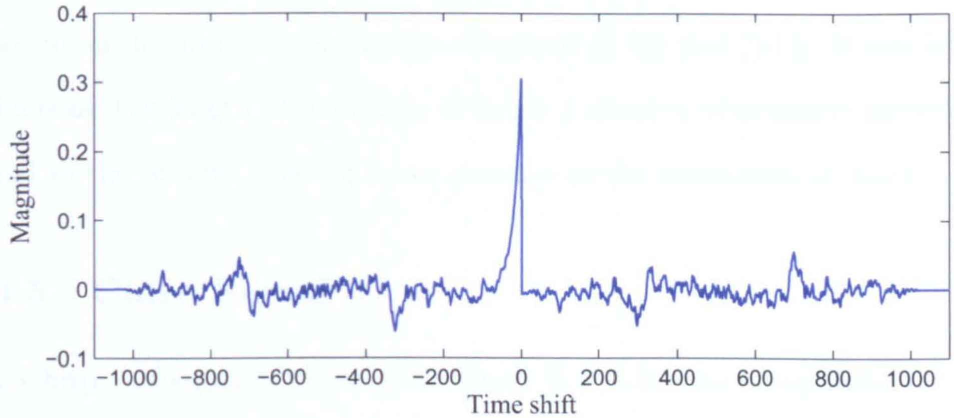

(b)

Figure 3.8: Correlation functions: auto correlation of input (a) and auto cross correlation of input with output of RC network (b).

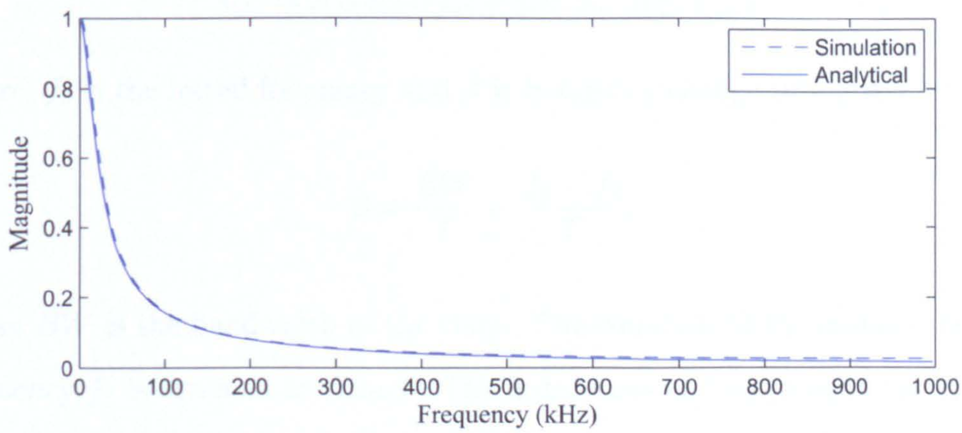

Figure 3.9: Analytical and simulated magnitude of the transfer function of the RC network using the Fourier transform of the cross correlation shown in the figure 3.8(b).

bandwidth to suit a particular process frequency range. From equations (3.10) and (3.11), since the bandwidth of this excitation starts from very low frequency up to the maximum half a sampling frequency, it is not possible to concentrate the energy of this signal over desired frequency range.

The advantages of the ML-PRBS signal make it an appropriate candidate for electrical impedance spectroscopy, when simultaneous measurements are needed over a wide frequency range. This signal has been used for electrical impedance spectroscopy in studies of long bone features by [105]. For accurate estimation of the transfer function for each measurement channel in an EIT imaging system, based upon the processes defined by equations (3.12) and (3.13), it may necessary to increase the length of sequence, or apply a number of sequence periods of the signal to the process, leading to an increase in the measurement time.

3.4.5 Chirp Signal

The Chirp, or frequency modulation signal, is well-known in sophisticated sensing applications such as Radar [106]. The appropriate forms of this signal for use with EIT are linear and logarithmic Chirp. The linear form of this signal is given by:

$$s(t) = A\cos[2\pi(f_0 t + \tfrac{1}{2}\beta t^2)], \quad 0 \leq t \leq T \tag{3.14}$$

where, f_0 is the initial frequency and β is frequency change rate given by

$$\beta = \frac{BW}{T} = \frac{f_f - f_0}{T}. \tag{3.15}$$

where BW is the bandwidth of the chirp. The equation (3.15) ensures the final frequency f_f is attained at time T. The instantaneous frequency of the chirp is defined by:

$$f_i = \frac{1}{2\pi}\frac{d\phi(t)}{dt} = f_0 + \beta t \tag{3.16}$$

where $\phi(t)$ is the phase of the chirp. The equation (3.16) indicates the linear variation of the frequency over the Chirp duration, T, as shown in figure 3.10a.

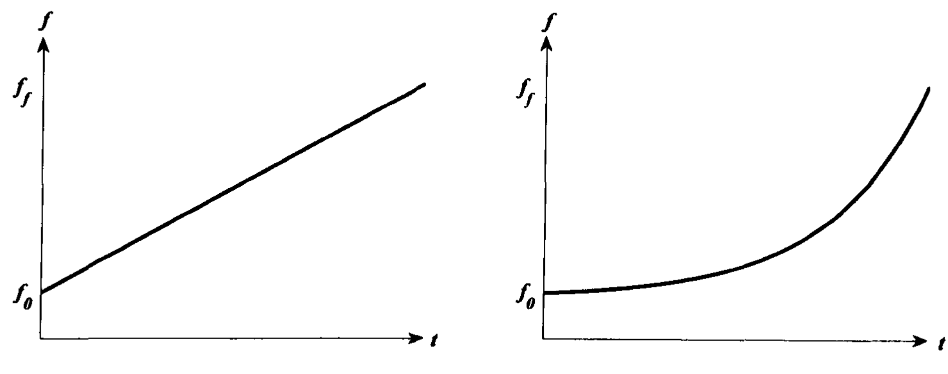

(a) (b)

Figure 3.10: Time-frequency characteristics of Chirp: linear Chirp (a) and logorithmic Chirp(b).

The logarithmic form of the Chirp is given [39] by:

$$s(t) = A\cos[\tfrac{2\pi f_0}{\log(\beta)}(\beta^t - 1)], \quad 0 \le t \le T \tag{3.17}$$

where frequency change rate is: $\beta = (\frac{f_f}{f_0})^{\frac{1}{T}}$. The instantaneous frequency of the logarithmic Chirp is defined by:

$$f_i = f_0\beta^t \tag{3.18}$$

This equation indicates the logarithmic variation of the frequency over the Chirp duration, T, as shown in figure 3.10b.

Both Chirp forms described by equations (3.14) and (3.17) express an up-sweep Chirp, where $f_0 < f_f$, but for down-sweep Chirp $f_0 > f_f$. The Chirp parameters may thus be designed so that it continuously sweeps the desired frequency range.

In the Chirp waveform the modulation spreads the energy over the desired bandwidth. This eliminates the drawbacks of other waveforms in the previous sections. The crest factor of this waveform is $\sqrt{2}$, which is equal to that of the sinusoidal signal. Figure 3.11a shows a linear Chirp signal having a frequency bandwidth from 10 kHz to 510 kHz which is swept in a duration of 1 ms; and its response in a low pass RC network having a relaxation factor τ of 10^{-5}s, as shown in 3.11b. This verifies that the response Chirp directly gives the frequency response.

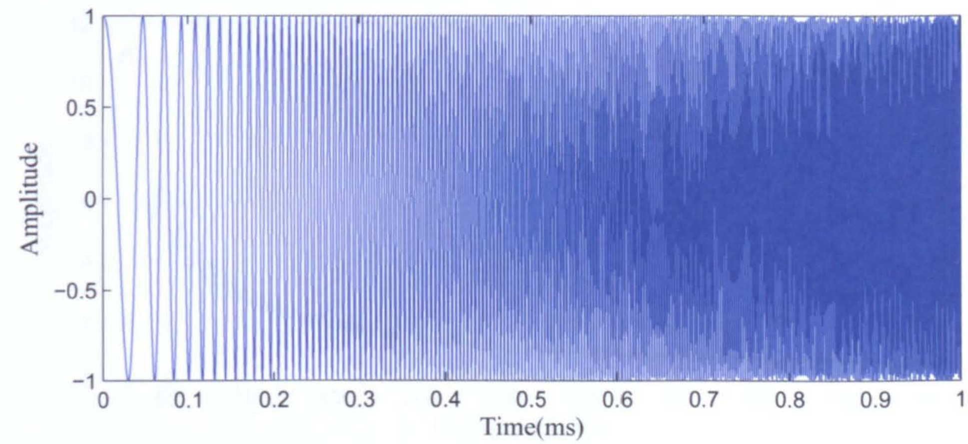

(a)

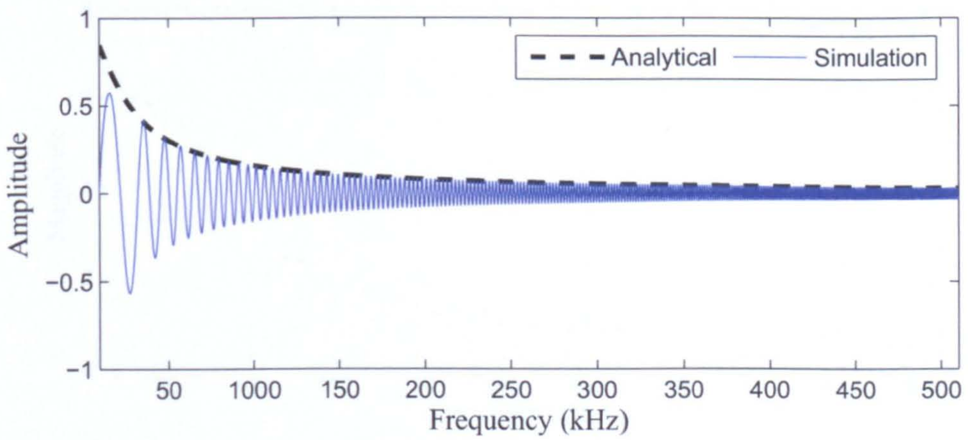

(b)

Figure 3.11: Chirp Signal (a) and the response of RC network (b): simulated magnitude (solid) and the magnitude of transfer function (dashed).

Expression (3.1) may effectively be used to design the Chirp bandwidth. The maximum relaxation time of the process will provide a key factor for the design of the maximum value of the signal duration. The Chirp signal offers major flexibility in essence through its time-bandwidth product relationship. As inferred in (3.14) this allows the desired bandwidth to be swept linearly which will define a minimum value for the signal duration. Increasing T value enhances spectral resolution. This effect of the modification of T on spectral resolution is illustrated in figure 3.12. This shows the Fourier transform of the response function of a Chirp signal that sweeps through the same frequency band from 10 kHz to 510 kHz in durations of 1 ms and 0.1 ms.

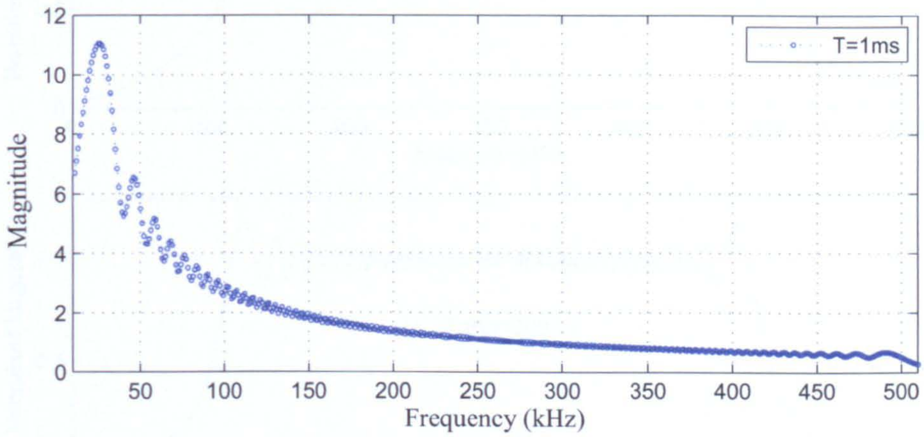

(a)

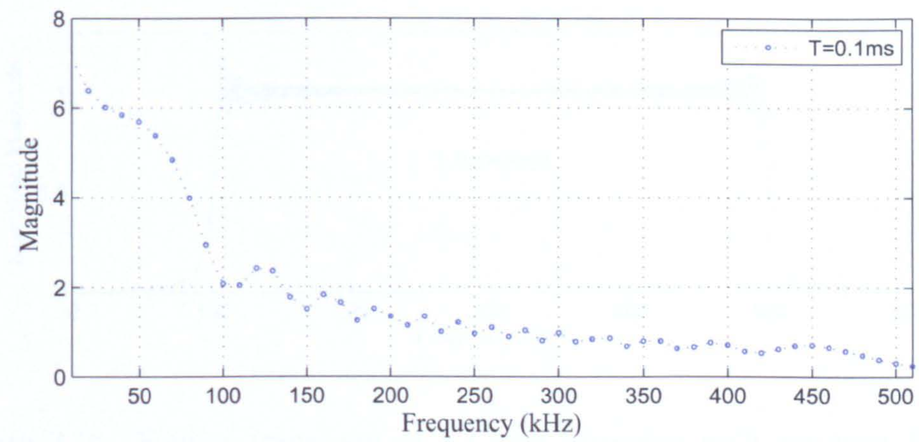

(b)

Figure 3.12: Fourier transform of RC response for Chirp durations of 1ms (a) and 0.1ms (b).

Increasing the duration T from the minimum also results in a flatter spectrum. For instance, figure 3.13 demonstrates this fact for three different time-bandwidth products. All spectra of Chirp spread from f_0 to $f_0 + BW$, but the Chirp with greater time-bandwidth product shows flatter response.

Synthesis of a Chirp signal is straightforward using commonly available large scale integrated devices, for example Analog Devices AD9852 digital synthesizer[107].

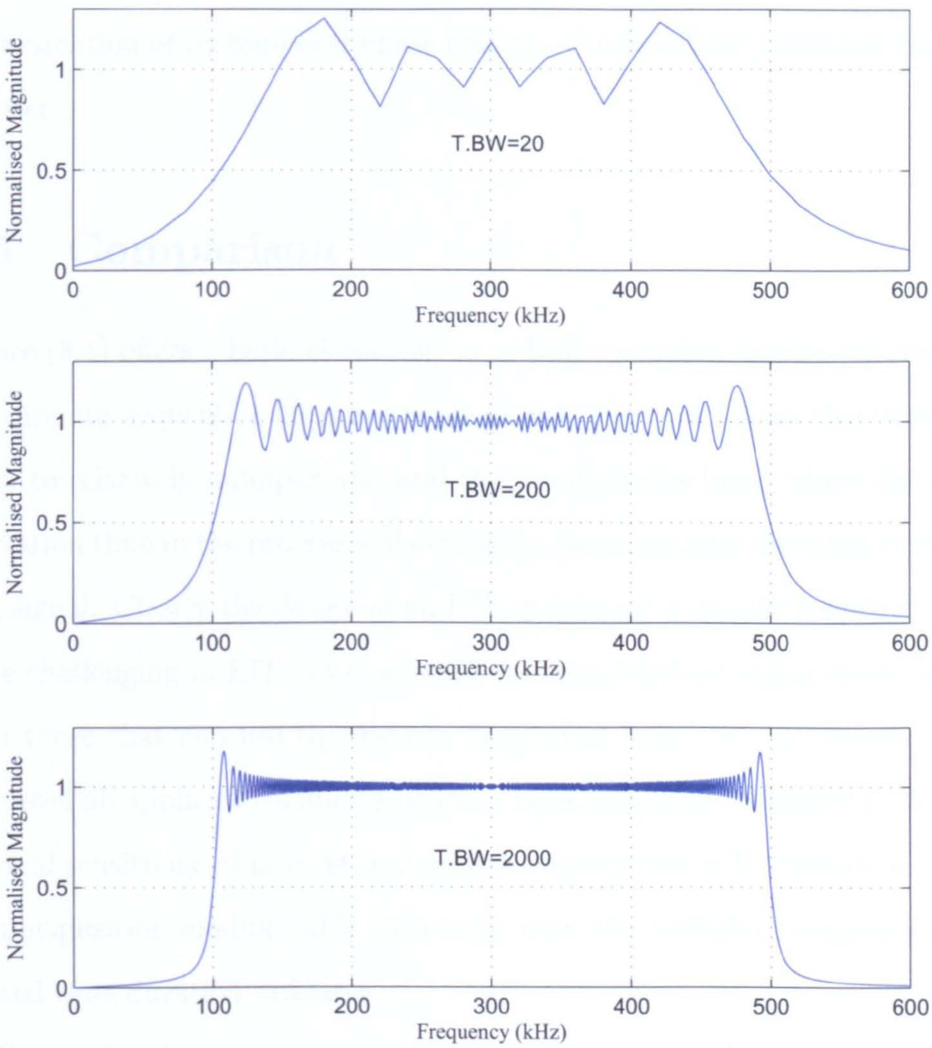

Figure 3.13: Fourier transform of a Chirp sweeping with constant BW from 100 kHz to 500 kHz with three different time-bandwidth product, T.BW=20, 200, 2000.

Chirp excitation offers advantages of flexibility in speed, duration and frequency content of the process measurements. This signal form allows measurements in a single continuous sweep over a specified bandwidth in a selected (if realizable) measurement interval. Since Chirp has the capability of delivering the spectral data in short duration, it decreases the error due to the time-variant events in the instant of the data acquisition.

As this signal is non-stationary, time-frequency analysis methods such as short time Fourier transform (STFT) and wavelet transform (WT) may be used for the determination of temporal amplitude and phase for the purpose of the reconstruction of tomographic images. Time-frequency features of Chirp and the extraction of its temporal phase and amplitude will be presented in the next chapter.

3.5 Comparison

Figure (3.1) offers a basic classification of EIT excitation signals into two forms: the discrete sequential form for applications where real-time requirements are likely to relatively unimportant; and the simultaneous form, where the dynamic relaxation time in the process will determine the maximum duration of an excitation signal. Clearly the design of an EIT system for a specific frequency range is more challenging in EIT systems using the simultaneous signal excitation form, than those that can use the discrete sequential form. At the system architecture level all applications must support a basic sampling frequency to deliver the spectral sensitivity of interest, but simultaneous forms will typically require fast data acquisition modules able to comply with this sampling requirement in the limited time duration available.

For applications requiring a simultaneous excitation form the Multi-sinusoid signal may be the first consideration. For example, in applications where the process is composed of a number of materials each of which has specific and distinct a priori electrical sensitivity characteristics of a spectral nature. Hence a Multi-sinusoid signal may be considered to estimate this information at the corresponding number of discrete frequencies. It suffers from the disadvantage of high crest factor. Also, although this method has the advantage of a flat spectrum in magnitude terms across the discrete spectral lines, it cannot provide fine spectral information over the wide frequency band which brackets these lines, to expose other process information.

Where a simultaneous excitation form is required for an application over a wide frequency range and with a high spectral resolution over this band, a wideband signal must be deployed. A group of candidate excitation signals have been considered including: Pulse, Sinc, PRBS, and Chirp. These are all shown intrinsically to support the wideband frequency requirement but each signal has specific advantages and disadvantages.

The simple Pulse signal, considered as a foundation, is easily implemented in principle but suffers from disadvantages that will limit its application in practical EIT systems. These include the difficulty of achieving an adequate SNR, poor bandwidth adjustability and a non-flat spectrum. The Sinc signal form does offer a flat spectrum but with the same disadvantages as the Pulse signal.

The ML-PRBS signal is a more useful candidate for WEIT excitation. It is easily implemented electronically and has no signal amplitude disadvantages. Its sampling frequency is also a basic adjustable parameter. Its duration is simply predicable from the sampling frequency and the maximal sequence length. To gain adequate wideband properties for a given application the design process must take the length of the sequence into account. In essence the sequence must be relatively long to form a flat spectral characteristic. Since the sequence length is related to the modulo-n power of 2, the control of sequence length and hence signal duration is relatively coarse and inflexible. This may produce an unacceptably long measurement time. As in the case of the Pulse and Sinc signals the ML-PRBS also has the disadvantage of inflexibility in adjustment of bandwidth to suit the required frequency range. A key requirement, as part of the EIT reconstruction process, is the provision of sufficient data to provide an accurate estimation of the transfer function for each measurement channel using (3.12) and (3.13). To fulfil this requirement it may be necessary to increase the data obtained and this can be achieved in one of two ways. Firstly, to further increase the sequence length, or secondly, to use multiple sequences in each excitation signal. Both of these solutions will increase the duration of the excitation signal. Subject to real-time constraints these steps may be acceptable in which case a ML-PRBS signal may provide a good candidate.

The final signal is the Chirp. As reviewed above this signal form offers major flexibility in terms of parameter design for wideband measurement. It also has the capability to concentrate excitation energy in a desired frequency range and hence allows the design process to efficiently address SNR issues. Although its implementation is more complicated than other candidates, high speed electronic devices are available that can simply be incorporated into EIT systems. As It will be illustrated, the chirp has the disadvantage of increasing the complexity in the downstream analysis of measured data in order to the extraction of image reconstruction data, but this offset by its significant advantages. The Chirp signal thus offers major advantages for WEIT systems which target the most demanding real-time applications which exhibit broad spectral characteristics.

3.6 Conclusion

The chapter has presented a review of excitation signals in the MFEIT systems with a focus on the key factors of signal bandwidth, test duration and type of excitation signal. It examines a set of signal candidates whose features are suitable for use in MFEIT systems. Their dynamic application characteristics are assessed using a simple RC network simulation. In a specific application several signal forms may be useful, but it is likely that there will be an optimal selection that enhances temporal and spectral information, and at a practical level also offers efficient implementation. The chapter presents a concluding comparison and demonstrates that the utilisation of an appropriate wideband signal such as Chirp can deliver a requisite measurement speed while providing major flexibility to tailor the measurement duration, bandwidth and frequency resolution.

Chapter 4

Chirp Signal Analysis

4.1 Summary

In the previous chapter, the chirp signal has been selected as the primary excitation signal in this research. In this chapter the extraction of the required parameters from the chirp signal in order to perform image reconstruction are discussed. For this, two types of time-frequency analysis consisting of short-time Fourier transform (STFT) and wavelet transform (WT) are described. The algorithms developed for the purpose of the accurate extraction of temporal values are presented and simulation results are demonstrated.

4.2 Time-frequency Analysis

In a WEIT system, a wideband signal is needed and, thus, the measured data set is wideband and contains the spectral information over the frequency range of interest. Figure 4.1 illustrates a typical measurement channel for a WEIT system using a chirp as excitation signal. In this figure $i_{in}(t)$ and $v_{out}(t)$ denote the excitation and measured chirp signals, respectively. The transfer admittance $Y(j\omega)$ of the channel can also be estimated by:

$$Y(j\omega) = \Re[Y(j\omega)] + j\Im[Y(j\omega)] = \frac{I_{in}(j\omega)}{V_{out}(j\omega)} \tag{4.1}$$

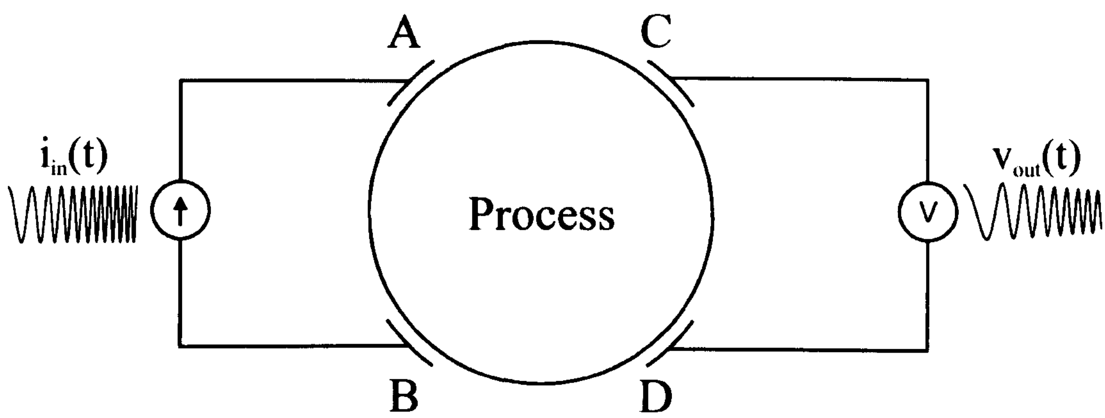

Figure 4.1: A typical WEIT system measurement channel using a chirp signal.

here $I_{in}(j\omega)$ and $V_{out}(j\omega)$, correspond to $i_{in}(t)$ and $v_{out}(t)$, respectively. The critical aspect of the use of chirp excitation is the rigorous analysis of the resulting wideband measurements for the purpose of precise extraction of their temporal amplitude and phase values. This gives the necessary data sets in order to reconstruct the admittivity distribution of the process over the desired frequency range.

The objective of this chapter is to investigate suitable methods and algorithms for the purpose of precise extraction of chirp temporal values. Since this signal is non-stationary, time-frequency analyses can be deployed [108]. Several different time-frequency methods are found in the literature. The detailed theory of such methods can be found, for instance, in [109, 108, 110, 111]. In this research, two common techniques in time-frequency analysis consist of STFT and continuous wavelet transform (CWT) are examined to extract the precise amplitude and phase of the chirp signal. To investigate the time-frequency characteristics of a signal using STFT, an analysing window with constant length is slid over the signal. In the wavelet transform this is conducted by scaling a mother wavelet. By this capability, wavelet transform offers a more powerful approach for the purpose of analysing signals with rapid frequency changes [108] such as different types of chirp signal.

In the following, these above methods are briefly described and the results of chirp signal analyses by developed algorithms are demonstrated.

4.3 Short-time Fourier Transform (STFT)

4.3.1 STFT

STFT (or Windowed Fourier transform) of a signal $S(t)$ is defined [108, 110] by:

$$Sf(b,\omega) = \int S(t)g(t-b)e^{-i\omega t}dt \tag{4.2}$$

where $g(t)$ is a real symmetric window and $S(t) \in L^2(\mathbb{R})$ is a finite-energy signal, where $\int |S(t)|^2 < +\infty$. In equation (4.2), an equal analysing window $g(t)$ is translated across the signal $S(t)$, providing time localization, and the frequency components of the signal are analysed by means of Fourier transform in the neighbourhood of $t = b$, which this gives localization in the frequency domain. By this procedure, the STFT overcomes the drawback of the Fourier transform to provide time information. The time and frequency resolution of the STFT is further discussed in the next section.

4.3.2 Time-frequency Resolution of STFT

To evaluate the time-frequency resolution of different types of time-frequency methods a quantative measure is utilised in the time and frequency domains. The time resolution, σ_t, of a function, $g(t) \in L^2(\mathbb{R})$, is expressed by its standard deviation from its mean time $< t >$, and given by [109, 112]:

$$\sigma_t^2 = \frac{\int_{-\infty}^{+\infty} (t- < t >)^2 \, |g(t)|^2 \, dt}{\int_{-\infty}^{+\infty} |g(t)|^2 \, dt} \tag{4.3}$$

where $< t >$ is

$$< t >= \frac{\int_{-\infty}^{+\infty} t \, |g(t)|^2 \, dt}{\int_{-\infty}^{+\infty} |g(t)|^2 \, dt} \tag{4.4}$$

Similarly, in the frequency domain the resolution σ_ω is defined by:

$$\sigma_\omega^2 = \frac{\int_{-\infty}^{+\infty} (\omega - <\omega>)^2 \, |G(\omega)|^2 \, d\omega}{\int_{-\infty}^{+\infty} |G(\omega)|^2 \, d\omega} \tag{4.5}$$

where $G(\omega)$ is the Fourier transform of $g(t)$ and $<\omega>$ is mean frequency and defined by:

$$<\omega> = \frac{\int_{-\infty}^{+\infty} \omega \; |G(\omega)|^2 \, d\omega}{\int_{-\infty}^{+\infty} |G(\omega)|^2 \, d\omega} \tag{4.6}$$

Based on the uncertainty principle [109, 110]:

$$\sigma_t \sigma_\omega \geq \frac{1}{2} \tag{4.7}$$

It states that it is not possible to obtain an arbitrarily sharp analysis in both domains simultaneously. However, the product of σ_t and σ_ω is always constant. Therefore, having a smaller value of σ_t leads to degradation of frequency resultion, σ_ω, or vice versa. A Gaussian window can only satisfy the equality in equation (4.7).

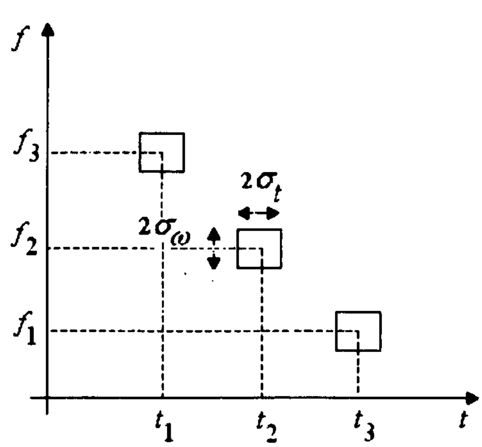

(a)

Figure 4.2: Time-frequency resolution of STFT.

The time and frequency resolution of the STFT is pictorially illustrated in figure

4.2. The product of time and frequency resolution is independent of the size of the window. Since the size of the analysing window remains constant, the resolution of this transform is constant over the time or frequency domain. The time and frequency resolution of the STFT is also demonstrated in 4.3.

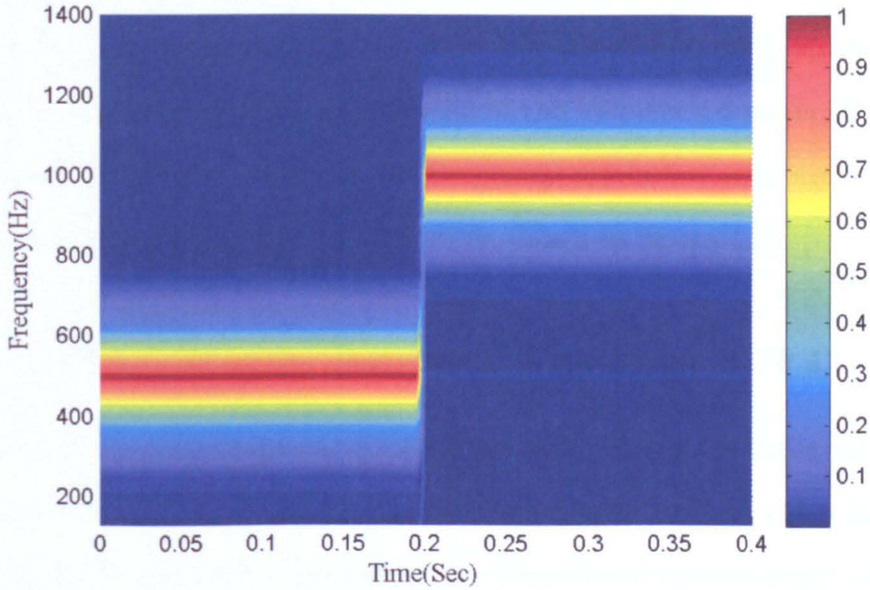

(a)

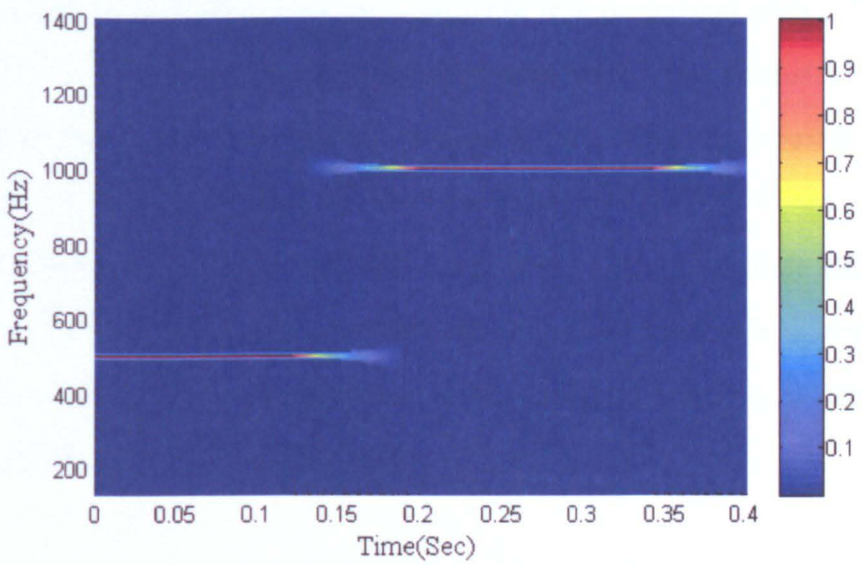

(b)

Figure 4.3: Spectrogram of a sinusoidal signal consisting of 500 Hz and 1 kHz frequency components using Gaussian window with duration of W=5 ms (a) and 80 ms (b), the colourbar shows the magnitude of spectrogram.

For this, the square of the STFT (or *spectrogram*) of a signal consists of two non-overlapping sinusoids of frequencies 500 Hz and 1000 Hz was calculated. In this simulation, a Gaussian window [112], $g(t) = \frac{1}{\sqrt{\pi f_b}} e^{-\frac{t^2}{f_b}}$, with bandwidth parameter $f_b = 2$ Hz^{-2} and duration of 5 ms and 80 ms were examined on the composite signal. The spectrogram in figure 4.3a illustrates that for the narrower window the time resolution is better than that of frequency. The figure shows clearly the frequency jump at the time $t = 0.2$ s, but there is no such sharp resolution for the frequency components in the frequency domain. By increasing the size of window to the 80 ms, the frequency resolution is improved in the cost of deterioration of the time resolution, as shown in figure 4.3b.

4.3.3 Extraction of Temporal Values by STFT

STFT with its time-frequency localisation features can be deployed for the extraction of temporal values of time varying signals such as chirp form signals. This approach has been reported for the impedance spectroscopy using a chirp [113].

To examine the STFT method an algorithm was performed with a FFT routine available in MATLAB[39]. In this implementation, the Gaussian window, as described in the previous section, was exploited. To have accurate extraction, the window bandwidth must be small such that $\Delta\omega \leq \phi'(t)$, where $\phi'(t)$ denotes the instantaneous frequency of the signal [108, 114]. To satisfy this, since the frequency of the chirp varies over time, the length of window is determined using the minimum frequency component in the chirp. Therefore, it can be proved that L satisfies following constraint:

$$L \geq \frac{1}{f_{min} T_s} \tag{4.8}$$

where f_{min} is the minimum frequency in the chirp and T_s is the sampling time.

The STFT algorithm was designed as following steps:

1. The appropriate window size, L, is selected such that it satisfies (4.8).

2. Using L and knowledge of the frequency variation of the excitation chirp, the signal is divided into the appropriate segments such that they contain the desired frequency points. These segments are then arranged as columns of the matrix $S = [s_1, \cdots, s_N]$, where N is the number of the discrete frequency points.

3. Each column of the matrix S is multiplied by the window.

4. The FFT is applied to each column of S.

5. The magnitude and phase of the elements of S are determined.

6. The maximum magnitude of each column and its corresponding phase are selected as the magnitude and phase at each frequency points.

To determine the spectral characteristics of a transfer function, for instance (4.1), the input excitation signal and the output signal must be separately analysed by the above procedure and then the magnitude and phase of Y are determined by:

$$|Y(j\omega)| = \frac{|I_{in}(j\omega)|}{|V_{out}(j\omega)|}, \qquad \angle Y(j\omega) = \angle I_{in}(j\omega) - \angle V_{out}(j\omega) \tag{4.9}$$

Frequency Analysis of RC Network

The performance of the above procedure was evaluated through the frequency analysis of a RC network. The advantage of using this is that it can be analytically analysed and compared with the simulation results. The schematic of the

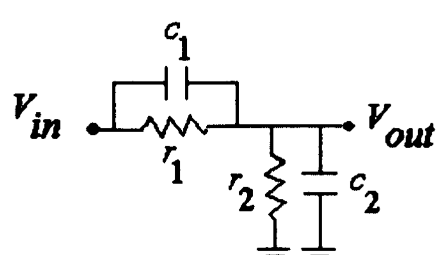

Figure 4.4: RC network circuit.

RC network is shown by figure 4.4. The transfer function of this network, $H(\omega)$, is:

$$H(\omega) = \frac{V_{out}}{V_{in}} = k\left(\frac{1 + i\omega/\omega_z}{1 + i\omega/\omega_p}\right) \tag{4.10}$$

where $k = \frac{r_2}{r_1+r_2}, \omega_z = \frac{1}{r_1 c_1}$ and $\omega_p = \frac{r_1+r_2}{(c_1+c_2)(r_1 r_2)}$. By substituting suitable component values, a low-pass or high-pass circuit can be simulated. This network was simulated by solving its differential equation numerically. The magnitude and phase of transfer function (4.10) at various frequency points were then determined using the algorithm presented above. The input signal was a linear chirp with amplitude 1 V that sweeps linearly over the frequency range from 10 kHz to 510 kHz within 5ms. It was applied to a low-pass network as defined in table 4.1. The table illustrates the numerical results and also analytical values for the network at the discrete frequency points. As a measure of accuracy, relative errors were calculated for the analytical and simulated values. This can be expressed by:

$$E = \frac{|V_S - V_A|}{|V_A|} \tag{4.11}$$

where V_A is the analytical value and V_S is the simulated value. The simulations

Table 4.1: Comparison of simulated and analytical solution for the low-pass network with component values: $r_1 = 1\text{M}\Omega$, $r_2 = 1\text{M}\Omega$, $c_1 = 1\text{pF}$ and $c_2 = 20\text{pF}$, and when the input signal was linear chirp.

Frequency	Magnitude			Phase(D)			Relative Error(%)	
(kHz)	Analytical	L=0.1ms	L=0.5ms	Analytical	L=0.1ms	L=0.5ms	Magnitude	Phase
20	0.3044	0.3177	0.3164	45.68	47.93	55.08	4.38	4.91
30	0.2295	0.2354	0.3130	52.52	54.65	10.10	2.61	4.05
50	0.1520	0.1535	0.2151	55.69	57.57	20.38	0.93	3.37
150	0.0691	0.0686	.0732	40.92	42.18	49.81	0.69	3.06
250	0.0564	0.0567	0.0570	29.01	28.46	25.88	0.60	1.90
500	0.0499	0.0499	0.0500	15.92	15.96	15.96	0.08	0.26

were repeated for the various window sizes. The simulation results have indicated that the accuracy of the magnitudes have closely the corresponding levels, but there is significant discrepancy in most detected phase values. For instance, the table shows the results at two window sizes of 0.1ms and 0.5ms. The relative errors in the table 4.1 were calculated for the narrower window.

The above simulation was also conducted using a logarithmic chirp described in section 3.4.5, as input excitation, for a similar Network to that described above. The simulations were also repeated for the various window sizes. The simulations resulted in similar variations as that of linear chirp. Table 4.2 shows the results for the window size of 0.1ms and 0.5ms at different frequency.

Table 4.2: Comparison of simulated and analytical solution for the low-pass network when the input signal was logarithmic chirp.

Frequency	Magnitude			Phase(D)			Relative Error(%)	
(kHz)	Analytical	L=0.1ms	L=0.5ms	Analytical	L=0.1ms	L=0.5ms	Magnitude	Phase
20	0.3044	0.3004	0.3208	45.68	45.42	46.42	1.30	0.58
30	0.2295	0.2343	0.2432	52.52	52.68	51.27	2.11	0.30
50	0.152	0.1541	0.1590	55.69	55.34	55.22	1.37	0.65
150	0.0691	0.0680	0.0743	40.92	41.97	20.43	1.49	2.55
250	0.0564	0.0562	0.0592	29.01	28.85	32.30	0.29	0.54
500	0.0499	0.0501	0.0510	15.92	15.95	18.39	0.36	0.19

4.4 Continuous Wavelet Transform

4.4.1 CWT

CWT of a signal $S(t)$ using wavelet $\psi(t)$ is defined by [108, 115]:

$$CWT_s = \int_{-\infty}^{+\infty} S(t)\psi^{\star}_{a,b}(t)dt \tag{4.12}$$

where, a and b are scale and translation parameters, respectively, and $\star$ denotes complex conjugation. Wavelet $\psi(t)$ is called the mother wavelet and is a function with zero average and finite energy. The scaled and translation form of the

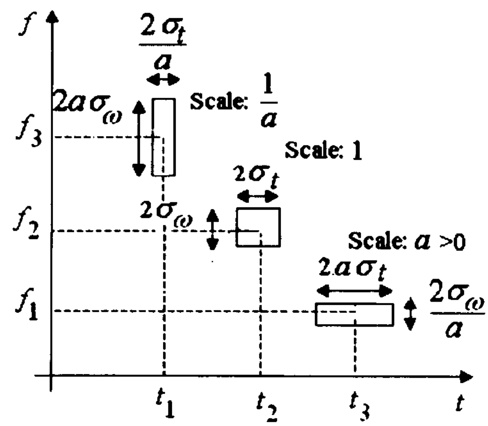

Figure 4.5: Time-frequency resolution of CWT.

mother wavelet, $\psi_{a,b}(t)$, is given by:

$$\psi_{a,b}(t) = \frac{1}{\sqrt{a}}\psi(\frac{t-b}{a}) \tag{4.13}$$

By scaling the mother wavelet, time resolution can be exchanged for frequency resolution, and vice versa, hence providing variable time-frequency resolution for the WT. This makes the wavelet transform an efficient tool to analyse time-varying signals.

In the WT, in contrast to the STFT, the width and the height of the window are modified such that they can match to the specific frequency component. Thus the time and frequency resolution are also modified. This scaling capability overcomes the drawback of the fixed window in the STFT. The product of time and frequency resolution is independent from scale and translation parameters. This is illustrated in figure 4.5.

By using (4.3) and (4.5), the time resolution $\sigma_{t,a}$ and frequency resolution $\sigma_{\omega,a}$ of the scaled wavelet (4.13), are given by:

$$\sigma_{t,a} = a\sigma_t \tag{4.14}$$

$$\sigma_{\omega,a} = \frac{\sigma_\omega}{a} \tag{4.15}$$

4.4.2 Extraction of Temporal Values using CWT Ridge

The energy density of a signal can be represented by the square of the modulus of the CWT (or *scalogram*). The distribution of energy shows its concentration around a particular curve which is called the ridge of the CWT. This phenomenon is illustrated in figure 4.6. The figure shows the ridge of the CWT of the sinusoidal signal described in section 4.3.2. This indicates that the scalogram has

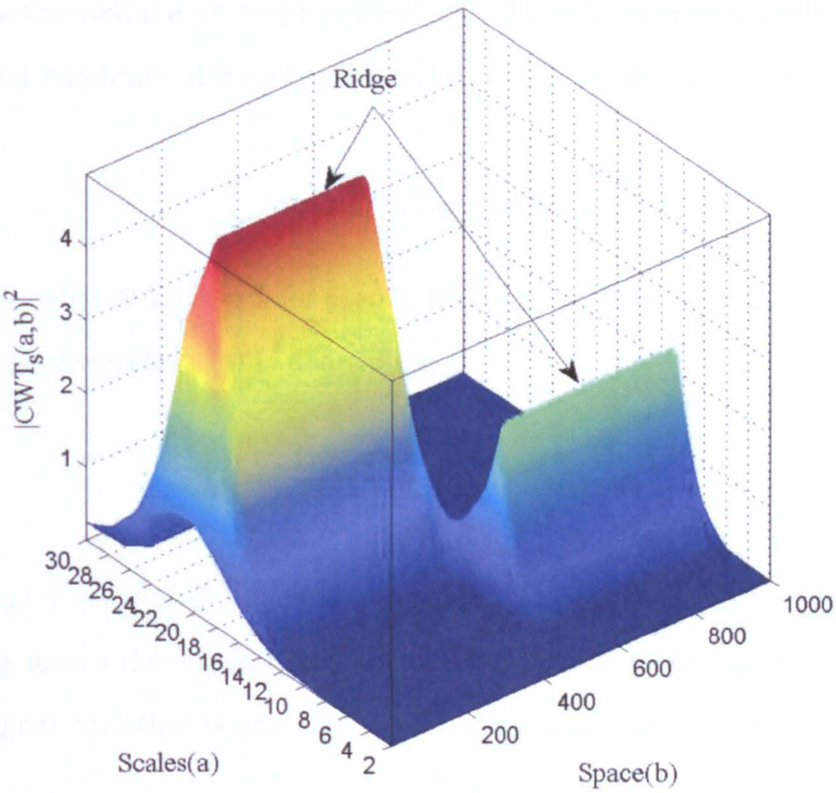

Figure 4.6: Ridge of CWT of sinusoidal signal consisting of 500 kHz and 1 kHz frequency components, $|CWT_s(a,b)|^2$.

local maximum values for the frequency components of the signal in each instant of time.

As described later in this chapter, extraction of the ridge reveals information regarding the instantaneous frequency of the signal and also its temporal values[116]. Delprat [116] proposed an algorithm for the ridge extraction using a Gaussian function as the analysing wavelet. Mallat [108] also achieves the same results by using an analytic wavelet transform.

The properties of the CWT ridge are exploited for the accurate extraction of necessary values from the chirp signal. For this, the method presented in [108] is deployed. This method is briefly described as follows.

An analytic wavelet $\psi(t)$ can be constructed using frequency modulation of window $g(t)$:

$$\psi(t) = g(t)e^{j\omega_c t} \tag{4.16}$$

where ω_c is the modulation frequency and $g(t)$ is a real symmetric and normalised window and bandlimited with bandwidth $\Delta\omega$. The Fourier transform of $\psi(t)$ is:

$$\Psi(\omega) = G(\omega - \omega_c) \tag{4.17}$$

It is obvious that $\Psi(\omega) << 1$ for $\omega < 0$, if $G(\omega) << 1$ for $\omega_c > \Delta\omega$. The scaled and translated wavelet $\psi(t)$ is defined by:

$$\psi_{a,b} = \frac{1}{\sqrt{a}}\psi(\frac{t-b}{a}) = e^{-i\kappa b}g_{a,b,\kappa}(t) \tag{4.18}$$

where $g_{a,b,\kappa}(t) = \sqrt{a}g(\frac{t-b}{a})e^{i\kappa t}$ with $\kappa = \omega_c/a$. Equation (4.18) also shows that the scaling moves the centre frequency of $\psi(t)$ from ω_c to $\kappa = \omega_c/a$.

The signal $S(t)$ that is analysed is real and defined as:

$$S(t) = A(t)\cos\phi(t) \tag{4.19}$$

where $A(t)$ and $\phi(t)$ are amplitude and phase, respectively. The instantaneous frequency of this signal, $\phi'(t)$ of $S(t)$ is given by:

$$\phi'(t) = \frac{d\phi(t)}{dt} \tag{4.20}$$

In [108], it is proved that the wavelet transform of signal $S(t)$ using the analytic wavelet $\psi(t)$, described by (4.16), can be expressed by:

$$CWT_S(a,b) =< S, \psi_{a,b} >= \frac{\sqrt{a}}{2}A(b)e^{i\phi(b)}(G(a[\kappa - \phi'(b)]) + \epsilon(b,\kappa)) \tag{4.21}$$

The corrective term $\epsilon(b,\kappa)$ can be ignored by satisfying the following conditions:

$$\frac{\omega_c^2}{|\phi'(b)|}\,\frac{|A''(b)|}{|A(b)|} << 1 \tag{4.22}$$

$$\omega_c^2\,\frac{\psi''(b)}{|\psi'(b)|^2} << 1 \tag{4.23}$$

$$\phi'(b) \geq \frac{\Delta\omega}{a} \tag{4.24}$$

The above equations express that to ignore $\epsilon(b,\kappa)$ in (4.21), the variation of $A(t)$ and $\phi'(t)$ over the wavelet $\psi_{a,b}$ must be slow, and also the bandwidth of the scaled wavelet , $\Delta\omega/a$, must be smaller than $\phi'(b)$. By neglecting $\epsilon(b,\kappa)$, the ridge of the CWT is calculated by maximisation of (4.21). This expression is at its maximum when:

$$\phi'(b) = \kappa(b) = \frac{\omega_c}{a(b)} \tag{4.25}$$

This means that at the ridge, the centre frequency of the scaled wavelet gives the instantaneous frequency of the signal. On the ridge, therefore, by substituting (4.25) into (4.21), the temporal amplitude $A(b)$ of the signal is determined by:

$$A(b) = \frac{2\,|CWT_S(a_r(b),b)|}{\sqrt{a_r(b)}\,|G(0)|} \tag{4.26}$$

where a_r denotes the scale on the ridge. The phase of signal is also equal to the phase of wavelet transform on the ridge:

$$\phi(b) = \angle CWT_S(a_r(b),b) \tag{4.27}$$

Equations (4.26) and (4.27) result in analytic values of the real signal $S(t)$. The presented theory implies that it is possible to build an algorithm to determine an accurate estimation of the temporal characteristics of the signal, provided that the stated conditions are satisfied.

4.4.3 Complex Morlet Wavelet

The use of a complex form of the wavelet, as mentioned in the previous section, allows the estimation of the temporal specifications separately. The complex wavelet can be constructed using various real windows, for instance, Gaussian, Hamming and Hanning windows [108]. In this research, the complex Morlet wavelet was utilised as the mother wavelet $\psi(t)$. The reason for this selection is that this wavelet is essentially constructed by modulation of a Gaussian window, which is able to provide maximum localization in time and frequency plane. It is shown later in this section that the Morlet wavelet retains the time and frequency resolution equal to that of Gaussian window. A normalised form of the complex Morlet wavelet is expressed by [117, 118]:

$$\psi(t) = \frac{1}{\sqrt{\pi f_b}}(e^{i\omega_c t} - e^{-f_b \omega_c^2/4})e^{-t^2/f_b} \tag{4.28}$$

where $\omega_c = 2\pi f_c$, f_c is centre frequency and f_b is bandwidth parameter. The Fourier transform of Morlet wavelet is:

$$\Psi(\omega) = e^{-\frac{f_b}{4}(\omega-\omega_c)^2} - e^{-\frac{f_b}{4}(\omega^2+\omega_c^2)} \tag{4.29}$$

Using (4.3) and (4.5), the time and frequency resolution of Morlet wavelet, σ_ω and σ_t, can be obtained by:

$$\sigma_\omega = \frac{1}{\sqrt{f_b}} \tag{4.30}$$

$$\sigma_t = \frac{\sqrt{f_b}}{2} \tag{4.31}$$

It is obvious that the multiplication of (4.30) and (4.31) retains the equality in equation (4.7), verifying that the Morlet wavelet provides the ultimate possible time-frequency localisation. An example of the time and frequency domain waveforms of the Morlet wavelet for two sets of scale and translation values is shown in figure 4.7. This figure also demonstrates that the time support of the wavelet

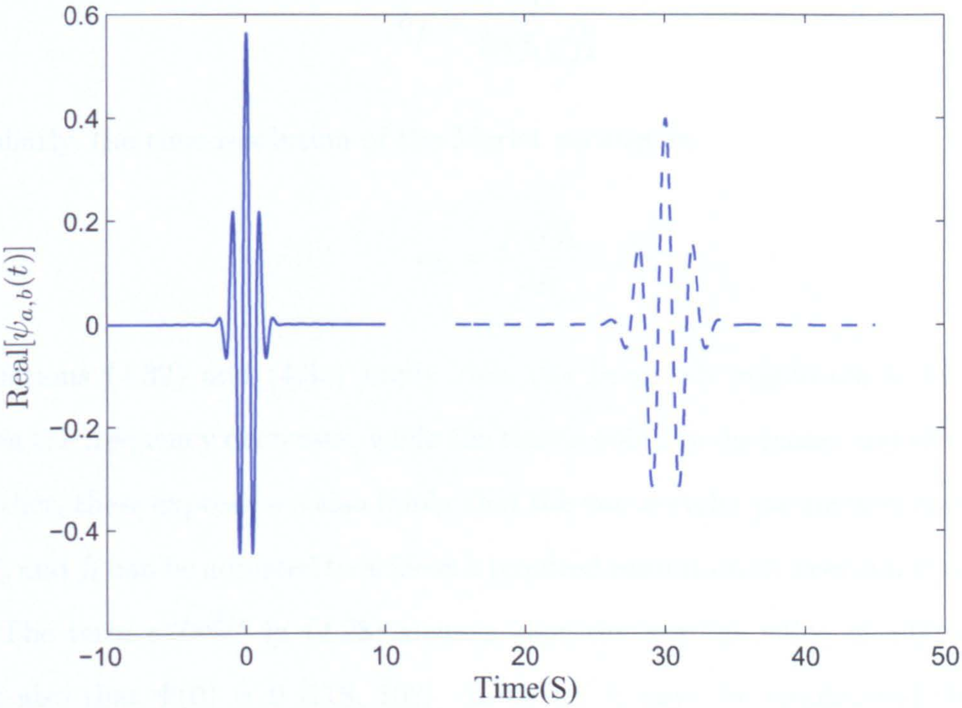

(a)

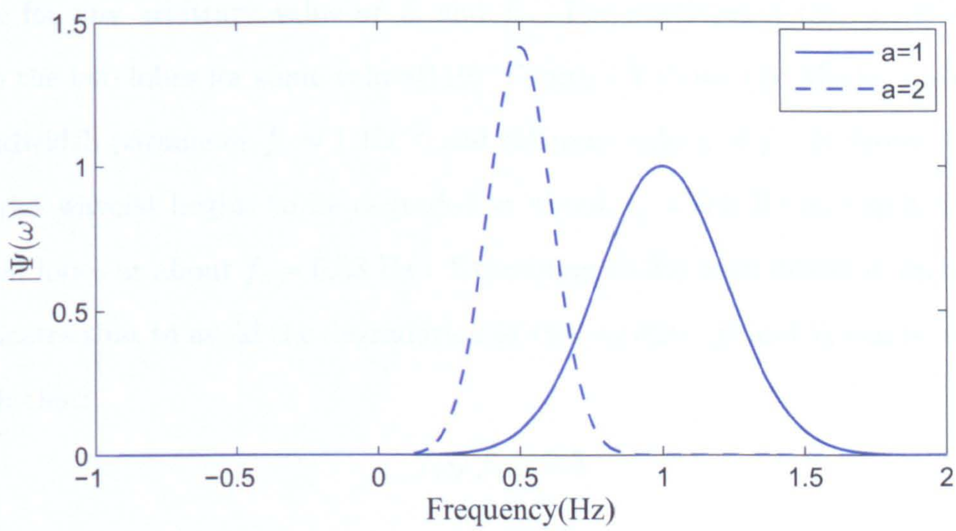

(b)

Figure 4.7: Scaled and translated Morlet wavelet, $f_c = 1$ Hz and $f_b = 1$ Hz^{-2}: real part of $\psi_{a,b}(t)$ (a)and magnitude of Fourier transform $|\Psi(\omega)|$ (b).

increases in direct proportion to the scale parameter a, but in the frequency domain it is focused on frequency $f = f_c/a$ with bandwidth inversely proportional to scale. Using expressions (4.15), (4.30) and the relation $\sigma_f = \sigma_\omega/2\pi$, the frequency resolution at frequency f_i can be calculated by:

$$\sigma_{f_i} = \frac{f_i}{2\pi f_c \sqrt{f_b}} \tag{4.32}$$

Similarly, the time resolution of the Morlet wavelet is:

$$\sigma_{t_i} = \frac{f_c \sqrt{f_b}}{2 f_i} \tag{4.33}$$

Equations (4.32) and (4.33) imply that the frequency resolution is increased when the frequency decreases, while the time resolution decreases and vice versa. Further, these expressions also imply that the two wavelet parameters consisting of f_c and f_b can be adjusted to achieve a required resolution at a certain frequency.

The term $e^{-f_b \omega_c^2/4}$ in (4.28) ensures that the average value of $\psi(t)$ is zero and also that $\Psi(0) = 0$ [118, 108]. However, it must be emphasised that the envelope $|\psi(t)|$ of the Morlet wavelet, given by (4.28), does not retain its single lobe for any arbitrary value of f_c and f_b. The envelope of this wavelet splits into the two lobes for some values[119]. Figure 4.8 shows the Morlet wavelet for bandwidth parameter $f_b = 1$ Hz^{-2} and different values of f_c. It shows that the Morlet wavelet begins to be degraded at about $f_c = 0.5$ Hz and split into two equal lobes at about $f_c = 0.38$ Hz . Examining (4.28) with different values of f_b indicates that to avoid the degradation of this wavelet, f_c and f_b can be selected such that:

$$f_c \sqrt{f_b} \geq 0.5 \tag{4.34}$$

It can be verified that the degrading wavelet (4.28) is related to the corrective term. This term can be eliminated by appropriate selection of f_b and f_c. However, as explained in the next section, this results in a smaller range for selection of the wavelet parameters.

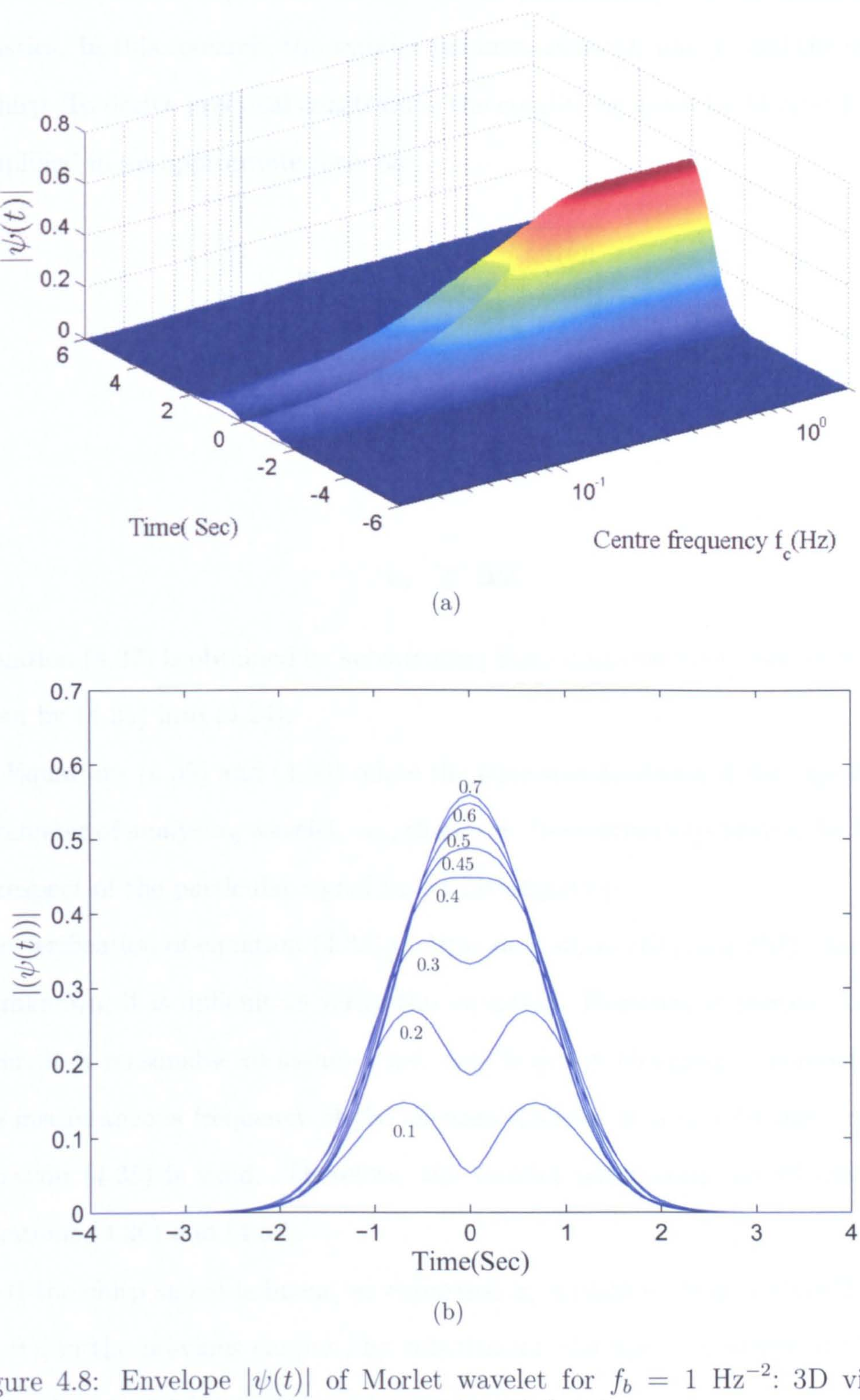

Figure 4.8: Envelope $|\psi(t)|$ of Morlet wavelet for $f_b = 1$ Hz^{-2}: 3D view for $0 \leq f_c \leq 2$ Hz (a), 2D profile at some value of f_c (b).

4.4.4 Selection of Wavelet Parameters

In section 4.4.2 it was mentioned that the temporal values can be determined on the ridge of the scalogram if some restrictions are satisfied. The satisfaction of these conditions is dependent on the wavelet parameters, and the signal characteristics. In this research, the wavelet parameters are f_c and f_b and the signal is a chirp. To derive practical constraints, the conditions given by (4.22)-(4.24) are simplified in an appropriate form as:

$$\omega_c << |\phi'(b)| \sqrt{\frac{|A(b)|}{|A''(b)|}} \tag{4.35}$$

$$\omega_c << \frac{|\phi'(b)|}{\sqrt{\phi''(b)}} \tag{4.36}$$

$$\omega_c \geq \Delta\omega \tag{4.37}$$

Equation (4.37) is obtained by substituting instantaneous frequency on the ridge given by (4.25) into (4.24).

Equations (4.35) and (4.36) relate the time specifications of the signal to the parameter of analysing wavelet, ω_c, therefore, the restrictions have to be fulfilled in respect of the particular signal under investigation.

The verification of equation (4.35) is dependent upon $A(t)$ and $\phi'(t)$. Since $A(t)$ is unknown, it is difficult to verify this equation. However, in process measurement, it is reasonable to assume that $A(t)$ is slowly changing in comparison to the instantaneous frequency of the excitation signal at a certain time and thus equation (4.35) is valid. Therefore, the wavelet parameters are selected using equations (4.36) and (4.37).

If the chirp signal is linear, as expressed by equation $S(t) = A\cos[2\pi(f_0 t + \frac{1}{2}\beta\ t^2)]$ in the previous chapter, by substituting the first and second derivatives of its phase, equation (4.36) can be rewritten as:

$$f_c \ll \frac{f_i}{\sqrt{2\pi\beta}} \tag{4.38}$$

where f_i denotes instantaneous frequency of linear chirp.

In (4.37) the bandwidth of the analysing wavelet can be replaced by $\frac{2}{\sqrt{f_b}}$, and thus it can be rewritten as:

$$f_c \geq \frac{1}{\pi\sqrt{f_b}} \tag{4.39}$$

Connection of equations (4.38) and (4.39) gives the appropriate range for f_c:

$$\frac{1}{\pi\sqrt{f_b}} \leq f_c \ll \frac{f_i}{\sqrt{2\pi\beta}} \tag{4.40}$$

Therefore, for a linear chirp the parameters f_c and f_b must be adjusted such that the equation (4.40) is fulfilled. These parameters are also linked to the time duration, σ_{t_i},and frequency bandwidth, σ_{f_i} of the analysing wavelet, Morlet wavelet, at a particular frequency given by (4.33) and (4.32), respectively. That is, the condition (4.40) can also be fulfilled by adjusting $f_c\sqrt{f_b}$. Hence, by rearranging the inequality (4.40) and incorporating the condition (4.34), it can be proved that:

$$0.5 \leq f_c\sqrt{f_b} \ll f_i\sqrt{\frac{f_b}{2\pi\beta}} \tag{4.41}$$

This form also implies the relation with time and frequency resolution, σ_{t_i} and σ_{f_i}.

An example of the use of this expression is shown in figure 4.9 for two chirp signals sweeping the bandwidth of 500 kHz with two different rates and also $f_b = 1$ Hz^{-2}. The arrows in the figure present the regions for the selection of the appropriate parameters. This figure demonstrates that, in general, the slower chirp signal provides more freedom for choosing the appropriate parameters especially in lower frequencies. The region for the selection is also different for each chirp. This region is wider for the chirp with rate β_2, while this becomes smaller for the faster one, β_1. In addition, for each chirp the area in the lower frequency is more limited while it becomes wider at higher frequency. Thus, in general, there is less flexibility at low frequencies for selection of the appropriate parameters.

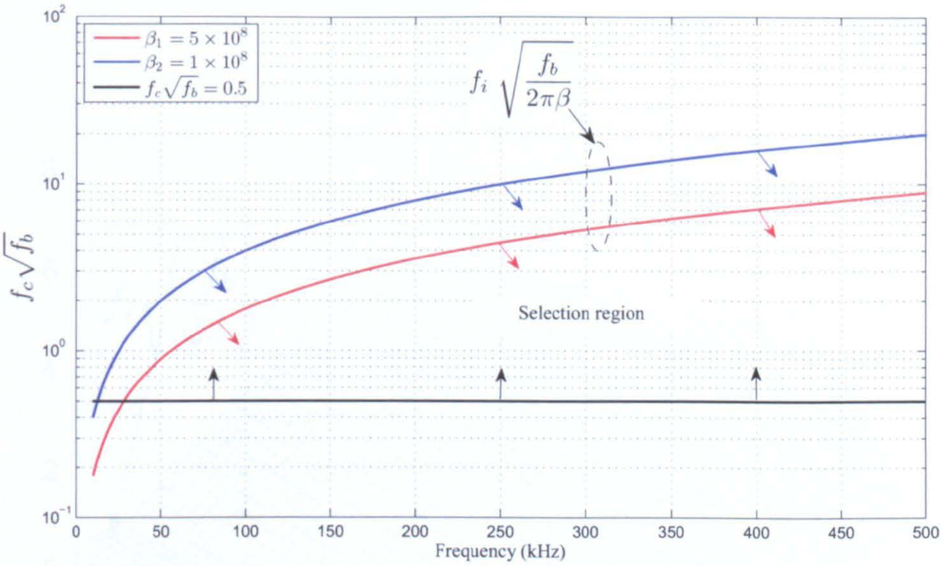

Figure 4.9: Selection region of wavelet parameters for two chirp signals with 500 kHz bandwidth at two different rates β_1 and β_2, left and right side of (4.41) are shown for $f_b = 1$ Hz^{-2}.

In addition, in equation (4.41), by modification of f_b, the permissible range for choosing the wavelet parameters is also modified accordingly. Thus, this increases the flexibility for choosing appropriate parameters.

For example, the behaviour of expression (4.41) at two frequencies consisting of 10 kHz and 500 kHz, versus f_c and f_b, are shown in figure 4.10. The comparison of figures 4.10a and b demonstrates that the appropriate range for the wavelet parameters varies over the frequency range.

In the above discussion the complete form of the Morlet wavelet given by (4.28), was considered. However, if the brief form of the Morlet wavelet is utilised, it is necessary to meet the condition: $f_b\omega_c^2/4 \gg 1$. This restriction can be taken into account by modification of equation (4.41). This is, however, a restrictive factor for selection of wavelet parameters. For this reason, it was preferred to exploit the complete form of the Morlet wavelet.

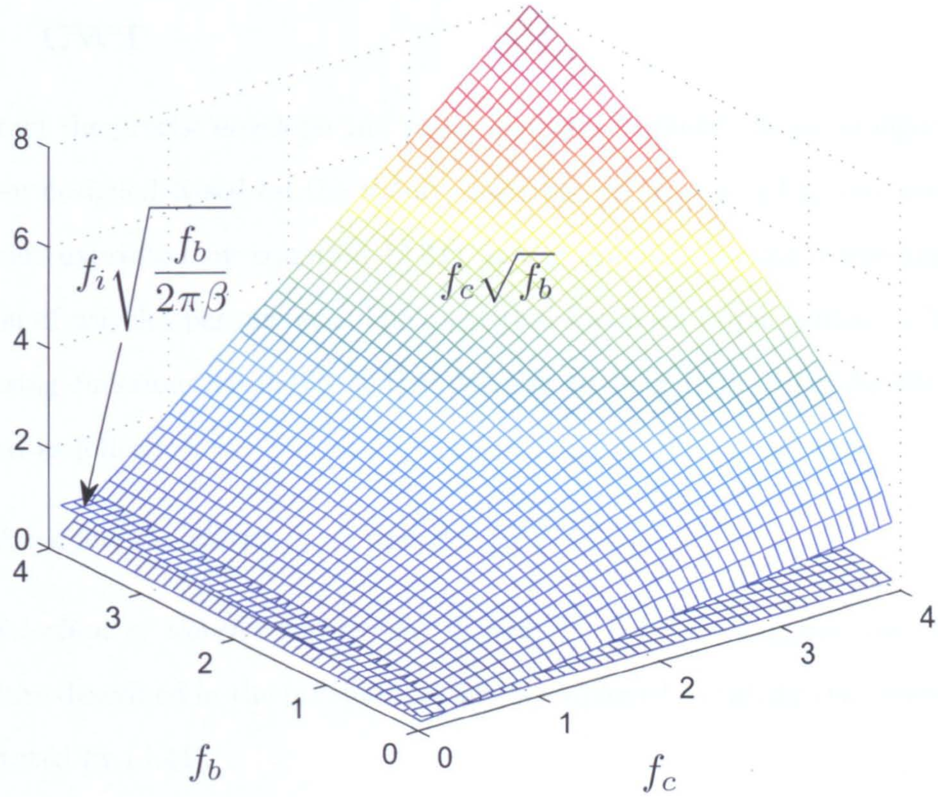

(a)

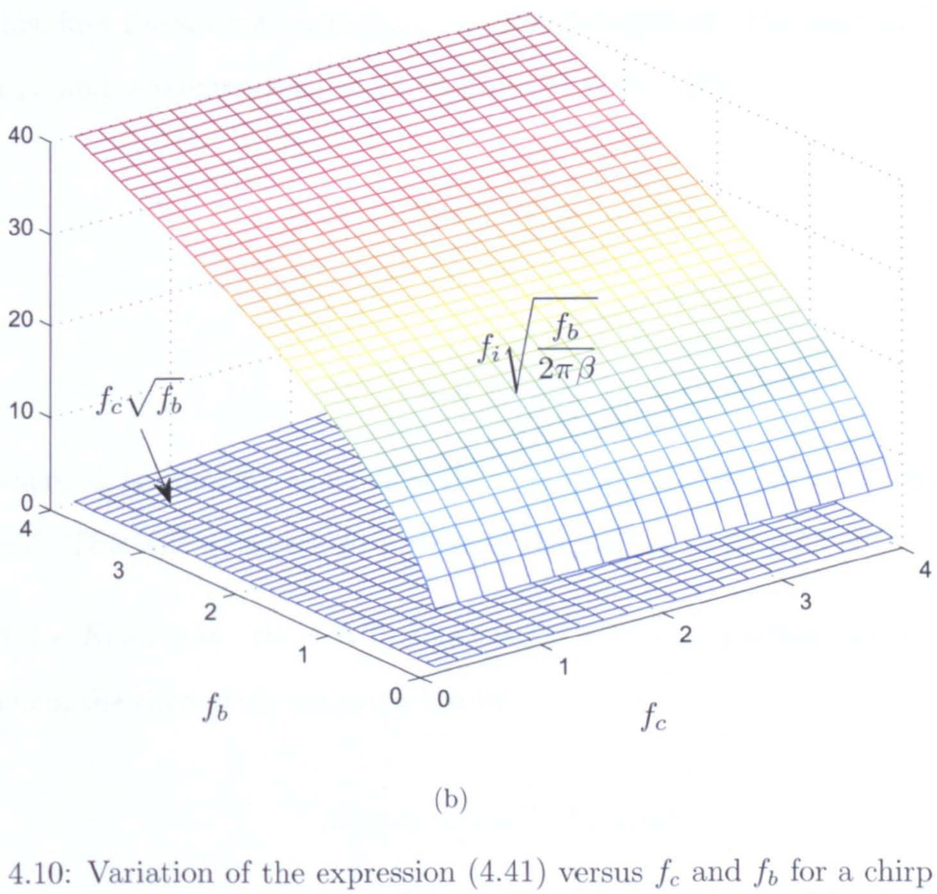

(b)

Figure 4.10: Variation of the expression (4.41) versus f_c and f_b for a chirp with 500 kHz bandwidth and $\beta = 1 \times 10^8$ at 10 kHz (a) and 500 kHz (b).

4.4.5 Extraction of Chirp Temporal Characteristics by CWT

To extract the precise envelope and phase over the frequency band an algorithm has been designed based on the theory described in section 4.4.2, and also the constraint expressed by equation (4.41) in the previous section regarding the selection of wavelet parameters. The algorithm has been implemented in MATLAB using functions available in the Wavelet toolbox[120]. The algorithm is designed as follows:

1. *Specifying the chirp:* f_0, f_f and β.

2. *Selection of wavelet parameters* f_c *and* f_b*:* For this purpose, the procedure described in the previous section is employed to satisfy the conditions stated by (4.41).

3. *Determination of the wavelet scaling grid:* the scaling grid must be determined appropriately according to the selected chirp characteristics. For this, first the scaling range $[a_{min} \quad a_{max}]$ is determined. The minimum scale a_{min} and maximum scale a_{max} are calculated by [120]:

$$a_{min} = \frac{f_c}{f_f T_s} \tag{4.42}$$

$$a_{max} = \frac{f_c}{f_0 T_s} \tag{4.43}$$

   where T_s is sampling time. It is then necessary to determine an adequate grid. This will be described further in the next section.

4. *Ridge Extraction:* the CWT is calculated over the specified scaling grid. Then, the ridge data are extracted by:

$$a_r(b) = \max_a |CWT_S(a, b)| \tag{4.44}$$

This expression is used to determine the scales that maximize the scalogram.

5. *Calculation of the envelope and phase:* the temporal amplitude and phase on the ridge are calculated using:

$$A_r(b) = \frac{2\,|CWT_S(a_r(b), b)|}{\sqrt{a_r(b)}\,|G(0)|} \tag{4.45}$$

$$\phi_r(b) = \angle CWT_S(a_r(b), b) \tag{4.46}$$

6. *Determination of the precise temporal values:* Performing the procedure illustrated results in an output with ripple components which disturb precise determination of temporal values. This ripple arises from calculating the CWT on the coarser grid. They change more rapidly than the temporal values. These ripples can be cancelled in a similar way to a denoising procedure by discrete wavelet transform. The basic principle of denoising is the decomposition of the signal into wavelet coefficients, followed by reconstruction using those coefficients that contain zero or lower noise components [121]. Thus, the estimated values in step 6 are decomposed into the corresponding wavelet coefficients by certain level. Since the ripples appear in the details coefficients, they can efficiently be removed by performing the reconstruction using only approximation coefficients. As verified latter in this section, this results in an accurate estimation of the temporal envelop and phase over frequency range. The level of the decomposition can be determined by performing a test simulation over a scaling grid on the selected chirp.

Scaling Grid

To determine the scaling grid, first the range of scaling is calculated according to the minimum and maximum frequency of the signal. One solution is to create an equally spaced grid within the range $[a_{min} \quad a_{max}]$, and using $a = \frac{f_c}{fT_s}$, where f is frequency. However, this does not give adequate grid for wide bandwidth. The reason for this is that the wide bandwidth results in a wide scaling range, thus, performing the CWT on the fine grid requires considerable computation time and memory. Using the above approach on a coarser grid results in coarse spectral data at high frequency and fine data at lower frequency. To avoid this; logarithmic grid can be exploited. Thus it can be proved that the scaling grid with N points on the above range can be defined by:

$$a_n = a_{min}(\frac{a_{max}}{a_{min}})^{n/N} \quad n = 0, 1, \cdots, N \tag{4.47}$$

The grid can be adjusted via N. Figure 4.11 shows an example of the two methods described . The top figure, using the first method, indicates coarse

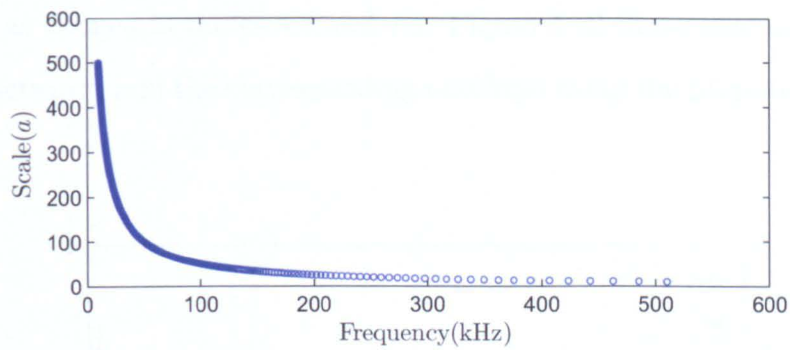

(a)

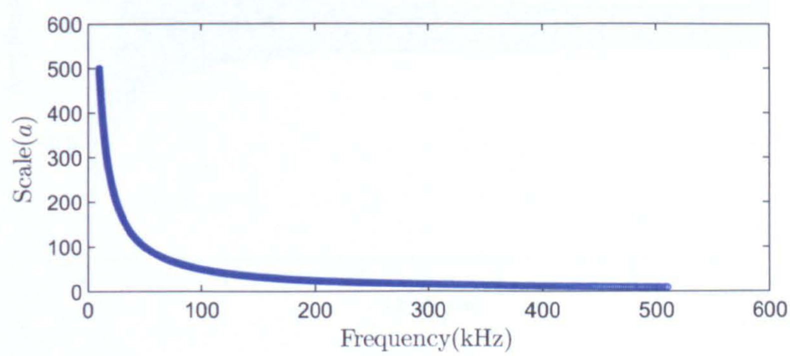

(b)

Figure 4.11: Scaling grid for a chirp sweeping from 10 kHz up to 510 kHz within duration $T = 0.005$ Sec, $f_s = 5 \times 10^6$ Hz and $f_c = 1$ Hz: using equally spaced grid (a), and logarithmic grid using (4.47) (b), where $N = 1000$.

grid at high frequency. In this grid, the difference between two consequative frequencies at the beginning of the frequency range is 9.8135 Hz, whereas this rises to 24.286 kHz at the end. The bottom figure shows the result of using the logarithmic method. Here, it was verified that the difference between two consequative frequencies at the beginning of the frequency range is 39.3957 Hz which rises to 2.0013 kHz at the end.

Frequency Analysis of RC Network

The performance of the described algorithm evaluated through the frequency analysis of RC network. The schematic diagram of the network and its transfer function were shown in pages 62 and 63, respectively. The frequency response of this network determined using the algorithm presented in this section. The input chirp signal, as in described in section 4.3.3, was applied to two low and high pass networks, as defined in tables 4.3 and 4.4. Figure 4.12 shows the response of the low pass network, and the corresponding envelope using the proposed algorithm.

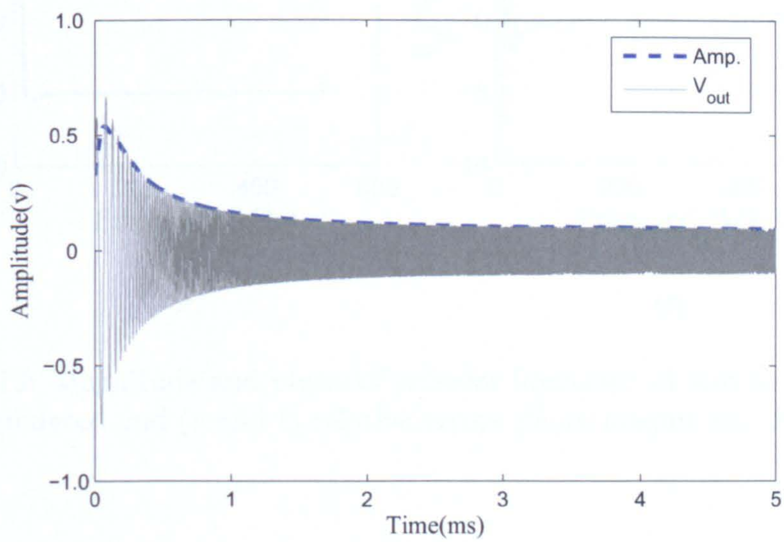

Figure 4.12: Output signal and extracted Magnitude.

Figure 4.13 also shows the analytical and simulated results for this network.

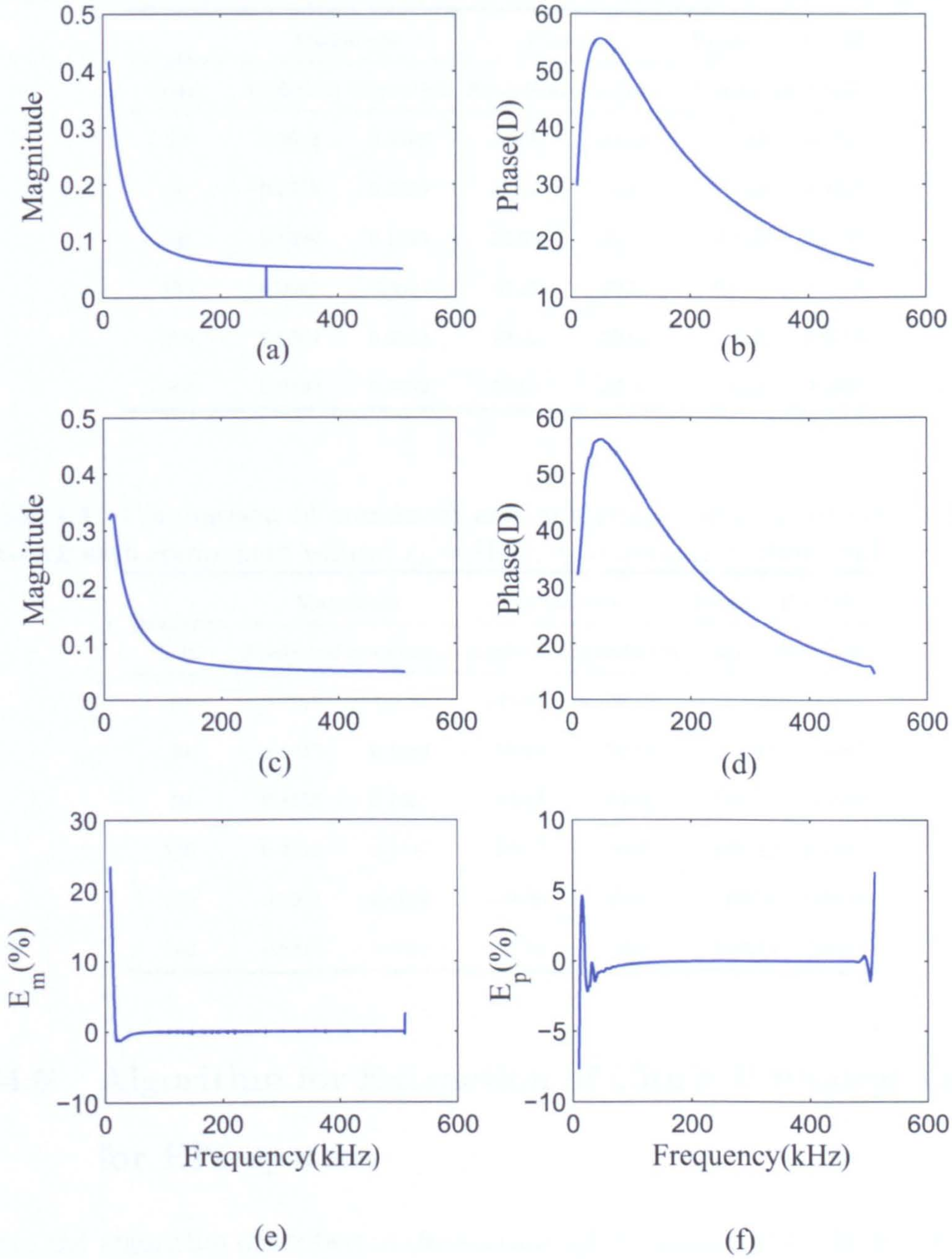

Figure 4.13: Magnitude and phase of transfer function: (a and b) analytical, (c and d) simulated and (e and f) relative errors (%)of magnitude, E_m, and phase E_p.

Tables 4.3 and 4.4 give comprehensive numerical results for the low and high pass RC networks, respectively.

They indicate the precise extraction of the amplitude and phase of the signal. In this example the maximum errors for the extraction of the amplitude and phase were less than 3% and 4%, respectively.

Table 4.3: Comparison of simulated and analytical solution for the low-pass network with component values: $r_1 = 1\text{M}\Omega$, $r_2 = 1\text{M}\Omega$, $c_1 = 1\text{pF}$ and $c_2 = 20\text{pF}$.

Frequency	Magnitude		Phase(D)		Relative Error(%)	
(kHz)	Analytical	Simulation	Analytical	Simulation	Magnitude	Phase
20	0.3044	0.3082	45.68	45.39	1.256	0.6234
30	0.2295	0.2319	52.52	53	1.046	0.9094
50	0.1520	0.1524	55.69	56.1	0.2364	0.7348
150	0.0691	0.0691	40.92	40.95	0.0111	0.0854
250	0.0564	0.0563	29.01	29.02	0.0114	0.0263
500	0.0499	0.0499	15.92	16.06	0.0020	0.885

Table 4.4: Comparison of simulated and analytical solution for the high-pass network with component values: $r_1 = 1\text{K}\Omega$, $r_2 = 50\Omega$, $c_1 = 10\text{nF}$ and $c_2 = 20\text{pF}$.

Frequency	Magnitude		Phase(D)		Relative Error(%)	
(kHz)	Analytical	Simulation	Analytical	Simulation	Magnitude	Phase
20	0.0763	0.782	-48.06	-46.15	2.456	3.977
30	0.1012	0.1014	-56.92	-56.55	0.2111	0.6495
50	0.1553	0.1551	-63.83	-63.96	0.0799	0.1919
150	0.4118	0.4117	-59.77	-59.8	0.0182	0.0457
250	0.6001	0.6002	-49.56	-49.57	0.00316	0.0244
500	0.8317	0.8317	-31.93	-32.2	0.0013	0.8123

4.4.6 Algorithm for Extraction of Chirp Temporal Values for EIT system

Since the algorithm described in the section 4.4.5 operates over the entire bandwidth. It will thus be time consuming in terms of processing when applied to multi-electrode impedance tomography. To avoid this problem a new algorithm has been designed which considers specified frequencies instead of the whole band. This exploits the linearity of the wavelet transform and the fact that the frequency rule of the chirp is known. Hence the wavelet parameters can be determined for a training waveform and are then applicable to the measured chirp waveforms. The algorithm thus has two parts. In the first part the optimal wavelet parameters are calculated for the desired frequencies, and are determined only once for a certain chirp and frequency set. In the second part these parameters are used to extract the temporal amplitude and phase of signal to be analysed.

The optimum wavelet parameters are determined through an error minimization procedure at a set of frequencies given by $F = [f_1, ..., f_n, ..., f_N]$. For this the procedure described in section 4.4.4 is employed to satisfy the conditions stated by (4.41). This leads to the calculation of a wavelet set: $W_p = [w_1, ..., w_n, ..., w_N]$ at frequencies $f_n \in F$. Each Morlet wavelet w_n is identified by two parameters f_b and f_c.

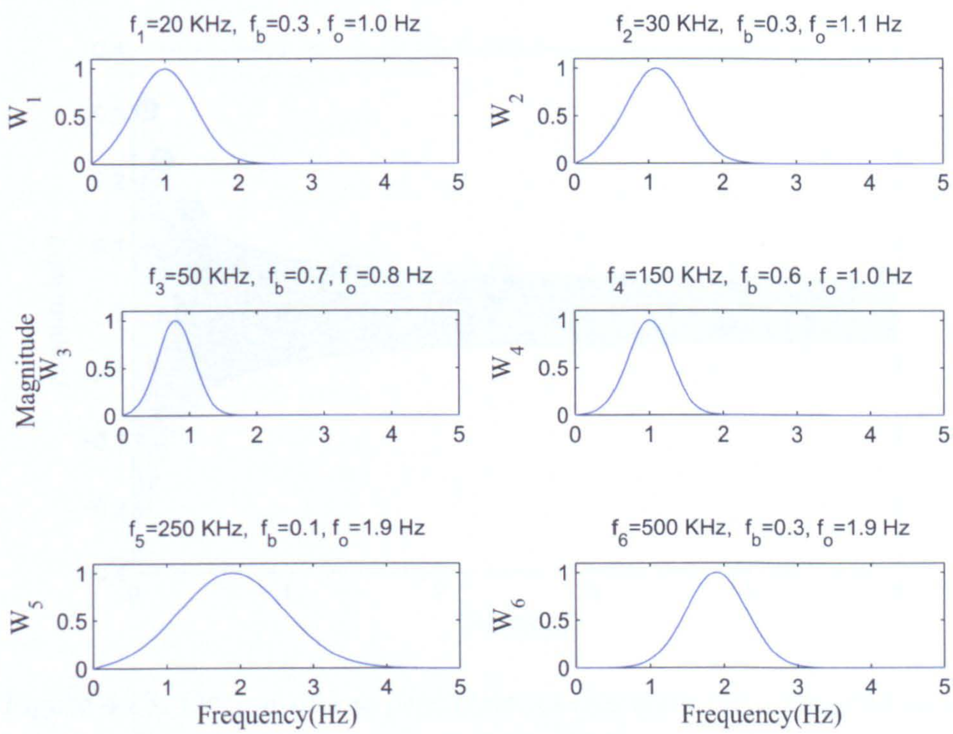

Figure 4.14: Fourier transform of selected wavelets for some frequencies.

For simulation, a linear chirp similar to that described in the previous section was exploited. The optimum wavelet parameters were then determined by the described procedure at certain frequencies. The frequencies were arbitrarily selected within the range 20 to 500 kHz. Figure 4.14 shows the Fourier transform of the resulting wavelets.

In the second part of the algorithm the chirp temporal characteristic is precisely computed by applying the algorithm at each frequency $f_n \in F$ using corresponding wavelet w_n. This is calculated using equations (4.26) and (4.27). For verification of the proposed method the output of the same low-pass filter described in section 4.3.3 was exploited here. The analytical and simulated temporal characteristic values are shown in figure 4.15 and table 4.5. As a measure of algorithm performance, the absolute values of relative error between analytical and simulated values indicate that the presented method can successfully extract the phase and amplitude of the signal.

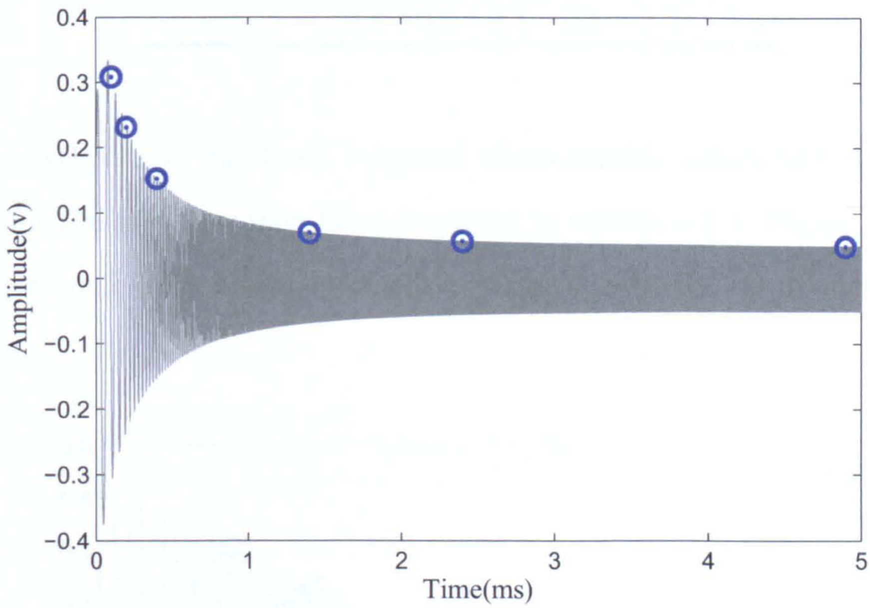

Figure 4.15: Output of low pass filter, circles show the extracted values.

The proposed algorithm in this section can be applied to any type of chirp signal. For example, the performance of the method was examined on a logarithmic chirp with the same parameters as the linear chirp described above. Since the frequency variation rule of chirp is logarithmic, the new set of optimum wavelet parameters were determined at the frequency points of interest. Table 5.1 gives the resulting wavelets parameters.

Table 4.5: Comparison of analytical and simulated results for linear chirp

Frequency (kHz)	Magnitude		Phase(D)		Relative Error(%)	
	Analytical	Simulation	Analytical	Simulation	Magnitude	Phase
20	0.3044	0.3131	45.68	45.96	2.8600	0.6100
30	0.2295	0.2320	52.52	53.01	1.1000	0.9300
50	0.1520	0.1523	55.69	55.97	0.2000	0.5000
150	0.0691	0.0691	40.92	40.94	0.0000	0.1000
250	0.0564	0.0563	29.01	29.01	0.1800	0.0030
500	0.0499	0.0499	15.92	15.90	0.0200	0.1300

Table 4.6: Wavelet parameters for logarithmic chirp swept from 10-510 kHz within 5ms.

Wavelet parameters	Frequency(kHz)					
	20	30	50	150	250	500
f_c	0.9	1	1	1.1	0.6	1.9
f_b	0.5	0.5	0.4	0.5	1.2	0.4

The analytical and simulated temporal characteristic values were then determined for the same low-pass filter described in section 4.3.3. Figure 4.16 shows the logarithmic chirp and the extracted magnitudes at the six frequency points.

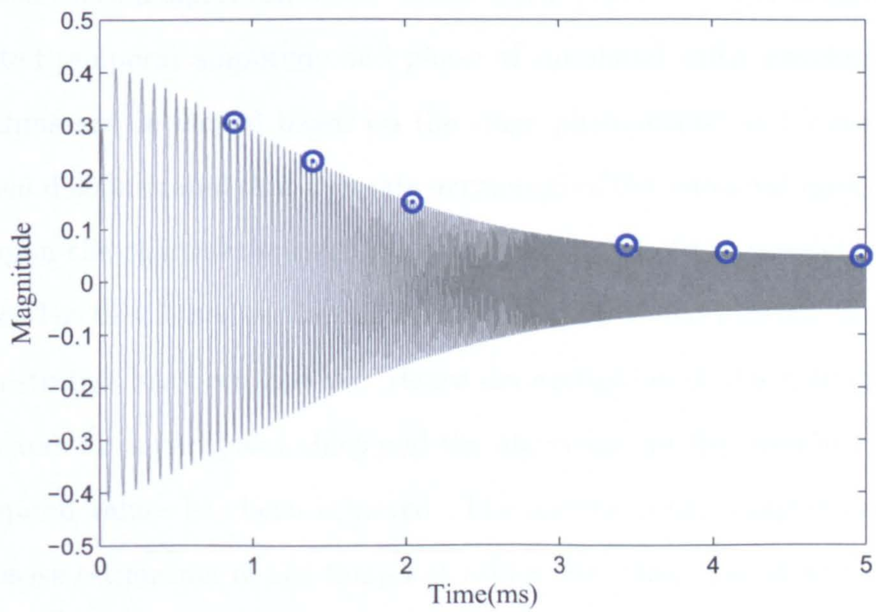

Figure 4.16: Output of low pass filter, circles show the extracted values.

Table 4.7 demonstrates analytical and simulated results, and also the absolute value of their relative difference. It can be seen that the presented method provides good estimation of temporal values on the logarithmic chirp.

Table 4.7: Comparison of simulated and analytical results for logarithmic chirp.

Frequency (kHz)	Magnitude		Phase(D)		Relative Error(%)	
	Analytical	Simulation	Analytical	Simulation	Magnitude	Phase
20	0.3044	0.3052	45.68	45.75	0.2809	0.1454
30	0.2295	0.2299	52.52	52.64	0.2065	0.2203
50	0.1520	0.1522	55.69	55.77	0.0840	0.1377
150	0.0691	0.0691	40.92	40.95	0.0339	0.0655
250	0.0564	0.0563	29.01	29.01	0.0352	0.0184
500	0.0499	0.0500	15.92	15.91	0.0239	0.0894

4.5 Conclusion

This chapter has demonstrated the algorithms developed to determine the required values from the chirp signal, in order to perform image reconstruction. For this purpose, STFT and CWT were examined. The simulation results have indicated that an algorithm based on the CWT provides better accuracy for the extracted temporal amplitude and phase of simulated chirp waveforms. These algorithms are developed based on the ridge phenomenon and using CWT. It has been demonstrated that accurate extraction of the temporal values is dependent upon the characteristics of the chirp signal and of the wavelet parameters utilised. For this, based on the conditions stated by Mallat in [108], the appropriate constraints has been derived. Hence determination of the optimum wavelet parameters for a particular chirp and the algorithm for the accurate estimation of temporal values has been achieved. The results in this chapter demonstrate the precise estimation of the temporal values, but they also show that there is an absolute relative error between analytical and estimated values.

Chapter 5

WEIT Simulation Study

5.1 Summary

This chapter addresses the augmentation of a single frequency EIT to form a wideband EIT system in order to provide spectral information. To achieve this requires a fast and efficient method to obtain the sensed data. For this purpose a novel method using chirp excitation is proposed and implemented. In this chapter, description of the proposed method is given and its verification is demonstrated. Firstly, a brief introduction gives the requirements of EIT systems and the essential underlying concepts. The performance of the method has been assessed through various simulations. The chapter finally describes methods for the analysis of the spectral tomographic data.

5.2 The Concept of Spectro-Tomography

The conventional requirement in EIT is to create a sequence of images of the process conductivity distribution using peripheral measurements, such that the data is obtained within a time scale that can track the process dynamics. The image set then provides an estimate of the evolving distribution of component materials within the process. In general these investigations reveal qualitative data which, with suitable calibration, may be analysed to offer relative quantitative measurement. However, the information usually is not enough either for the interpretation of process events, or for material identification. These drawbacks limit the application of single-frequency EIT systems.

A further requirement in many processes is the identification of materials, often from a known set of primary materials, or reagents, that may be loaded into a process vessel; and secondary materials, or products, that may be created through a physical and/or chemical reaction. The former requirement may be realised through single-frequency EIT but this typically cannot provide data to achieve the second requirement of material identification. In all cases additional data may be used to enhance a spatial distribution estimate. As introduced in Section 1.2 as a key motivation for this study, it appears feasible that this latter requirement can be accomplished using multi-frequency EIT. The underlying opportunity for this study is that process materials exhibit considerable change in their electrical properties in response to an injected signal over a frequency range arising from the properties of the material(s) of interest.

There is supporting evidence for example in medical research, for the characterisation of human tissue, and also for the diagnosis of particular clinical conditions based upon electrical properties [12, 11, 122, 89]. Empirical mathematical models of materials also indicate this behaviour [58].

Hence applying this concept promises to be useful in the investigation of an industrial process in which materials offer frequency dependent contrast. For instance pharmaceutical materials show various frequency-dependent behaviour over a frequency range[123]. For such a process, the construction of tomography images for a range of frequency bands can hence provide spectral data which would facilitate the interpretation of the process events; or the identification of materials which are an essential requirements in many processes. This is described further through a process where the initial materials A and B have frequency dependent behavior and the their composition results in product C which also exhibits different frequency dependent response, figure 5.1.

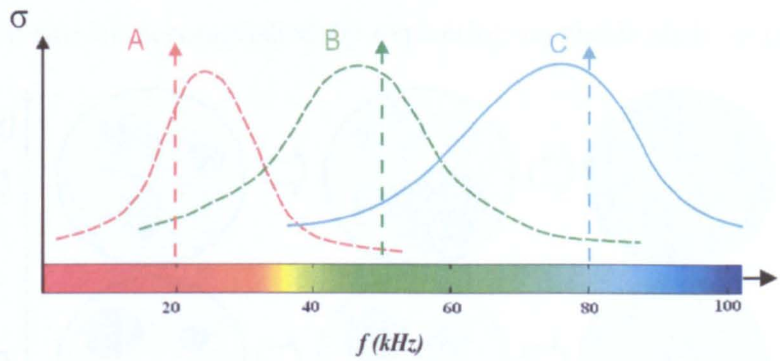

Figure 5.1: Example: spectral characteristics of initial materials A and B and product C.

Figure 5.2 shows this simple batch process, (top), and the conventional single-frequency EIT tomograph at 50 kHz, for example. Here the product C appears

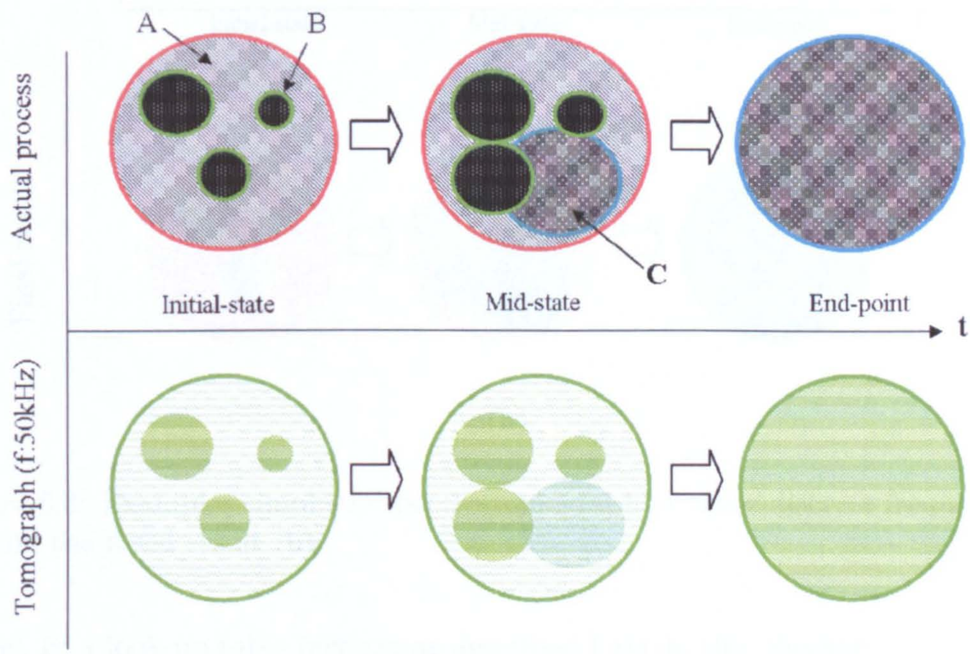

Figure 5.2: Example: batch process trajectory: actual process (top) and tomography images using single-frequency EIT at 50 kHz (bottom).

a different contrast value but in similar colour as the material B. Therefore this tomographic image can not provide information to assess the correct behaviour of the process. If the tomography images are reconstructed at various frequencies, they can provide local spectral conductivity, as illustrated in figure 5.3a. This spectral information may then be analysed or interpreted in order to either analysing the process events or material identification at various states. For instance, in this example the end product C may be identified, figure 5.3b.

The analyses can be accomplished by exploiting methods such as parametrised

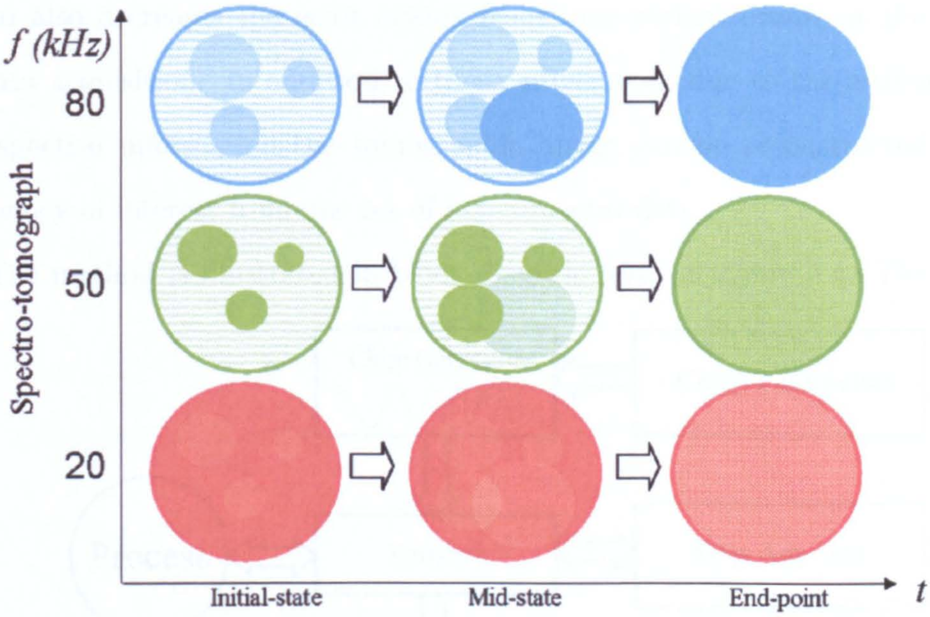

(a)

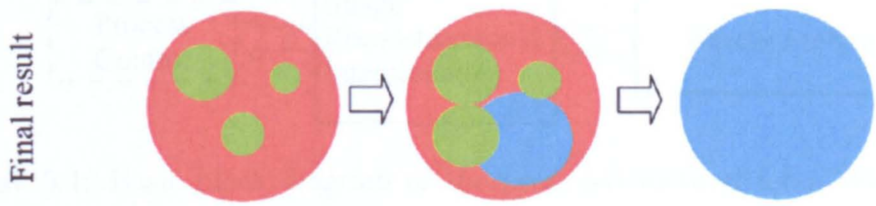

(b)

Figure 5.3: Example: simplistic spectro-tomograph at three discrete frequencies (a) and the fused result (b).

model, or a look-up table method as described later in this chapter.

5.3 Method

To meet dynamic process estimation needs the realisation of the WEIT method requires a fast and efficient procedure to obtain the sensed data. For this, a novel approach is proposed in which Chirp signal is used as excitation. As discussed in chapter 3, utilising Chirp excitation extends the conventional EIT system to provide spectral information and offers advantages of flexibility in speed, duration and frequency content of the peripheral process measurements. These capabilities enable high speed data acquisition that includes spectral information. This signal also decreases the error arising from time-variant events at the instant of data acquisition. In addition to these advantages, due to the availability of the spectral information the tomographic image can be reconstructed at any frequency of interest from one set of experimental data.

The method is illustrated in block diagram form in figure 5.4. The critical

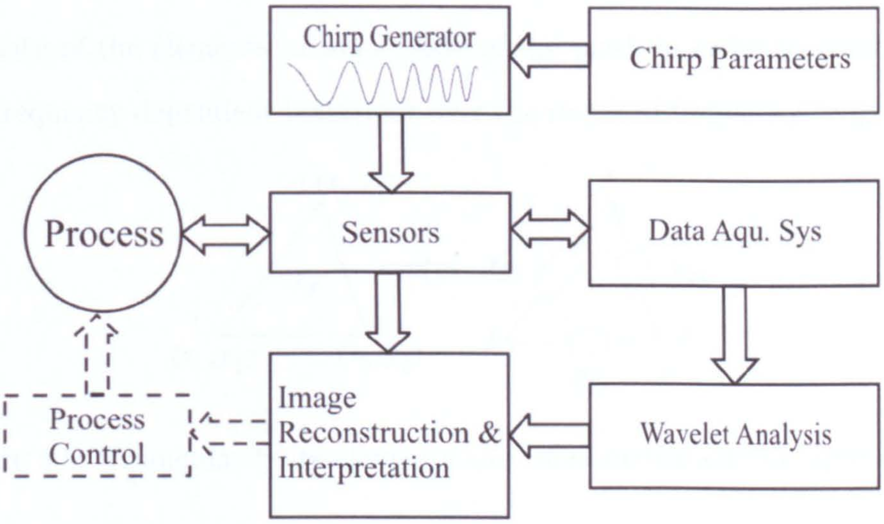

Figure 5.4: Basic block diagram of the proposed method for a Wideband Tomography.

aspect of the use of chirp excitation is the precise extraction of the resulting temporal values. The reason for this is that the accuracy of reconstructed admittivity profile is affected by the accuracy of measured data. The extraction of these values from peripheral measured data set has been discussed in the previous chapter and an algorithm based on the wavelet transform was presented.

The WEIT numerical simulation study was carried out using an adapted EIDORS 2D package [37]. The simulated process peripheral measurements were numerically generated using the mesh model described in the next section. The tomography measurement data sets are then demodulated and analysed by the proposed algorithm .

5.4 Simulated Data Set

The simulated wideband data sets were produced using a mesh model. The admittivity of elements within inhomogeneous regions were updated at the instantaneous frequency f_i of the excitation chirp. The simulation was based upon the analogy of a finite element model to a linear electrical network, as reported in [124] and illustrated in figure 5.5. This offers the possibility of updating the admittivity of the elements in some parts of the mesh in order to create a particular frequency dependent behaviour over the required frequency range. In the

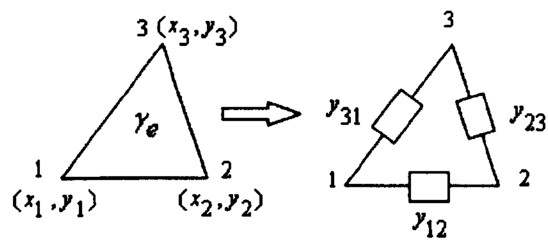

Figure 5.5: Triangular finite elements and its electrical circuit equivalent.

equivalent circuit the entries of the element admittance matrix Y_{mn} at frequency f_i are expressed by:

$$Y_{mn}(f_i) = \frac{\gamma_e(f_i)}{2A_e}(b_m b_n + c_m c_n) \quad m,n = 1,2,\ldots N, \quad m \neq n \tag{5.1}$$

where,$\gamma_e(f_i)$ is the admittance of each element at each frequency, A_e is the area of the element, and the values of b_m and c_m are calculated using node coordination expression[124]. Then, analogous to an electrical network, each element is described by a system of linear equations. These allow the construction of mesh node equations at each frequency point, as expressed by:

$$Y(f_i).V(f_i) = I(f_i) \tag{5.2}$$

where, Y is the total admittance matrix, V is the node voltage and I is the node current matrix. The solution to equation (5.2) gives complex voltages V on the nodes at frequency f_i .

The admittance of each element, γ_e within inhomogeneous regions can be defined by using any appropriate function such as the Cole model[58] which is described by:

$$\gamma(f_i) = G(f) + iB(f) = G_\infty + \frac{G_0 - G_\infty}{1 + (i\frac{f}{f_r})^\lambda} \tag{5.3}$$

where $G(f)$ is the conductivity, $B(f)$ is the susceptivity, G_0 is the conductivity at low frequency, G_∞ is the conductivity at high frequency, f_r is the relaxation frequency and λ is shape factor. Figure 5.6 shows an example of this model which was also utilised in simulation.

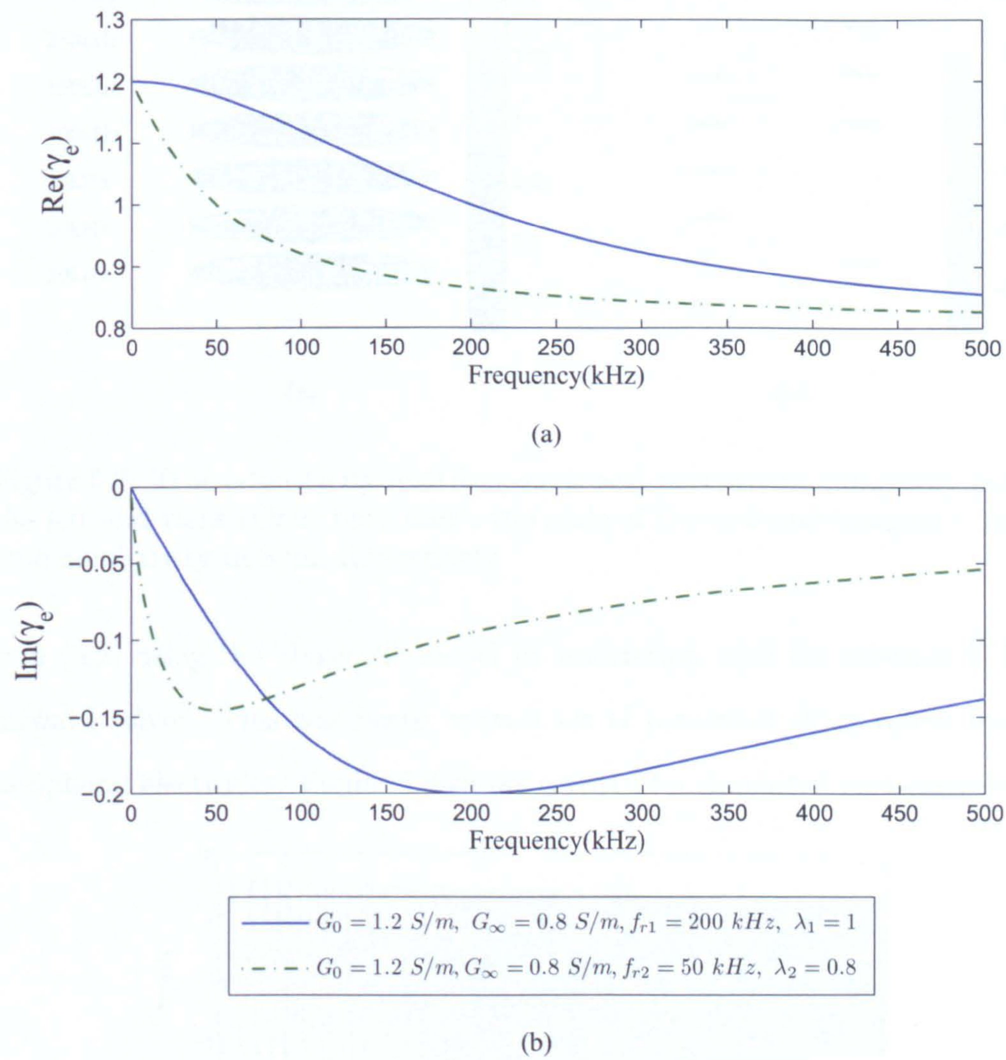

Figure 5.6: Example: real part(a) and imaginary part (b) of $\gamma_e(f)$ for two sets of parameters.

For these studies a fine circular mesh with the diameter of 1.5 cm was employed. This mesh consisted of 1952 first-order triangular elements, 1025 vertices and 16 peripheral electrodes. The background admittivity was set to (1-i0.1). To provide measurements over the required frequency range a Chirp is used as the excitation signal. Figure 5.7, for example, shows the true distribution at eight different frequencies. The simulation was performed by solving the system equa-

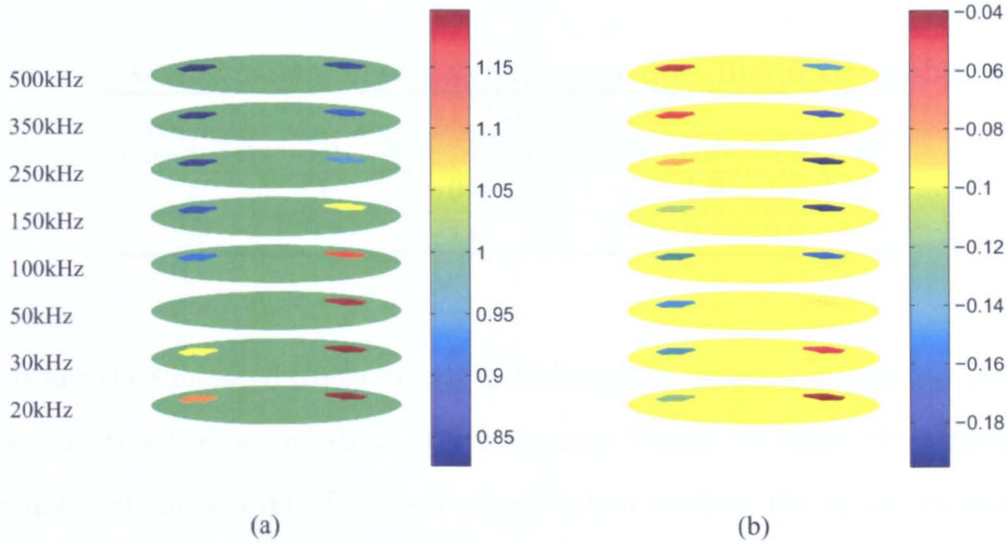

Figure 5.7: True admittivity distribution γ: real part(a) and imaginary part (b), the left and right colour bars shows the scale of the real and imaginary parts of true admittivity in S/m, respectively.

tion (5.2) using the above 2D model in association with the adapted EIDORS forward solver. This was based upon a set of measured chirp values from the peripheral electrodes. Figure 5.8 shows a part of a simulated measurement.

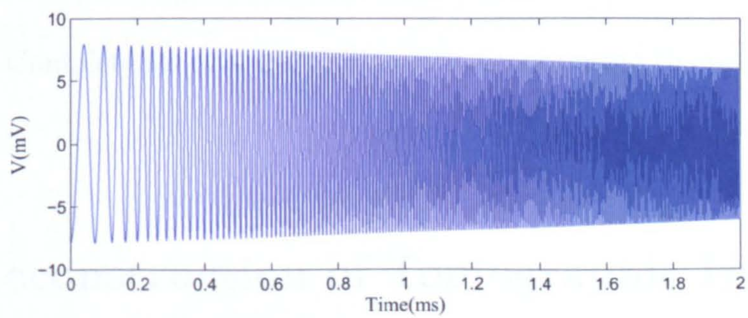

Figure 5.8: A part of a simulated measurement, the excitation chirp was a sweep from 10 kHz to 510 kHz within $T = 5$ ms.

5.4.1 Wavelet Analysis

The complete set of the measurements generated by the above procedure were analysed using the algorithm based on the wavelet transform illustrated in the previous chapter to reveal spectral band data sets. To perform this, first the appropriate wavelet parameters must be selected, for instance, table 5.1 gives these parameters for a chirp with a sweep from 10 kHz to 510 kHz over a period of 5 ms at eight frequency points.

Table 5.1: Wavelet parameters for a chirp swept from 10-510 kHz within 5ms.

Wavelet parameters	Frequency(kHz)							
	20	30	50	100	150	250	350	500
f_c	1	0.6	0.6	0.9	1	1.9	1.5	1.9
f_b	0.3	1	1.3	0.6	0.6	0.1	0.4	0.3

Analysing the simulated Chirp signals by utilising the optimum parameters yields the complete set of potentials at each frequency. Figure 5.9 shows the simulated measurements at 50 kHz. These values were then used for the reconstruction of admittivity distribution.

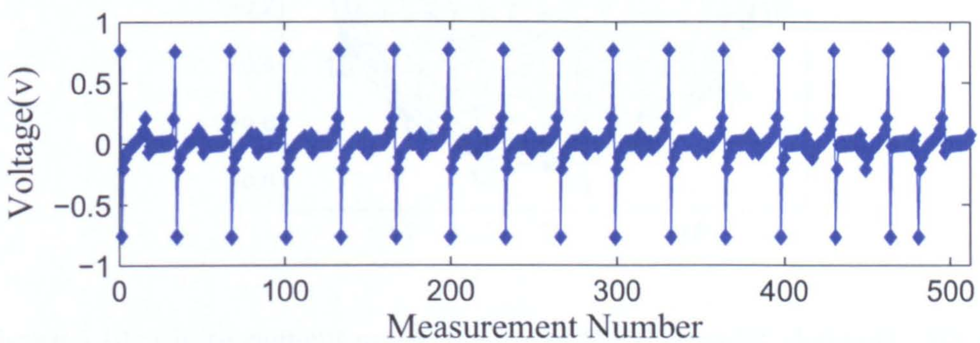

Figure 5.9: Complete set of simulated measurements using the proposed method at 50 kHz.

5.5 Reconstruction of Tomographic Image

The inverse solver available in the EIDORS suite was adapted for the use in this research. The nonlinear regularised Gauss-Newton algorithm described by equation (2.25) in chapter two was deployed. The termination criterion for all reconstruction conducted in this chapter was Morozov's criterion and the regularisation parameter was selected by visual inspection. Both error criterion and α were set to (1×10^{-6}) unless other values are stated. The potential on the excitation electrodes are ignored and the Jacobian matrix was also modified accordingly. The initial values for admittivity distribution γ_0 were calculated by using the approach mentioned in section 2.6.1.

The reconstruction was carried out by using a coarser finite element mesh in order to avoid the 'inverse problem crime' [125] of over-estimation from ill-posed and sparse data. The mesh model consisted of 488 first-order triangular elements, and 269 vertices, as shown in figure 5.10.

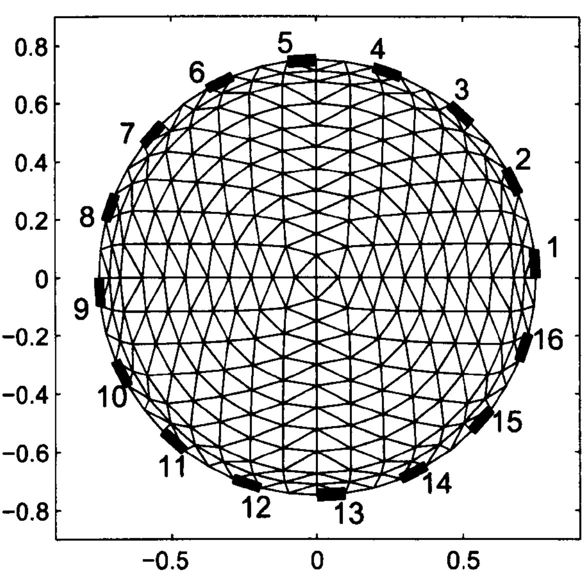

Figure 5.10: Finite element mesh consists of 488 triangular elements, 269 vertices and 16 peripheral electrodes.

Various types of tomography images can be reconstructed for real and complex admittivity problems. In the real case, the image can only be reconstructed for the conductivity, whereas in complex case the tomography images can be reconstructed for the real and imaginary parts and also for the magnitude of the admittivity distribution. Since, in the second case the reconstruction of the tomographic images may lead to reveal more information about the process, this type of image may be preferable. In this chapter, the WEIT simulation study are presented using an example of a complex admittivity distribution with inclusions illustrated by the model shown in figure 5.6. Tomographic images were reconstructed for the real and imaginary parts at frequencies given in table 5.1. They are shown in figures 5.11 and 5.12.

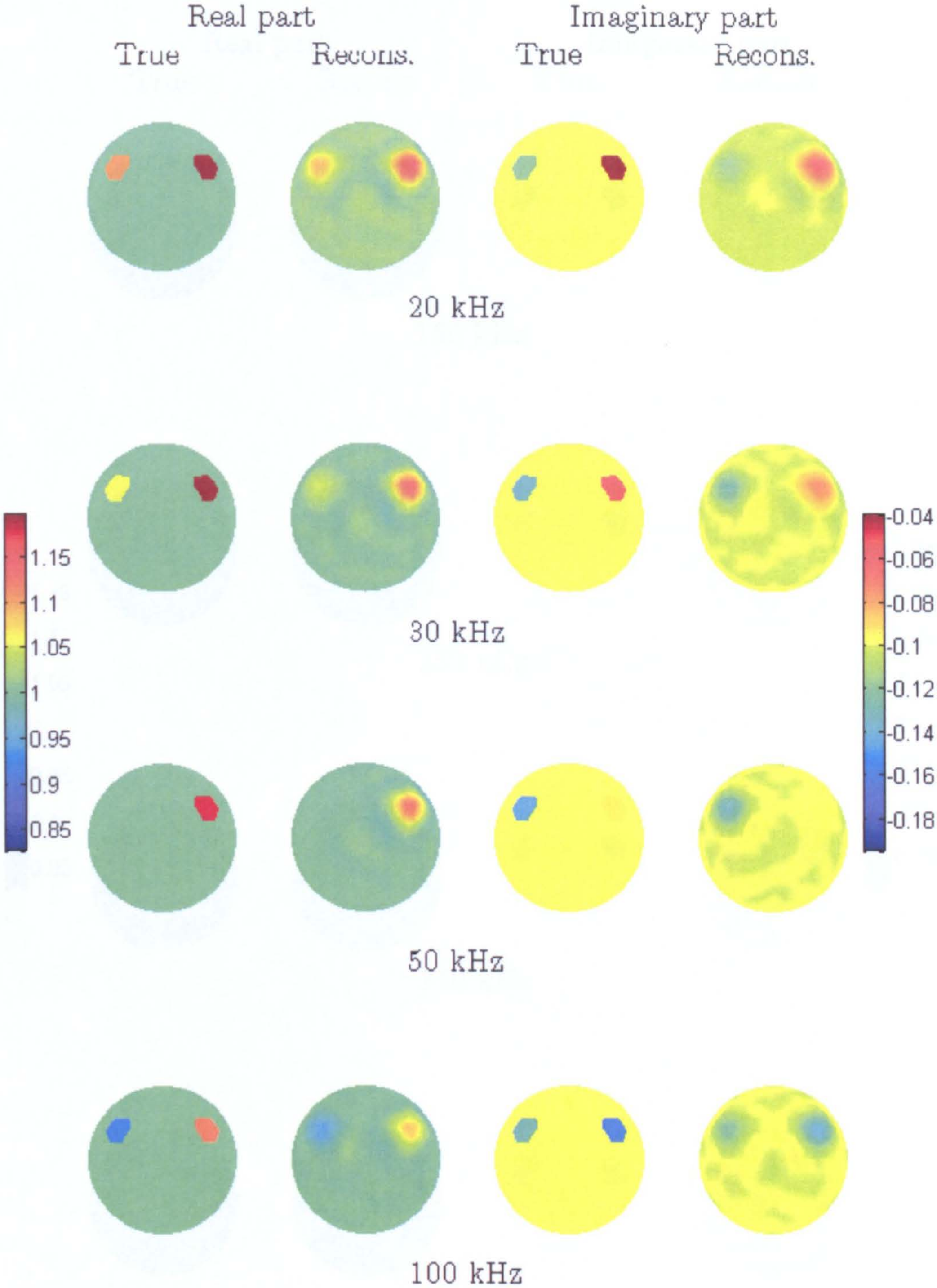

Figure 5.11: True and reconstructed tomographic images at frequencies: 20, 30, 50 and 100 kHz, the left and right colour bars show the scale of real and imaginary parts of admittivity (in S/m), respectively.

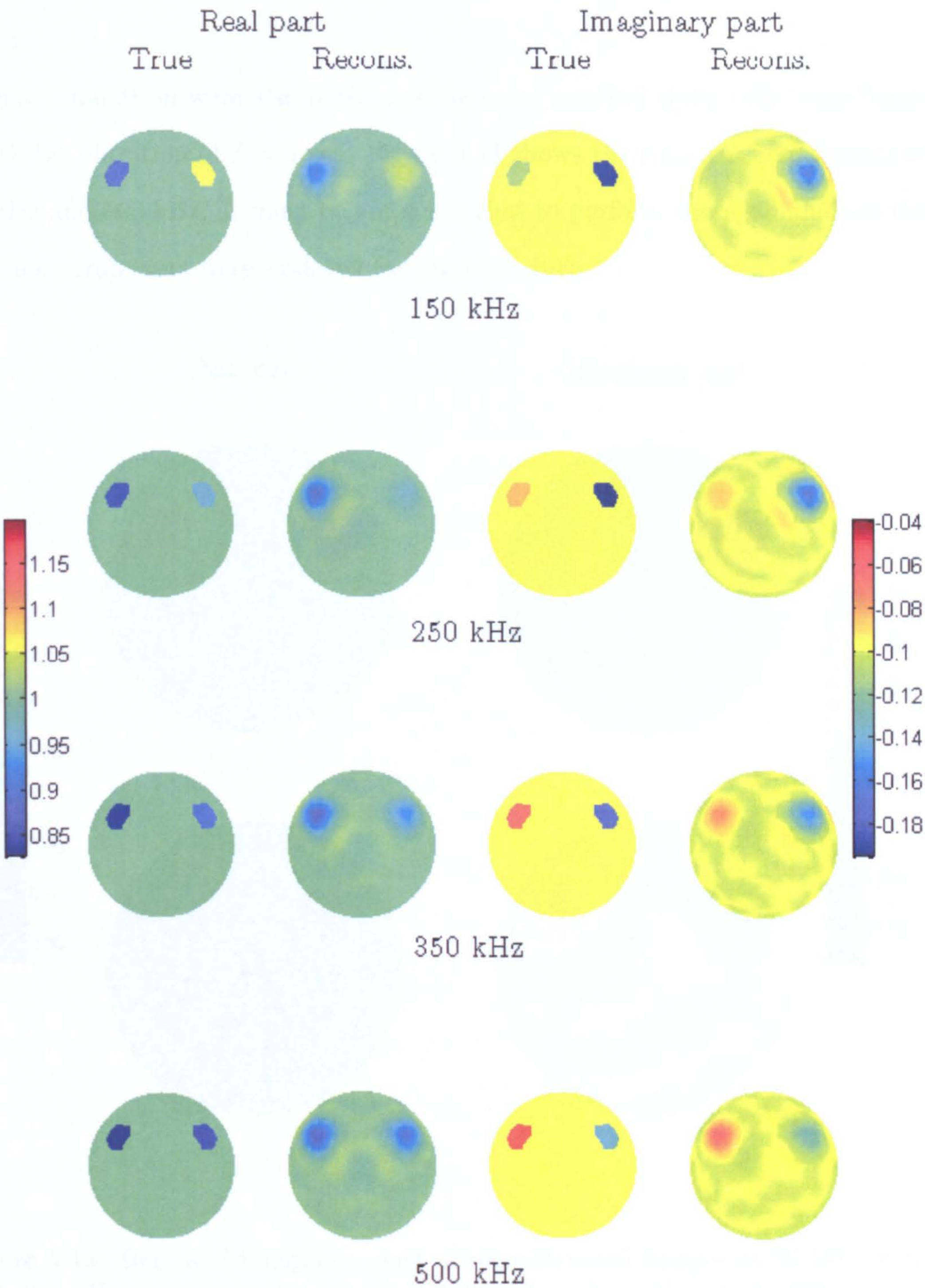

Figure 5.12: The continue of figure 5.11 at frequencies 150, 250, 350 and 500 kHz.

In above figures, the colour bars are similar and the left and right bars show the scale of the real and imaginary parts of the admittivity distribution, respectively.

Similar simulation were also performed by using another chirp with same bandwidth but duration of $T = 1$ ms. Figure 5.13 shows the reconstructed images at 20 kHz and 500 kHz. It must be emphasis that to perform these simulations the wavelet parameters were updated for the new chirp.

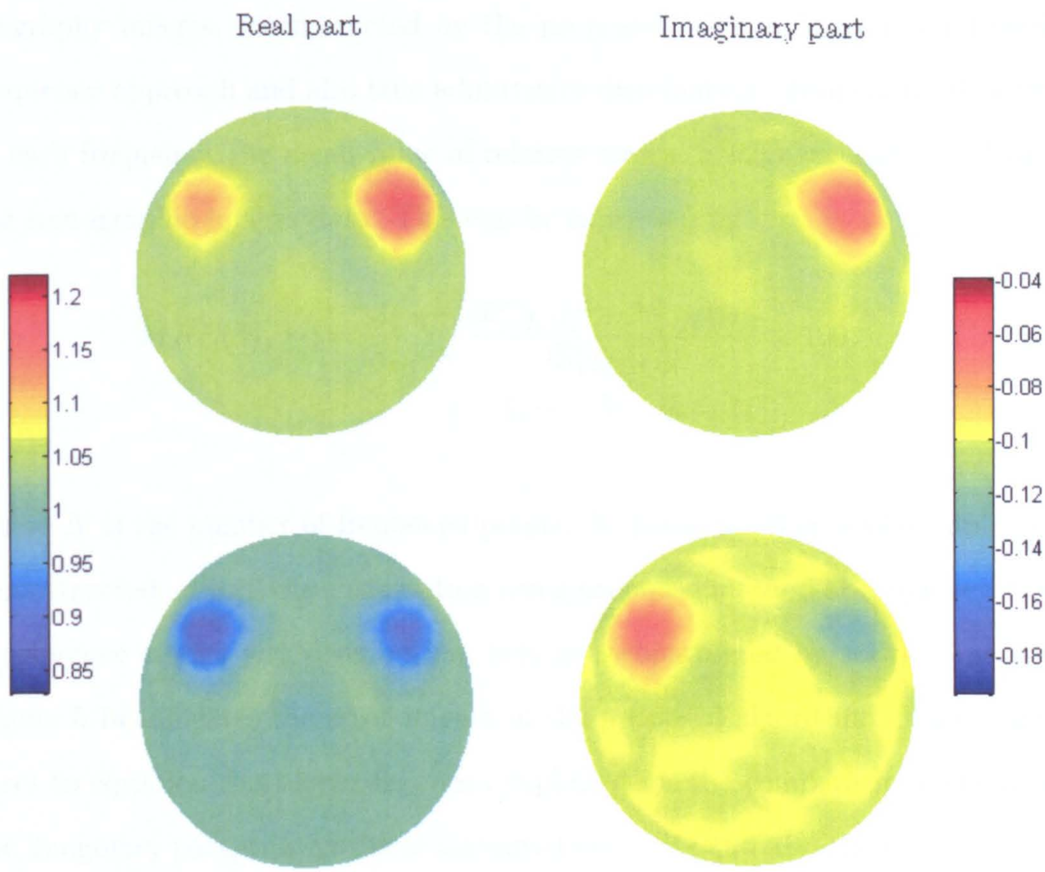

Figure 5.13: Real and imaginary part of reconstructed images at 20 kHz (top) and 500 kHz (bottom), the left and right colour bars show the scale of real and imaginary parts of admittivity (in S/m) and the simulated data set were generated using a chirp with $T = 1$ ms.

The results of above simulations show clearly the variation of the frequency-dependent inclusions over frequency range. These images, in fact, give the spectral information besides the spatial distribution. Thus the tomography images, based upon frequency banding of the excitation signal, are able to reflect the frequency-dependent characteristics in the process. These simulations also verify that the proposed method has the flexibility of adapting the characteristics of the excitation chirp to meet the process requirements.

5.6 Error Impact on Tomographic Images

The performance of the method is demonstrated through a comparison of tomography images, reconstructed by the proposed method, conventional single frequency approach and also true admittivity distribution. To measure the error at each frequency, the mean value of relative errors (MRE) was calculated from the tomographic images data. This can be expressed by :

$$MRE(\widehat{\gamma}_f, \gamma_f) = \frac{1}{N_e} \sum_i \frac{|\Re[\widehat{\gamma}_{f_k}(i)] - \Re[\gamma_{f_k}(i)]|}{|\Re[\gamma_{f_k}(i)]|} \times 100 \qquad (5.4)$$
$$i = 1, \cdots, N_e \;, \quad k = 1, \cdots, N$$

where N is the number of frequency points, N_e is the number of elements, $\widehat{\gamma}_f$ is reconstructed admittivity distribution using proposed method at frequency f, γ_f is reference admittivity distribution, true or reconstructed by another method. Figure 5.14 indicates the error impact of the proposed algorithm. Similar measures to equation (5.4) have also been exploited for the comparison of errors on the imaginary part, the synthetic measured data sets and also the noise analysis in the rest of this chapter.

To study the error impact, the MRE values were calculated on the reconstructed real and imaginary parts using WEIT in respect to the true distributions and those reconstructed using SFEIT at eight frequencies. The corresponding results are shown in figure 5.14.

These figures demonstrate that, except the error at 20 kHz, which is greater than at other frequencies, the errors show a slight increase in comparison to those reconstructed directly. Here, the minimum error value is 0.018% at 100 kHz, while the maximum value is at 20 kHz with an error value about 1.6%.

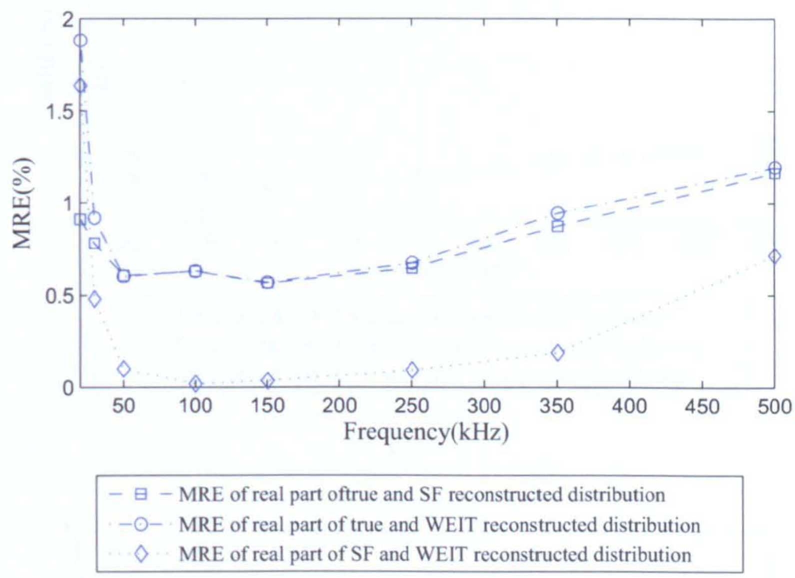

(a)

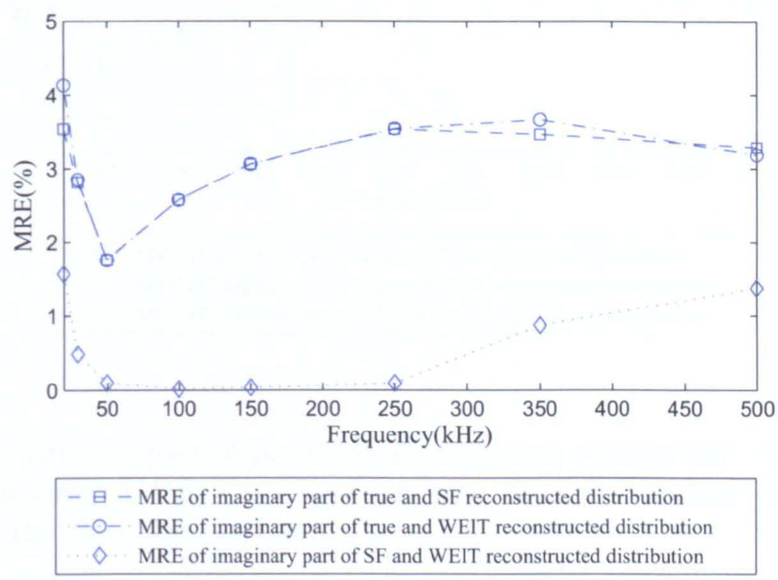

(b)

Figure 5.14: Error impact of proposed algorithm on tomographic images at different frequencies: $MRE(\widehat{\gamma}, \gamma)(\%)$ of real part (a) and imaginary part (b), the duration of the chirp was T=5ms.

To see the impact of the characteristics of the excitation signal on the error, the above simulations were repeated by using a modified chirp with duration of $T = 1$ ms; figure 5.15 shows the results for this simulation. In this case,

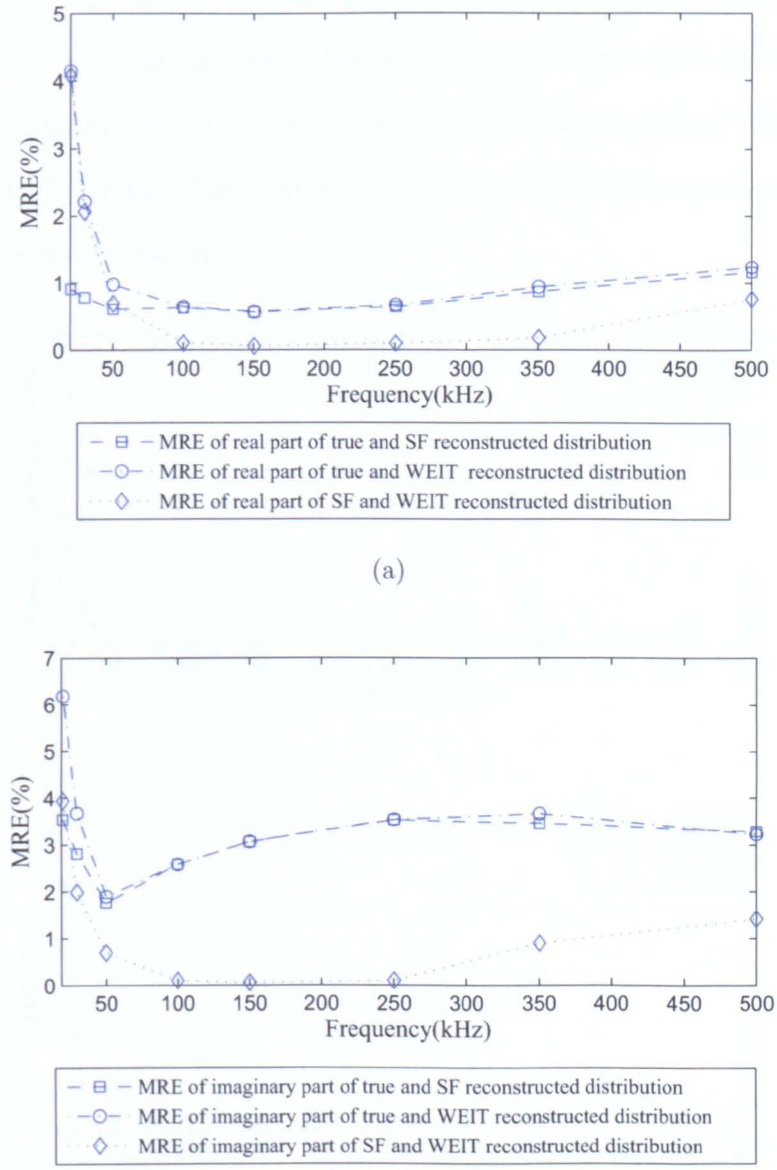

Figure 5.15: Error impact of proposed algorithm on tomographic images at different frequencies: $MRE(\widehat{\gamma}, \gamma)(\%)$ of real part (a) and imaginary part (b), the duration of the chirp was T=1ms.

the comparison of the errors with those demonstrated in figure 5.14 shows a greater error at lower frequencies including 20, 30 and 50 kHz, while there is no significant difference at other frequencies. The minimum error value is 0.059% at 150 kHz whereas the maximum values is at 20 kHz with a value about 4.08%.

These errors originate in the algorithm and arise from the wavelet transform. To verify this, the relative error on the training waveform and also $MRE(\widehat{V}, V)$ calculated on the complete sets of the simulated measurements by WEIT, $\widehat{V}$

and SFEIT, V at various frequencies, are compared. These are presented in figure 5.16. By comparing these figures with those shown in 5.14 and 5.15 it is evident that the errors are generated by the presented method and that these are propagated through the simulated measurements and consequently appear in the reconstructed images.

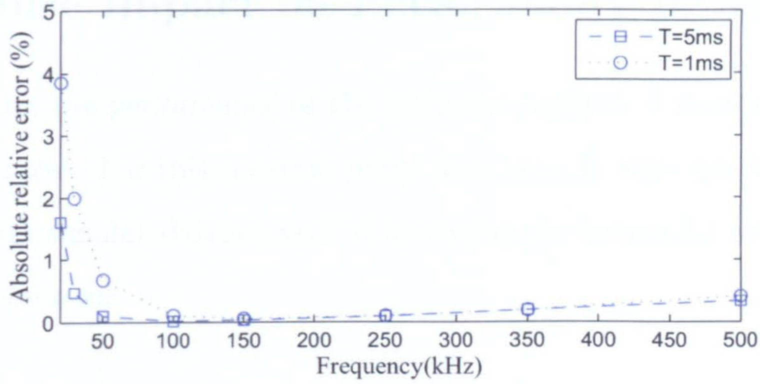

(a)

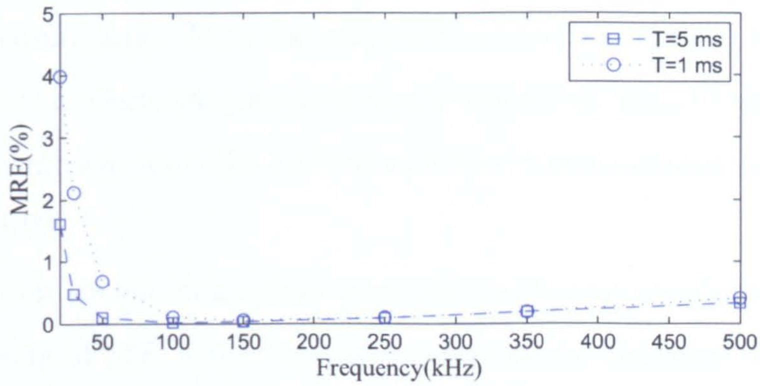

(b)

Figure 5.16: Error of proposed algorithm at different frequencies: relative error on the training waveform (a) and $MRE(\widehat{V}, V)(\%)$ on the simulatted measurements using SFEIT and WEIT (b).

The reason for the greater errors at some frequencies, for instance 20 kHz, was discussed in the previous chapter. It was shown that the necessary values can be accurately estimated under conditions stated in Section 4.4.4 in Chapter 4; The verification of these restrictions on the Chirp signals described above for low frequencies implies that it is not possible to extract the temporal values with the accuracy achieved at other frequencies. For the same reason the errors will increase when the chirp duration decreases, which can also be verified in figure 5.16. However, these minor errors (in these simulation conditions) are offset by the corresponding higher quality of estimation of the process spectral information.

5.7 Noise Impact on Performance of Method

In this section the performance of the proposed method is investigated in the presence of noise. For this purpose, noisy data sets, $\widetilde{V}$ were produced by contaminating the simulated data sets, V described in the section 5.4 with zero-mean Gaussian noise n as:

$$\widetilde{V} = V + n \tag{5.5}$$

The standard deviation (STD) of the noise was varied from 1% to 5% of corresponding measurement. Then the proposed method was applied to these data sets to extract the electrode potentials on a frequency set from 10 kHz to 500 kHz with 15 kHz increments. The performance was then evaluated by calculating $MRE(\widetilde{V}, V)(\%)$.

For comparison similar simulations were also performed on the measurements simulated using SFEIT. The results of simulations are presented in figure 5.17. The noticeable improvement is evident by comparison of the resulted error by SFEIT, figure 5.17a and that of proposed method, figure 5.17b. These figures demonstrate an improvement better than 600%. Therefore, it is verified that exploiting the presented method leads to less sensitivity to the noise and that it is able to provide better accuracy in the presence of noise. The reason for this improvement is due to the nature of bandpass filtering of the wavelet transform which will decrease the noise impact [126].

Figure 5.18 exhibits two images reconstructed using noisy data at 20 kHz and 500 kHz, corresponding to the minimum and maximum errors, by using the proposed method when the STD was set to the 1% of the noisefree simulated data.

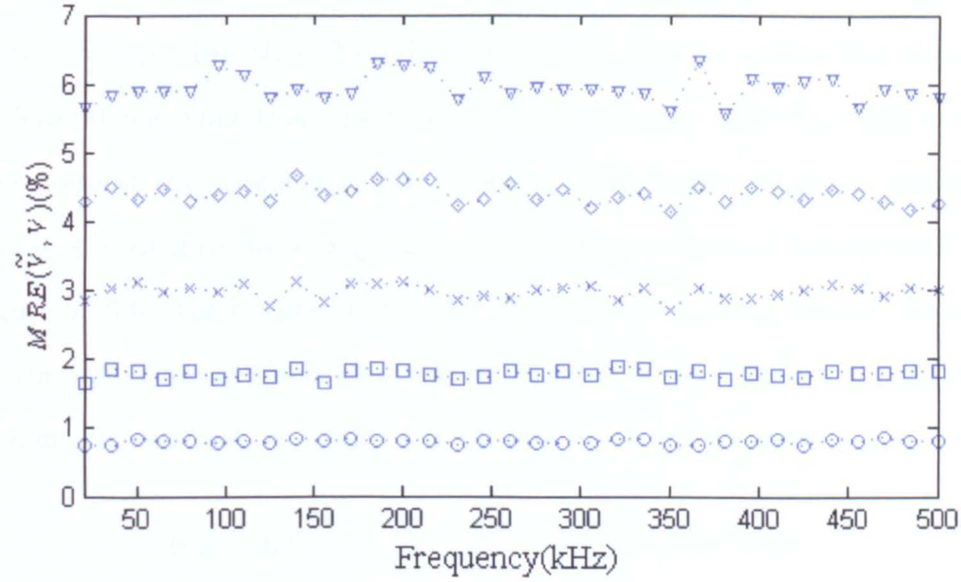

(a)

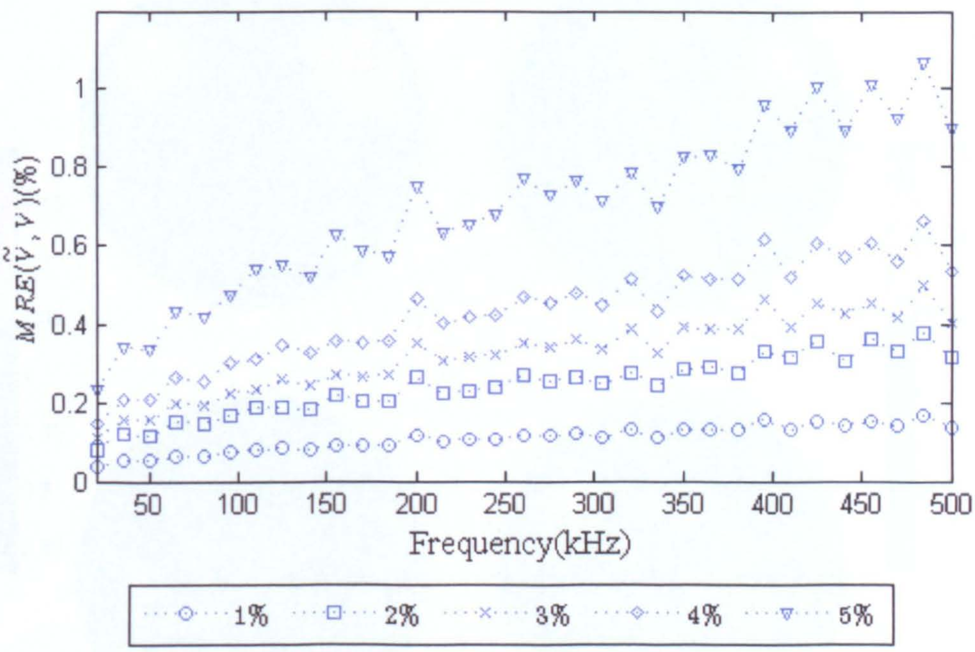

(b)

Figure 5.17: Performance of the presented method in presence of noise: $MRE(\widetilde{V}, V)(\%)$ using SFEIT (a) and with presented method (b), where V and $\widetilde{V}$ are noise-free and contaminated measurements, respectively, and the noise STD was set to the different values from 1% to 5% of corresponding measurement.

The regularisation parameter ($\alpha = 1 \times 10^{-6}$) was equal to the value used in the section 5.5. It should be noted here the reconstruction at a higher level of noise may require the modification of the value of the regularisation parameter [48]. However, here due to the presence of noise the reconstructions converged with final square error less than 2×10^{-6}. At 20 kHz the reconstruction converged after 5 iterations while this raised to 11 for the image at 500 kHz which is due to higher noise at this frequency. The presence of the noise introduces artifacts in the images leading to the wrong analysis and interpretation of tomographic data. In figure 5.18 for the images at 500 kHz although the true inclusions can still be seen, the significant artifacts cause misinterpretation, for instance the number of inclusions. In contrast, the images at 20 kHz shows more accurate images.

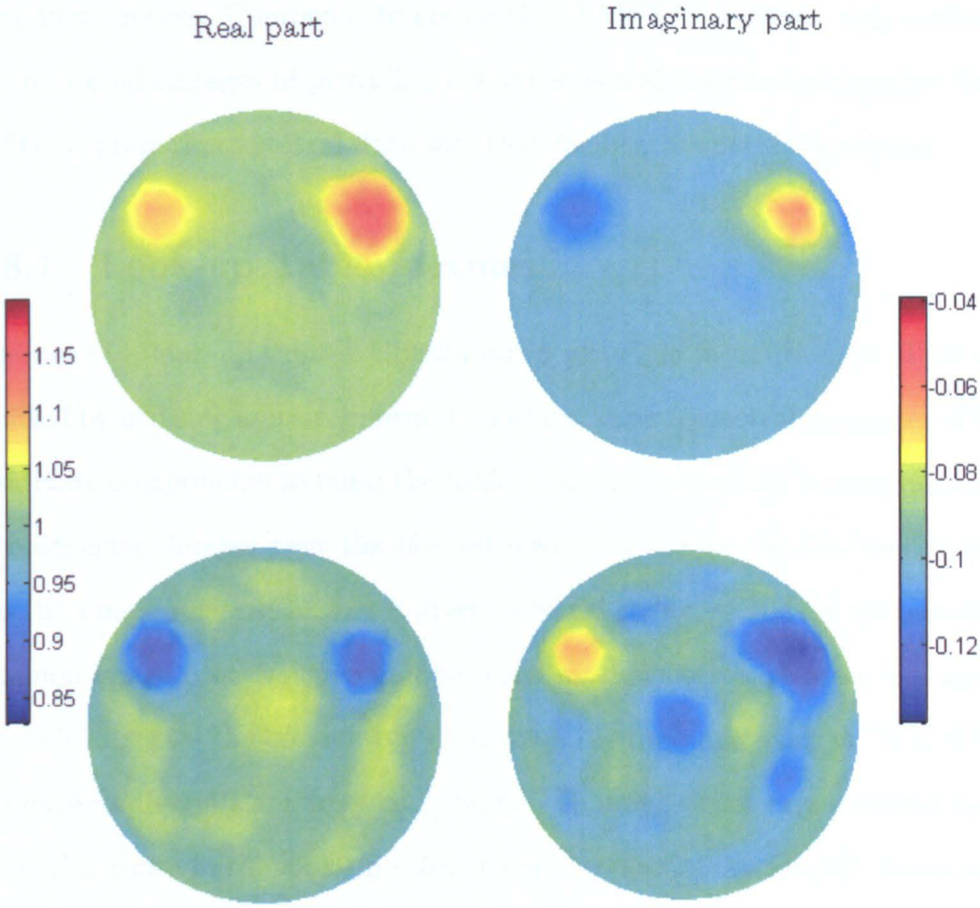

Figure 5.18: Tomography images reconstructed in the presence of noise at 20 kHz (top) and 500 kHz (bottom).

5.8 Spectral Tomographic Data Analysis

The simulation results in previous sections have verified that the proposed method is able to extend the SFEIT systems to the WEIT system. Since this method leads to the formation of the tomographic images over desired frequency range, it has the capability to provide local spectrum of the admittivity distribution. In essence, this relates the characteristics of the process or its materials to the spectral information. Hence in suitable applications we may expect that the band-segmented spectral data, in conjunction with a look-up table, or a model based method, may be deployed to identify the materials, or indicate their presence in a process. Compared to conventional MFEIT systems, this method has the major advantages of providing enough spectral information besides the flexibility in preparing spectral data sets that facilitates spectral analyses.

5.8.1 Look-up Table Method

The use of a look-up table is illustrated in principle in figure 5.19. This can be realised by utilising a priori information of the known spectral responses of known candidate components to build the table; and then using this in conjunction with reconstructed images over the desired frequency range. In the spatial domain specific image regions, having a given spectral index, would be extracted using common image processing techniques such as image segmentation. For instance, figure 5.19 shows the conductivity variation of three materials A, B and C over the expected significant frequency range. By comparing experimental spectral data with those in the look-up table it may be possible to identify material C in this process.

To see the feasibility of this method, a simulation is illustrated using the tomography images reconstructed with noisy data sets generated as described in the last section, when the STD was set to the 1%. The tomographic images were then reconstructed at all frequencies mentioned in the previous section. The regularisation parameter was ($\alpha = 1 \times 10^{-6}$). In this simulation, due to the

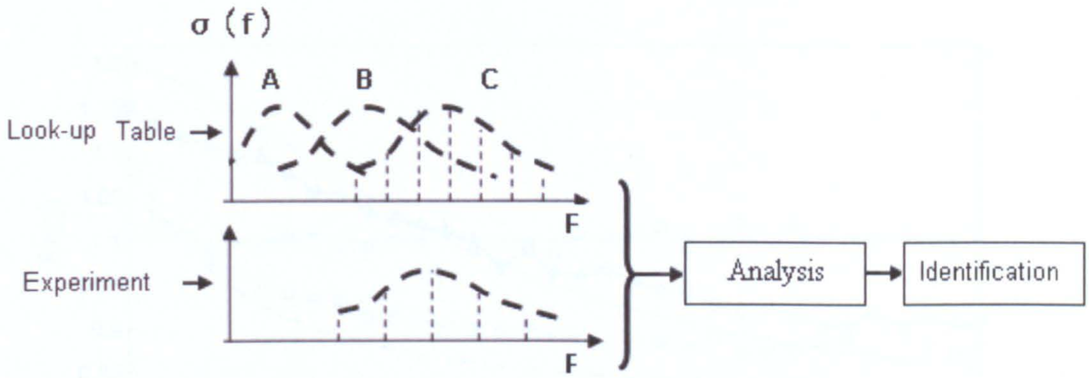

Figure 5.19: Spectral study using Look-up table method.

presence of noise, the reconstructions converged with final square error less than 2×10^{-6}. To investigate the trajectories of the local spectrum admittivity three regions were selected corresponding to the two inclusions, R_1 and R_2, and the background admittivity distribution, R_3, as shown in figure 5.20. The regions were selected based on the structural information provided by the reconstructed images. Each of these regions consists of 10 elements.

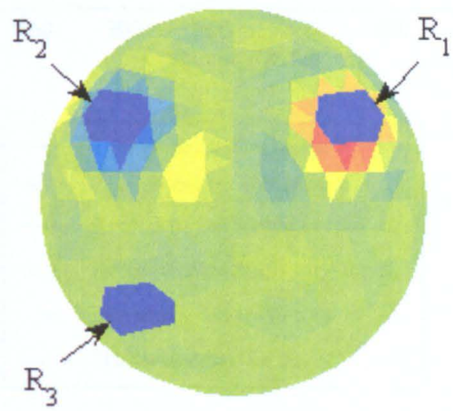

Figure 5.20: Selected regions on the tomography image.

Local spectral trajectories of these regions were then determined by averaging the admittivity values on the corresponding elements in the each regions. It is evident that the noise impact on the the averaged trajectories is less than the trajectory of each individual element. The results are shown in figure 5.21 together with the true models. This figure verifies that the regions can be distinguished from each other by their trajectories, thus by comparison of the true with the

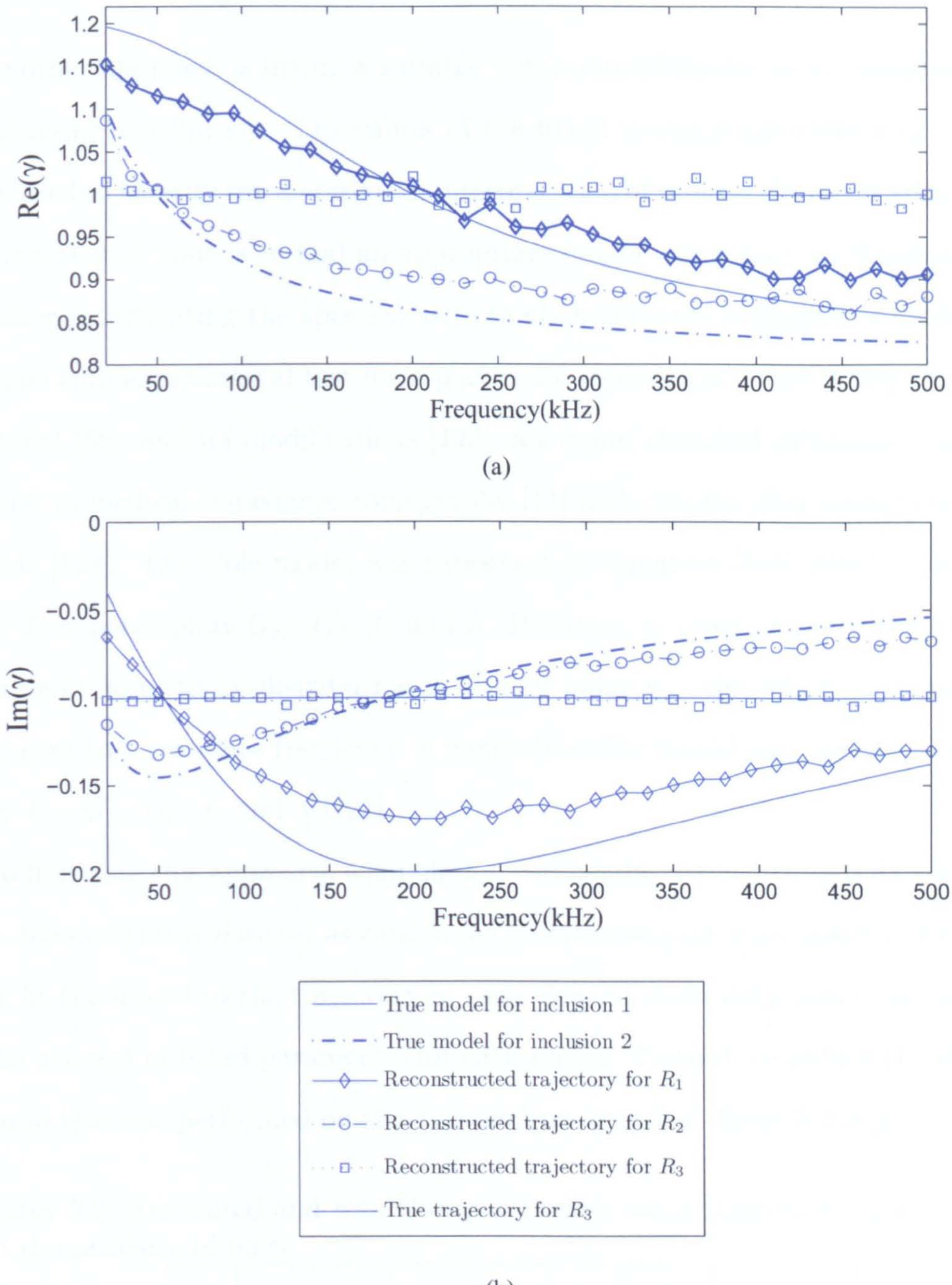

Figure 5.21: Trajectories of the real and imaginary parts of regions R_1, R_2 and R_3 at various frequencies, real parts (a) and imaginary parts (b).

estimated trajectories the selected regions can be matched with true models. This simulation implies that in practical situations it may be possible to exploit similar procedure to estimate local trajectories of admittivity distribution which may lead to recognition or identification of process parameters or materials.

5.8.2 Fitting Parametrised Model

Another approach is fitting a suitable parametrised model to the estimated admittivity distribution. The values of the fitted model parameters may then be utilised to identify the materials or interpretation of process characteristics. Here, the essential issue is to find an appropriate model which may be determined by either investigating the spectral aspects of the process materials or conducting some trial experimental test for a particular application. For instance the Cole model [58], and its modifications [123], for liquid chemical substances has been used in medical impedance tomography [11] and also for pharmaceutical materials [123]. The Cole model was expressed by equation (5.3) which is specified by four parameters G_∞, G_0, f_r and λ. However, in practice, since the absolute value of admittivity distribution is usually unknown, the relative expression in respect to a reference frequency is preferable. The model can then be expressed by $k = G_\infty/G_0$, f_r and λ [127].

To illustrate this approach, a simulation was conducted by fitting the Cole model to the same noisy data set as used in the previous section. Obviously, it is possible to fit the model to the trajectory of each element separately, and then calculate the average of fitted parameters for each region. Instead, to reduce the effect of noise this was performed on the averaged trajectories. Table 5.2 and figure 5.22

Table 5.2: Estimated and true Cole parameters using trajectories of the regions in the presence of noise

Region	λ		f_r(kHz)		$k = G_\infty/G_0$		Residual Error
	True	Estimated	True	Estimated	True	Estimated	
R_1	1	0.9060	200	202.5	0.67	0.7145	2.074×10^{-4}
R_2	0.8	0.8329	50	42.28	0.67	0.7418	2.090×10^{-4}
R_3	-	1	-	29.42	-	0.9719	2.1×10^{-4}

demonstrate good agreement between estimated and true model parameters.

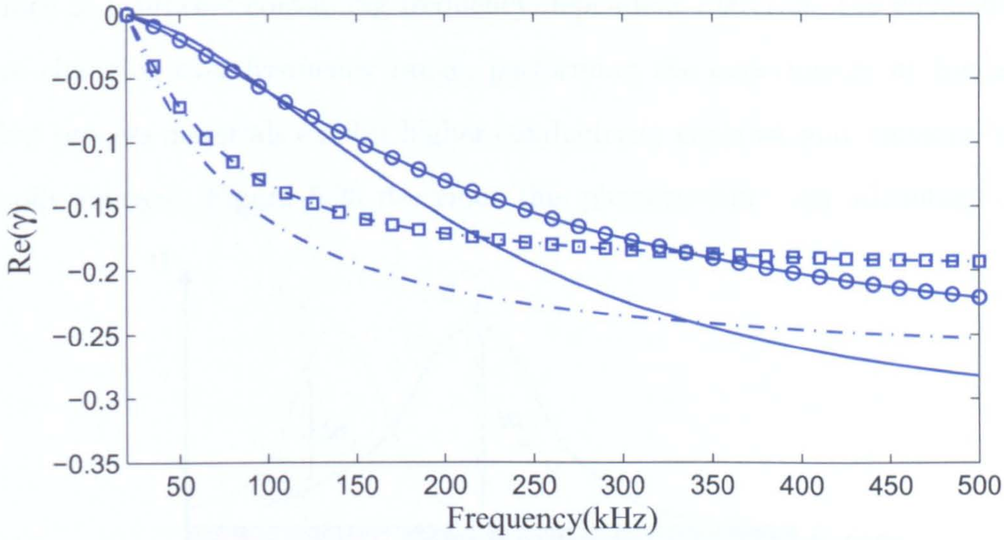

(a)

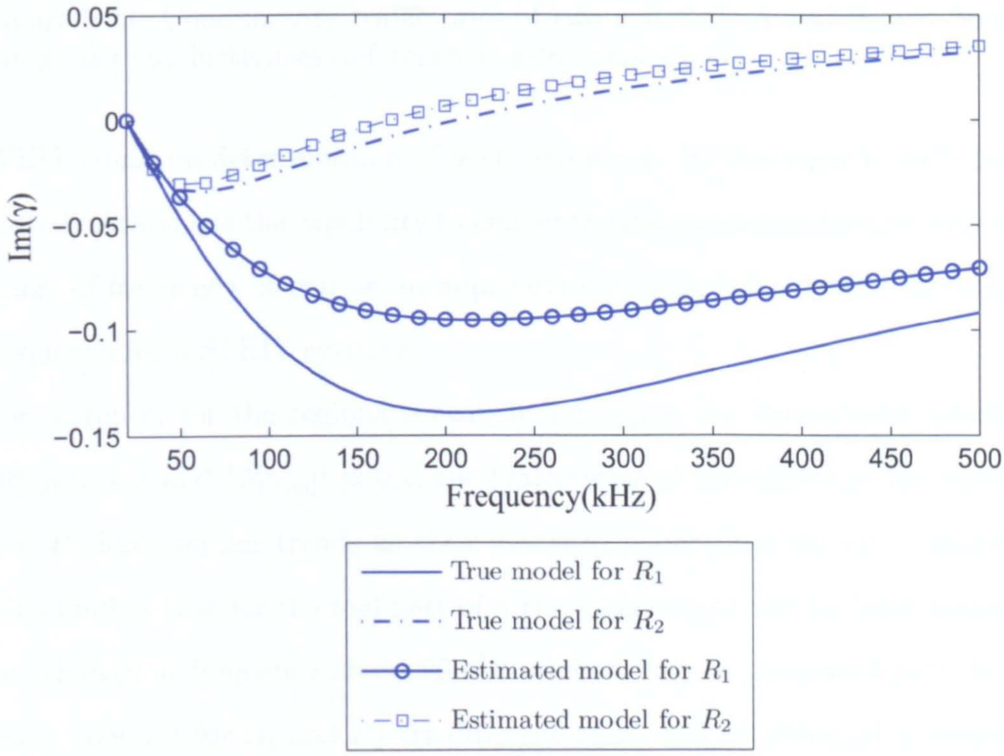

(b)

Figure 5.22: True Cole model and the estimated model for regions R_1, R_2, real parts (a) and imaginary parts (b).

5.8.3 Improving Conductivity Contrast Using WEIT

Since in a process containing frequency-dependent materials the conductivities are changing over frequency range, performing the experiments at frequencies that process materials exhibit higher conductivity contrast may enhance tomography images. Figure 5.23 describes this phenomenon. An advantage of the

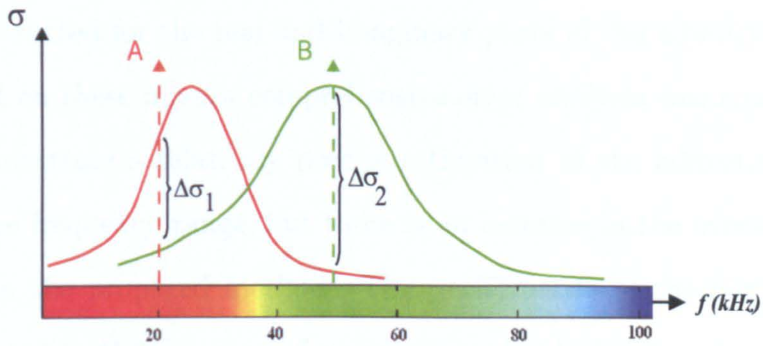

Figure 5.23: Conductivity trajectories of two materials A and B over frequency range, $\Delta\sigma$ conductivities difference at a frequency.

WEIT could be determination of such frequency. In this regard, since the presented method has the capability to deliver the measurement data set over a wide range of frequency, it can be an appropriate approach to identify the optimum frequency for a SFEIT systems.

For instance, for the regions shown in 5.20 since the background admittivity $|\Re[\gamma_{R_3}]| \approx 1$ and $|\Im[\gamma_{R_3}]| \approx 0.1$, the trajectories of the contrasts for regions R_1 and R_2 have similar trends as their averaged trajectories shown in figure 5.21. This implies that for the real part of γ the highest contrast for both regions can be achieved at frequency about 20 kHz whereas for the imaginary part the maximum contrast for R_1 and R_2 are different which can be obtained at frequencies about 200 kHz and 500 kHz, respectively.

In [128] for a conductive distribution the fraction $C = \sigma_A/\sigma_B$ is also defined as conductivity contrast, where σ_A is the conductivity of region A within a larger region B with conductivity σ_B. This definition was adapted for the multi-frequency imaging in [129].

5.9 Conclusion

The chapter presents a novel method for the WEIT using chirp excitation, based on the wavelet transform. The performance of the proposed method has been investigated by various simulations. The synthetic data sets were produced by using a 2D mesh with two frequency-dependent regions. The tomography images were reconstructed for the real and imaginary parts of the admittivity distribution. Based on these images comprehensive error analysis was conducted. The results demonstrate a relatively precise estimation of the admittivity distribution over the frequency range, but there is an increase in the average error that originates in the proposed method. The performance of the method also has been evaluated in the presence of noise. This simulation has shown significant improvements in the noise performance. The chapter concludes with an illustration of two approaches for the analysis of spectral tomographic data. The results imply the potential of the WEIT to provide a range of flexible local spectral admittivity information, which can enhance the identification of process materials or process parameters. The results of this chapter in general support the conclusion that utilising Chirp excitation efficiently facilitates tomographic measurement over a desired wideband frequency range, but this is achieved at the minor cost of extra processing complexity and a slightly increased average error.

Chapter 6

Experimental Feasibility Study

6.1 Summary

This chapter demonstrates the feasibility of the proposed method through experimental simulation. For these trials a single-channel EIT Chirp excitation was implemented which is briefly described. The tests were conducted using resistive paper and also a 16-electrode EIT rig. The experimental data were then analysed and tomography images were reconstructed by using the extracted data over the relevant frequency range. The chapter will also present the capability of a method for four-probe impedance spectroscopy used for performing reference tests on food materials.

6.2 Hardware Implementation

This section presents an overview of the implementation of the electronic system. This provides a single-channel EIT chirp excitation implementation to perform the experimental simulations, as an alternative to a real-time parallel data collection system, to support pseudo-static tests. Figure 6.1 shows the block diagram of this system.

In this system, the excitation Chirp was generated by a direct digital synthesis (DDS) unit [72] controlled by a host computer. Following initial amplifica-

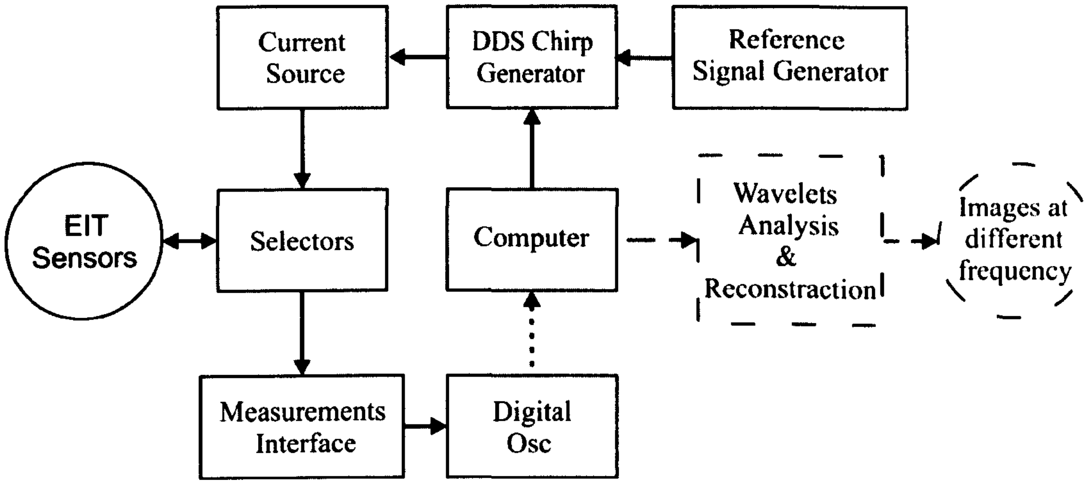

Figure 6.1: Block diagram of hardware.

tion the waveform is converted into a current stimulus supplied from a current source based upon a LT1228 fast trans-conductance amplifier [130]. The current was applied to the excitation electrodes using a selector board, according to the adjacent electrode protocol. To realize a simple feasibility test-bed the sensed voltages were differentially measured using a purpose-designed high-input impedance buffer, and then stored using a LeCroy digital storage oscilloscope. The following sections present further details of the implemented hardware.

6.2.1 DDS-based Chirp Generation

In this section the generation of the Chirp signal is described. As discussed in chapter 3, a Chirp is a signal which transits between two frequencies over a specified time duration. The frequency transition can be a linear or nonlinear function of time; a linear or nonlinear Chirp, respectively. To generate a Chirp signal a DDS technique was employed. As mentioned in chapter 2, this technique supports the generation of a very stable and accurate signal.

Figure 6.2 shows the block diagram of the DDS-based Chirp generation unit [72]. In this figure, the phase accumulator Ac2 is driven by summation of initial frequency f_{in} tuning word and the output of the frequency accumulator Ac1. The accumulator Ac1 recursively sums the frequency increment, tuning word Δf, at a rate determined by the ramp clock. This means that at each clock pulse the

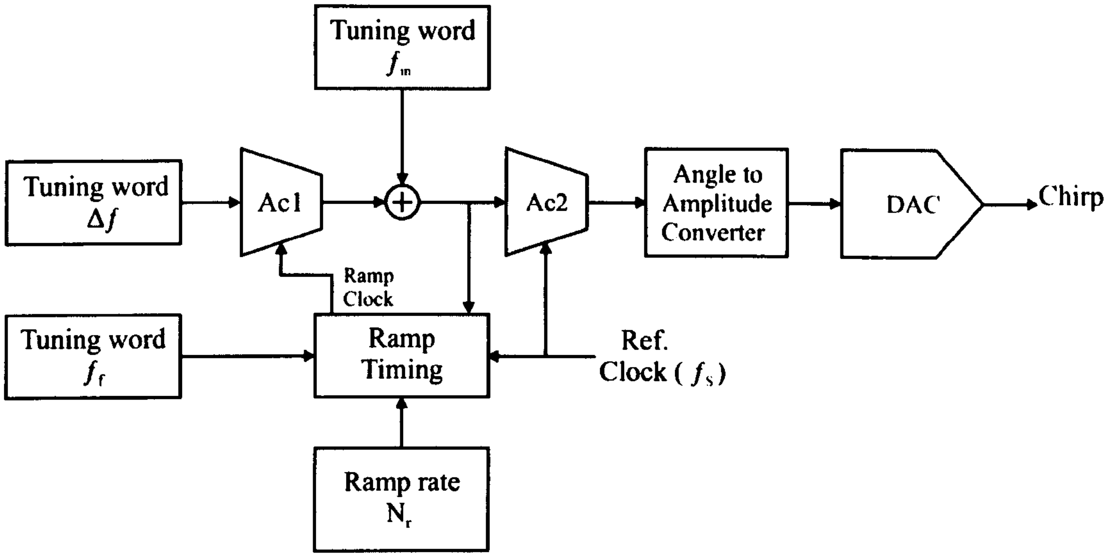

Figure 6.2: Block diagram of DDS-based Chirp generation.

input to the Ac2 is increased by Δf and consequently the output frequency f is updated each time. Both linear and nonlinear chirps can be generated by appropriate modification of the frequency increment. If the ramp clock is generated at equal intervals and the Δf word is constant, the slope of the output frequency variation is also constant and the output Chirp will be linear. To synthesis a nonlinear Chirp, the flexibility of the DDS technique allows the modification of Δf, or ramp rate, within the transition from the initial frequency, f_{in}, to the final frequency, f_f, according to the desired nonlinear function. In this work all experiments were carried out using a linear Chirp generated using an evaluation board supporting an AD9852 digital synthesiser [107]. This ensures the generation of a high quality Chirp from this precision device.

To generate a linear Chirp, one needs to specify essential Chirp parameters consisting of f_{in}, f_f, Chirp duration T and Δf. According to the DDS theory [72] and figure 6.2, for a up-sweep Chirp, $f_{in} < f_f$, the output frequency can be expressed as:

$$f = f_{in} + n\Delta f \qquad n = 0, \cdots, N \tag{6.1}$$

where n is an integer number and $N = \frac{f_f - f_{in}}{\Delta f}$. A further necessary parameter for the DDS Chirp generation is the ramp rate N_r which determines the duration spent at each frequency. It can be expressed by:

$$N_r = \frac{f_s T}{N} - 1 \tag{6.2}$$

where f_s is the system clock frequency.

6.2.2 Wideband Sinusoidal Current Source

Most EIT systems use sinusoidal current source excitation. The performance of the current source significantly affects the accuracy of the measurements, and in turn on the constructed images. A concise review on the reported current sources has been presented in the second chapter of this thesis. Since the characteristics of the current sources reviewed are frequency dependent, they are not able to retain their required features over a wide frequency range, when a simultaneous excitation signal is applied. Therefore, they can not be exploited for the WEIT systems. In this case, the variation of load impedance over a wide frequency range is a further reason that the design of the wideband current source is more challenging than that of the conventional EIT.

Among the reported current sources the monolithic VCCS such as the AD844 [80] provides wider bandwidth and thus, the possibility of working with a simultaneous excitation signal. The other advantages of using these type of amplifiers are reduction in the electronic circuitry, stability over frequency and load range, and also avoiding component mismatching. The limitation in the maximum output current is a drawback of this type of current source. To overcome this, a parallel arrangement of current sources may be deployed to achieve a composite higher output current source, for instance in [64], but at the expense of lower total output impedance.

For the implementation of the current source in this research an LT1228 amplifier [130] was utilised. This is a 100 MHz current feedback amplifier, which includes a very fast transconductance amplifier. This amplifier can be externally

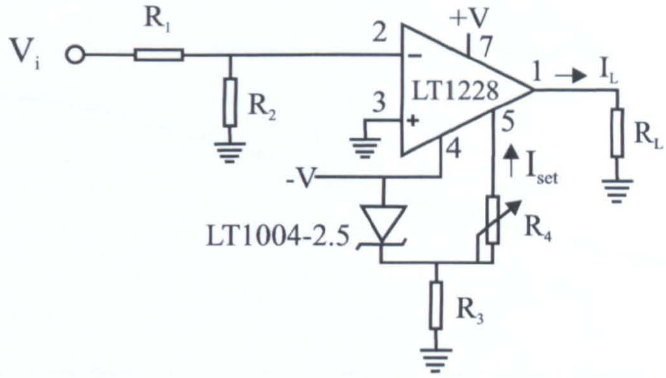

Figure 6.3: Schematic of current source using LT1228.

controlled by adjusting the reference current I_{set}, as shown in figure 6.3. It has also a wide output voltage range and, thereby, the capability to handle a wide range of output load. LT1228 has two main advantages in comparison with AD844. Firstly, a wider range of output load and secondly, the possibility of programming the output current without increasing the input voltage.

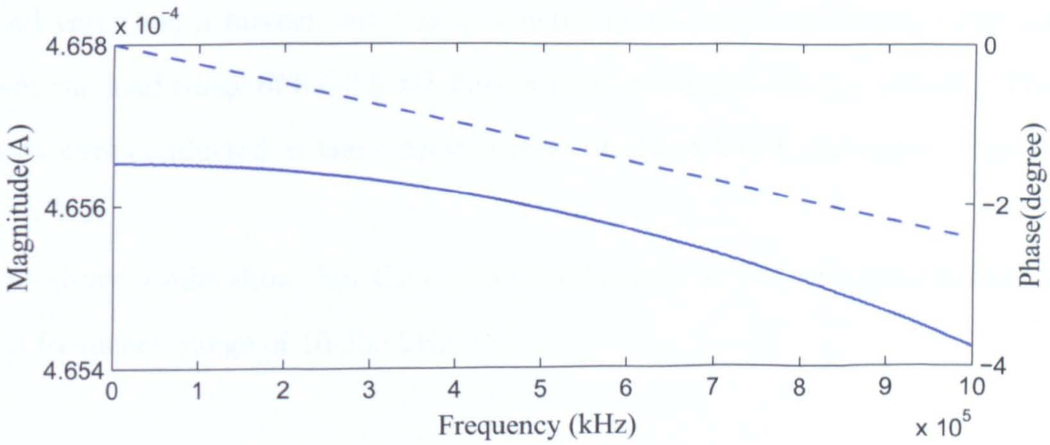

Figure 6.4: Current source AC analysis, magnitude (solid line) and phase (dashed line) .

Figure 6.4 shows the Spice AC analysis of the current source shown in figure 6.3. These results show a flat output current magnitude and phase change of 2.4(degree) over the bandwidth of 1 MHz. The simulation indicates that the maximum output impedance is 1.064 MΩ at a very low frequency value which declines to 400 kΩ at 1 MHz, as shown in figure 6.5.

In practice, however, the output impedance is less than these values. The practical tests over the frequency range of 10-200 kHz show the variation of the output

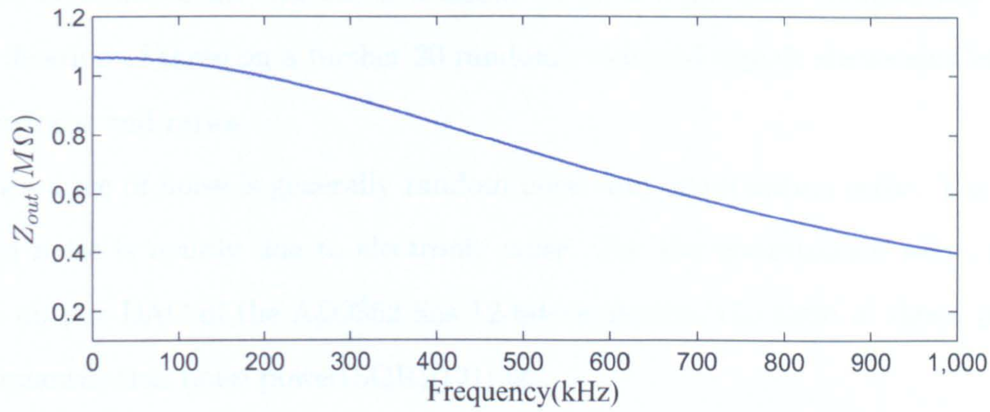

Figure 6.5: Output Impedance Z_{out}.

impedance from 286 kΩ at 10 kHz to 280 kΩ at 200 kHz. However, after this range the impedance gradually decreased to 20 kΩ at frequency 500 kHz. In the range of 10-200 kHz, the current indicated a relative change of 0.7% when the output load R_L was 1 kΩ. To see the stability of the current source with the load variation, a further test was conducted at frequency of 50 kHz. The tests over the load range of 0.1-3.5 kΩ show a realtive current change of 1.4%. These tests were conducted at the output current of about 5 mA and power supply of $\pm$15 Volt.

The above results show that the current source delivers its best performance over the frequency range of 10-200 kHz.

6.2.3 Noise Performance

The noise performance of the single-channel EIT system is evaluated by using Fourier analysis. Figure 6.6 presents the spectrum of an excitation Chirp and measured voltage in an experiment with the EIT rig, as illustrated later in this chapter. This is swept from 10 kHz to 210 kHz in a period of 5 ms. This figure shows the bandwidth occupied by the fundamental Chirp and the apparent disturbances. The figure implies that the disturbances consist of random noise and non-linear effects. The fundamental Chirp occupies the bandwidth 10-210 kHz. For this example, the power ratio of the fundamental signal to the non-linear part, is about 30 dB whereas it is about 40 dB for the noise components. The verification of these on a further 20 randomly selected signals shows similar disturbances and ratios.

The source of noise is generally random noise and quantization error. The random noise is mainly due to electronic noise. For the quantization noise, since the output DAC of the AD9852 has 12-bit resolution, the ratio of signal power to quantization noise power(SQR)[131] is:

$$SQR = 1.76 + 6.02B \ = 74 \ (dB) \tag{6.3}$$

where B is the DAC resolution.

Since all signals were recorded by the digital oscilloscope which has 8-bit resolution, then according to equation (6.3), this limits the SQR to about 49.92 dB. Comparing these theoretical values with the mentioned SNR of the practical data sets, implies the impact of quantization error on the total SNR of the system. This suggests that the implementation of a sophisticated measuring system with 12-bit ADC, for instance, would result in significant improvement in the overall SNR. It is also evident that since the non-linear disturbance has greater power ratio than that of the noise, it is a limiting factor in the implemented hardware. Here, again it must be emphasised that, due to the bandpass filtering of the wavelet transform the non-linear effects and also noise will be efficiently rejected by the proposed method.

Further investigation of the performance of the implemented hardware was carried out by the evaluation of the harmonic components in the current waveform applied to the rig at 50 kHz. As a measure of this, the total harmonic distortion (THD) method was exploited. This is expressed by:

$$THD(\%) = \frac{\sqrt{I_2^2 + I_3^2 + \cdots + I_n^2}}{I_f} \tag{6.4}$$

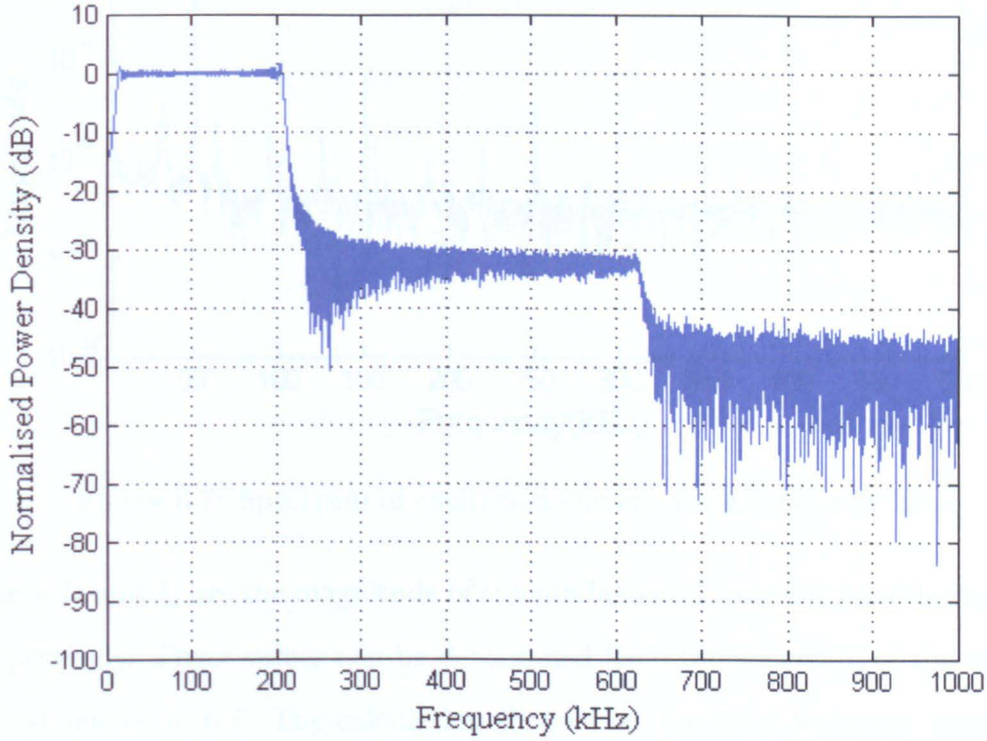

(a)

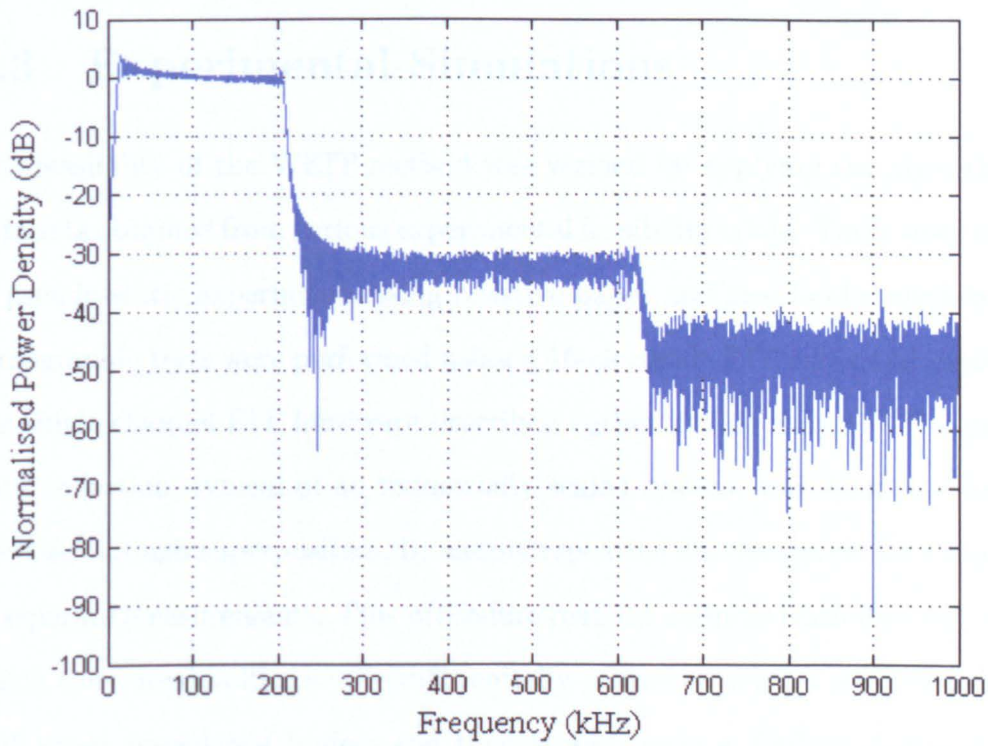

(b)

Figure 6.6: Spectrum of excitation current (a) and measured voltage (b), when the Chirp swept 10 kHz-210 kHz in period of $T = 5ms$.

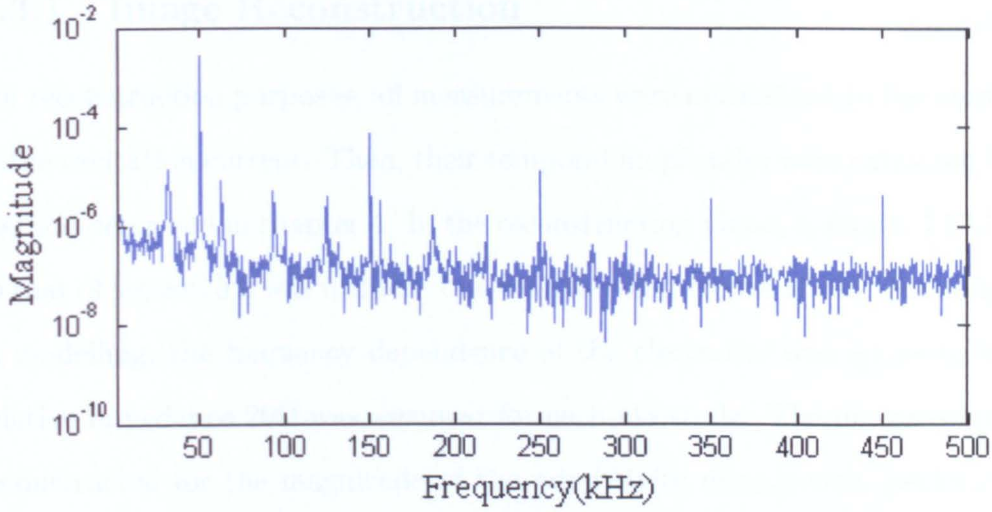

Figure 6.7: Spectrum of excitation current waveform at 50 kHz.

where I_f and I_n are the magnitude of the fundamental frequency and harmonics, respectively. These values can be determined from the spectrum of the current signal, shown in 6.7. The calculation shows that the total harmonic distortion for this example is, $THD = 2.9(\%)$.

6.3 Experimental Simulations

The feasibility of the WEIT method was verified by applying the algorithm on data sets obtained from various experimental feasibility trials. These tests consist of pseudo-static experiments using resistive paper and also food materials. The tomographic tests were performed using a 16-electrode EIT array and exploiting the single-channel EIT hardware described earlier in this chapter. The parallel data collection, typical of an industrially scaled system, was simulated for this exercise through superposition, by simply repeating the excitation for a sequence of separate measurements. This procedure realised a simple feasibility test-bed in which the sensed voltages were differentially measured using a purpose-designed high-input impedance buffer, and then stored using a LeCroy digital storage oscilloscope.

6.3.1 Image Reconstruction

For reconstruction purposes, all measurements were normalized to the amplitude of the excitation current. Then, their temporal amplitudes were extracted by the method described in chapter 4. In the reconstruction phase, a similar FEM mesh to that of section 5.5 was utilized, but with the diameter of 15 cm. For simplicity in modelling, the frequency dependence of the electrodes was ignored, but the relative impedance 20Ω was assumed for each electrode. The images were then reconstructed for the magnitude of the admittivity distribution, performed by five iterations of the nonlinear regularized Gauss-Newton method described in Chapter 2. The regularization factor was selected by inspection. In practice, to produce informative tomographic images, in the absence of information of the absolute values of admittivity, a difference image with respect to a reference may be deployed, as shown in figure 6.8.

As described in Chapter 2, for multi-frequency imaging the image at a certain frequency can be utilised as a reference. Therefore, objects which exhibit frequency-dependent behaviour will appear in the tomographic images. A second approach is reconstructing the final image with respect to the homogeneous medium. This consists of a simple two stage process. The images of the homogeneous medium, and then the medium complete with the non-homogeneous objects, were separately reconstructed at desired frequencies. To produce the final images they are then subtracted. Compared to the first method, this retains the structural information. However, its drawback is that the experiments must be initially conducted on the homogeneous medium, which may not be possible in many applications. Thus, in practical applications the first method may be preferable. Both methods efficiently reduce the effect of systematic errors [132], but since these errors have a frequency-dependent nature, the second approach appears to be more efficient.

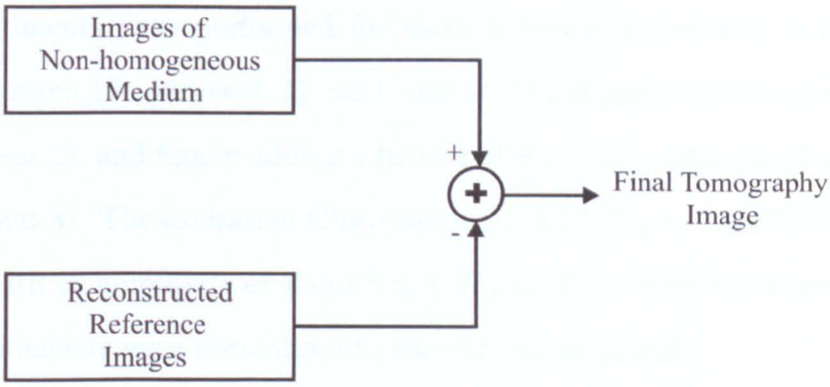

Figure 6.8: Reconstructing final tomography images at each frequency.

6.3.2 Experiments Using Resistive Paper

Resistive paper, or so called Teledeltos paper [133] facilitates clean and stable experiments for EIT studies. Since the excitation current flows in the 2-D surface, compared to the 2-D EIT rig it provides a more consistent and realistic 2-D phantom for the research investigation. However, from manufacturer data, the sheet resistance, ρ_s, is 2000 $\Omega/\Box$, but initial tests on similar samples of the paper indicate that sheet resistance varies between different samples of the paper roll. To create a 2-D resistive paper phantom, a cut-out circular piece of this paper was used. To then create frequency-dependent regions, non-homogeneous objects made with capacitors were appropriately fitted on it, as shown in figure 6.9.

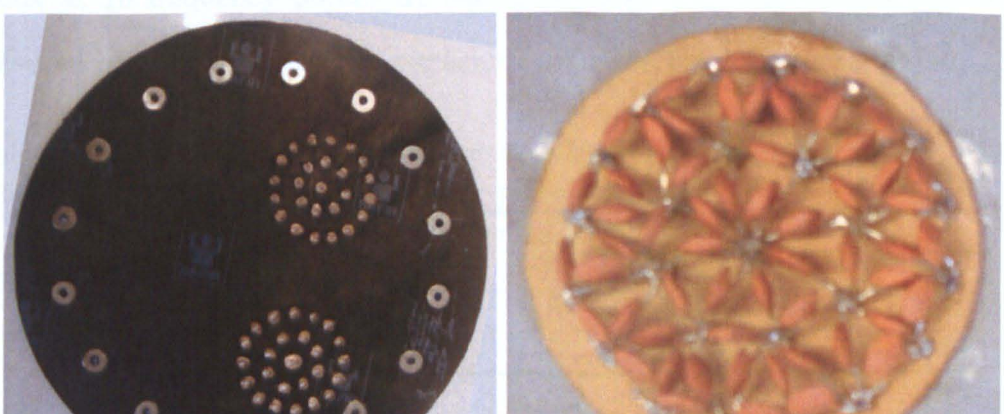

Figure 6.9: Resistive paper and inclusions: the resistive paper and two inclusions created using capacitances(left) and one of the inclusions attached to the back of resistive paper(right).

The experiments were performed for three scenarios consisting of a homogeneous phantom (Experiment 1), with one inclusion made of 10 nF capacitors (Experiment 2); and finally adding a further object made with 2.2 nF capacitors (Experiment 3). The excitation Chirp swept from 10 kHz to 210 kHz in a period of 5 ms, with an amplitude of about 5 mA. Figure 6.10 shows a measured Chirp. All measurements were normalised to the current amplitude.

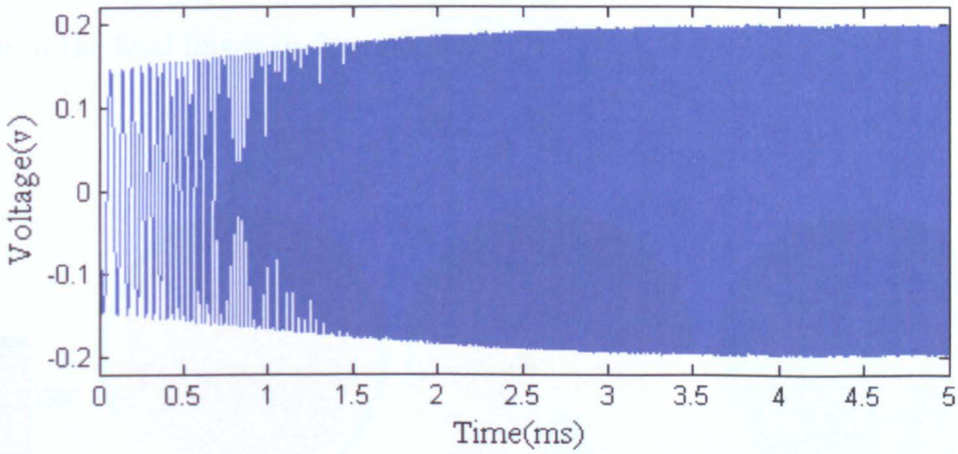

Figure 6.10: A measured Chirp, T=5 ms.

The measured data sets were analysed by using the proposed method. For this, the optimum wavelet parameters for the above Chirp were calculated. The results at 10 frequency points are shown in table 6.1. The magnitude of the measured data sets were then extracted. In the image reconstruction, there

Table 6.1: The wavelet parameters for the Chirp sweeping from 10 to 210 kHz with duration T=5 ms at 10 frequency points.

Wavelet parameters	Frequency(kHz)									
	20	40	60	80	100	120	140	160	180	200
f_c	0.7	0.7	0.7	0.7	0.8	0.7	1	0.7	0.8	0.8
f_b	0.7	0.9	1	0.9	0.7	0.9	0.4	0.8	0.6	0.6

was no significant change after 5 iterations, and the iteration was terminated at this point. The regularisation parameter was set to ($\alpha = 5 \times 10^{-4}$). Figure 6.11 shows the reconstructed images at each stage and the final images at frequencies 20 kHz and 200 kHz, for the Experiment 3. The colour bar shows the resistivity scale. The left and middle images of figure 6.11 indicate the absolute resistivity distribution, whereas the right image depicts the final image that give the resistivity changes with respect to the homogeneous paper. The negative sign in the colour bar implies the reduction of resistivity in comparison with the initial state. Comparing these images indicates that the subtraction results in a significant improvement in the elimination of the artefacts. For instance, at 200 kHz the objects are not visible in figure 6.11b, whereas they can be clearly seen in the final image in figure 6.11c.

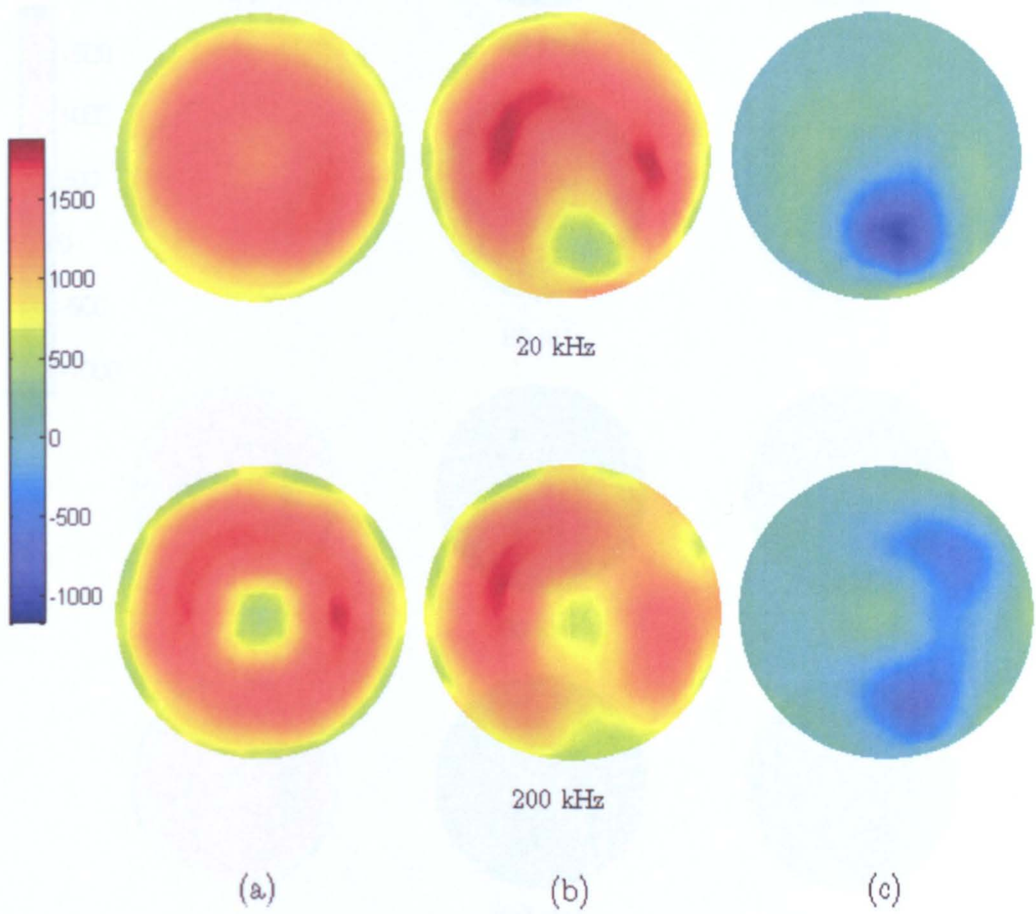

Figure 6.11: Reconstructed images for the resistive paper shown in figure 6.9: before including the inclusions(a), after including inclusions (b) and final image by subtraction(c); the colourbar shows the resistivity in Ω.

Figure 6.12 and 6.13 show the reconstructed images for the experiments described above at 10 frequency points from 20 kHz to 200 kHz.

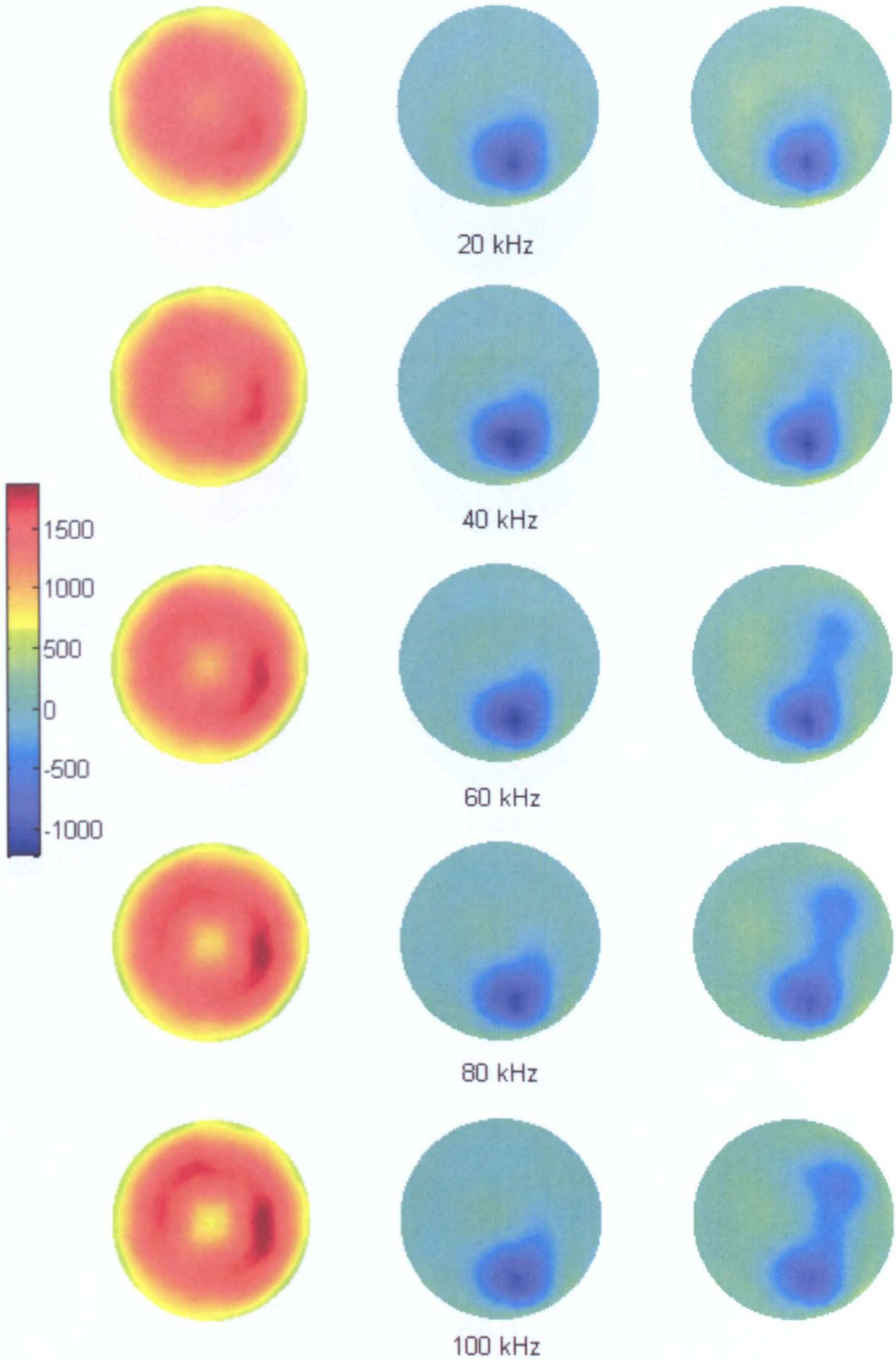

(a) (b) (c)

Figure 6.12: Reconstructed images for the resistive paper shown in figure 6.9 at frequencies from 20 kHz to 100 kHz: absolute resistivity image for Experiment 1 (a), final images for Experiment 2 (b), and Experiment 3 (c), the colourbar shows the resistivity in Ω.

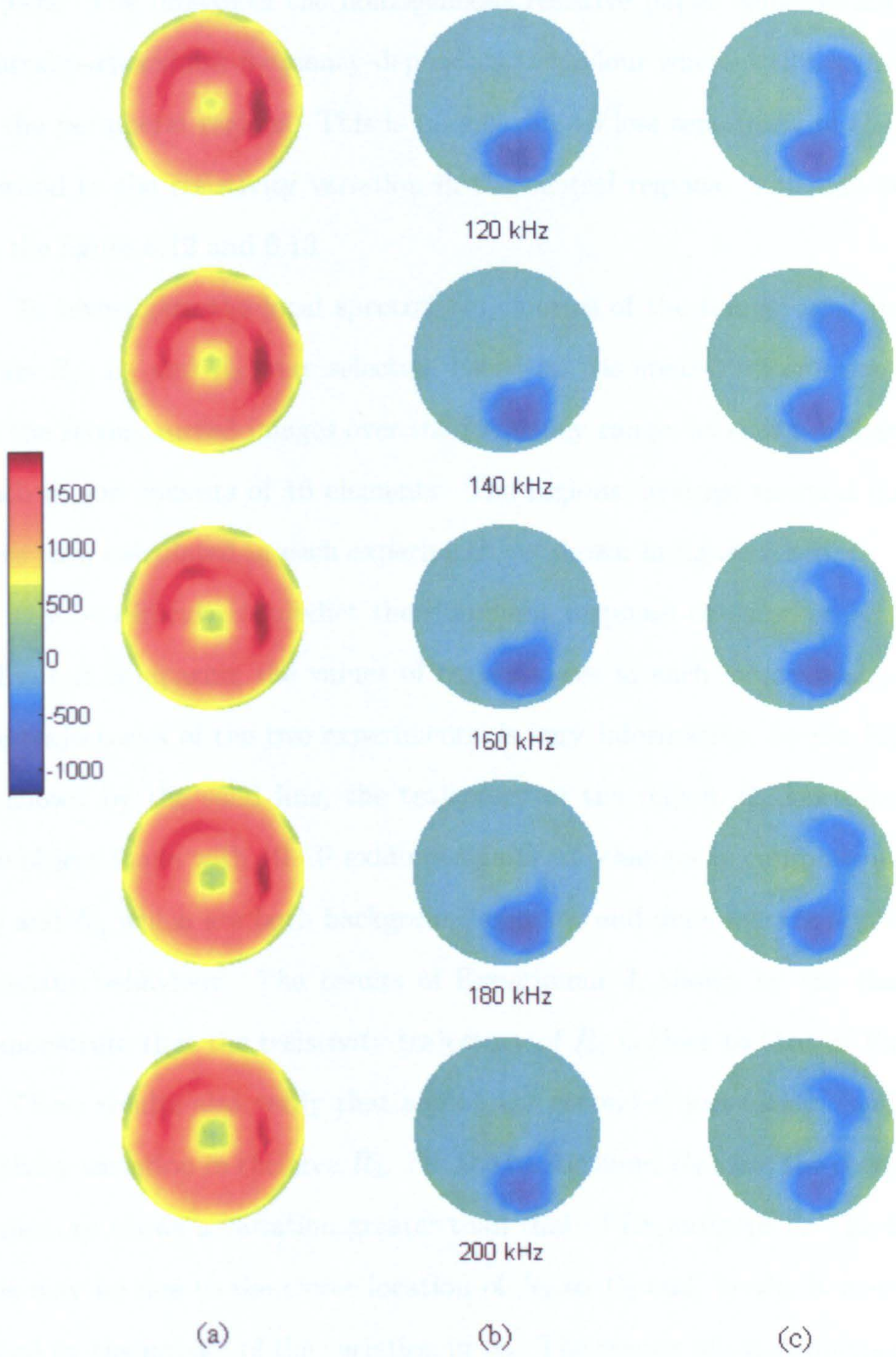

Figure 6.13: The continue of figure 6.12 for the frequencies from 120 kHz to 200 kHz

Comparing the final images with figure 6.9 verifies that the tomography images show the location of the objects correctly. The images also clearly exhibit the resistivity variation with frequency in the location of the non-homogeneous objects. The images of the homogeneous resistive paper demonstrate that the central parts exhibit frequency-dependent behaviour whereas this is insignificant in the peripheral regions. This is mainly due to less sensitivity of the adjacent method to the resistivity variation in the central regions. This can be verified on the figure 6.12 and 6.13.

To investigate the local spectral trajectories of the tomography images, regions R_1, R_2 and R_3 were selected, based on the spatial information provided by the reconstructed images over the frequency range, as shown in figure 6.14a. Each region consists of 16 elements. The regions' average spectral trajectories were then calculated in each experiment, as shown in figure 6.14b.

It may be difficult to predict the dominant response of these objects analytically, but comparing the values of capacitances in each experiments, and also the trajectories of the two experiments, is very informative. In the Experiment 2, shown by the solid line, the trajectory of the region R_1, corresponding to the object made with 10 nF exhibits significant changes in comparison with the R_2 and R_3 which are both background regions, and demonstrate approximately constant behaviour. The results of Experiment 3, shown by the dashed line, demonstrate that the resistivity trajectory of R_1 is close to that of Experiment 2. These results also verify that adding the second object causes significant resistivity variation in the area R_2. For the background R_3 case, the corresponding trajectory shows a variation greater than that of Experiment 2. The reason for this may be due to the closer location of R_3 to R_2 and, hence, it may be influenced by the impact of the variation in R_2. The results of experiments also show significant difference in the trend and values of the trajectories of the regions R_1 and R_2 due to the difference of the corresponding capacitors.

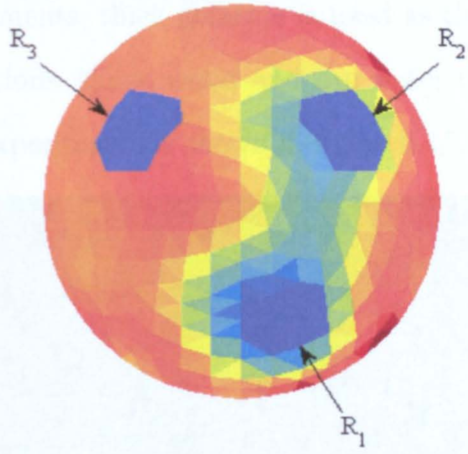

(a)

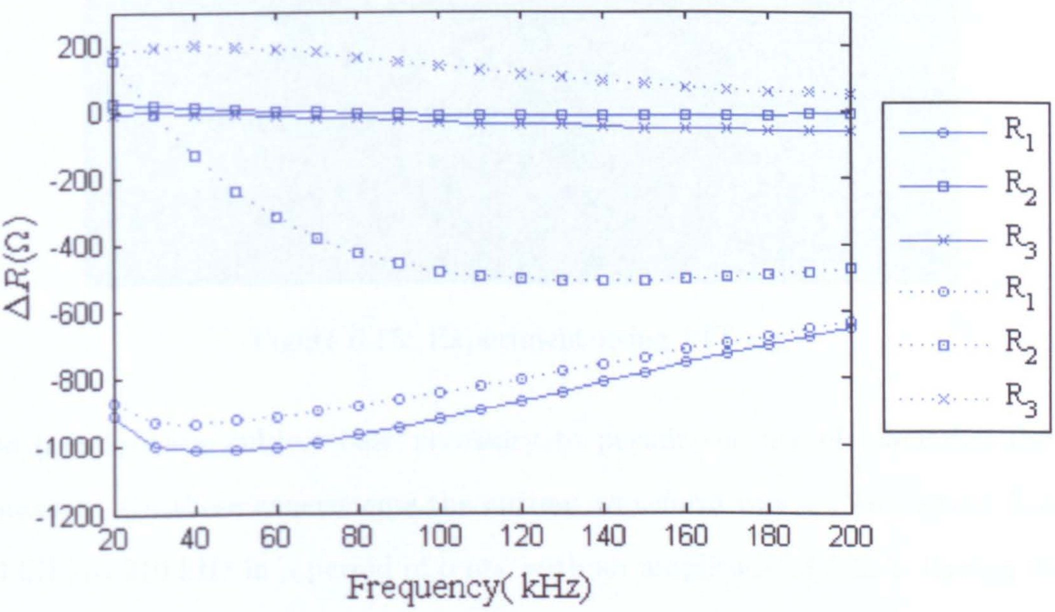

(b)

Figure 6.14: Local averaged trajectories: selected regions on images (a) and the variation of resistivity trajectories of R_1 in the location of object made with 10 nF, R_2 in the location of object made with 2.2 nF and R_3 background (b), where the solid and dashed lines are corresponding to the experiment 2 and 3, respectively.

6.3.3 Experiments Using the EIT Rig

Further investigations on the feasibility of the proposed method were carried out by performing a set of experiments using a 16-electrode EIT rig using food materials. In these experiments, thick gelatine is used as the background medium with common fruit sections, saline water and tap water used as inclusions. The arrangement of these experiments is shown in figure 6.15. The gelatine provided

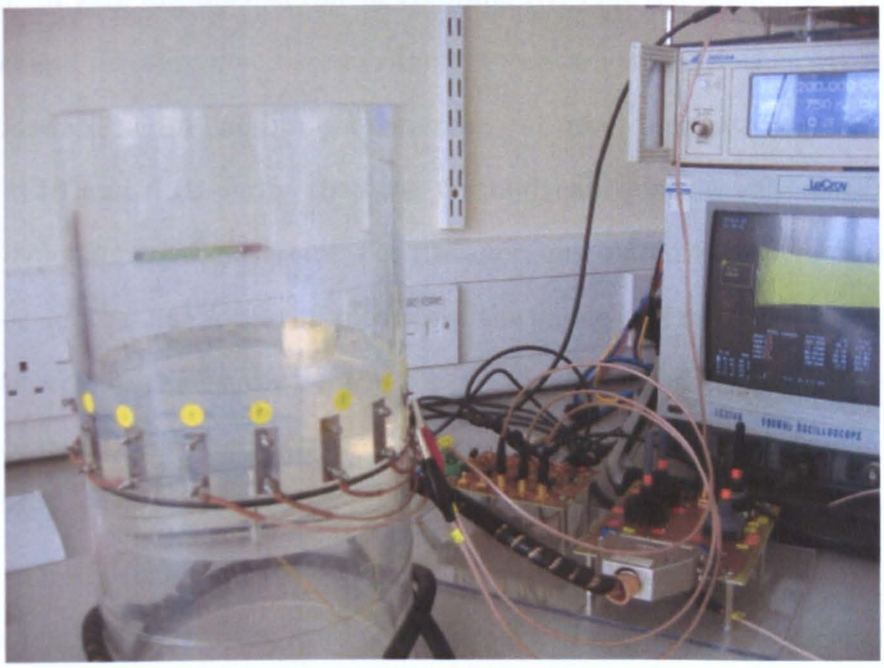

Figure 6.15: Experiment using EIT rig.

the pseudo-static subject base necessary to permit the use of sequential data collection. In these experiments the current waveform was a Chirp swept from 10 kHz to 210 kHz in a period of 5 ms, with an amplitude of 5 mA. During the experiments the temperature in the laboratory was maintained at 25±2 °C.

In these tests, the measurements were first performed on the homogeneous medium containing thick gelatine. Figure 6.16 shows the reconstructed resistivity distributions at two frequencies. According to these images, the homogeneous medium appears to have a small frequency-dependent characteristic.

Experiments were then carried out with the non-homogeneous objects. The final images were produced, as described previously in this chapter, and the regularisation parameter was set to ($\alpha = 3 \times 10^{-4}$). Figure 6.17 show (a) the location of the fruits and pool of tap water, and (b) the reconstructed image at frequency 100 kHz. Further images from 20 kHz to 200 kHz are shown in figure 6.18a and 6.19a.

The experiment was also conducted using saline in place of tap water, under the same conditions as the first set of experiments. Resulting tomographic images are shown in figures 6.18c and 6.19c. The difference images in respect to the image at 20 kHz are also shown in columns (b) and (d) of figure 6.18. Since the wideband measurements are available, reconstruction at other frequencies is straightforward and no additional experimental procedures are required.

Figures 6.18 and 6.19 verify that the method can qualitatively show the frequency dependence of materials. For instance, in comparison with the complex cucumber and banana foodstuff materials, the saline and tap water demonstrate less sensitivity to the excitation frequency. The figures also show differences in frequency dependence between the cucumber and banana materials over the frequency range. Hence where such characteristics are known the method could be used to identify materials.

As a further assessment from the above experiments the averaged trajectories of the local spectrum resistivity changes, $\Delta R(\Omega)$ of four regions, as shown in

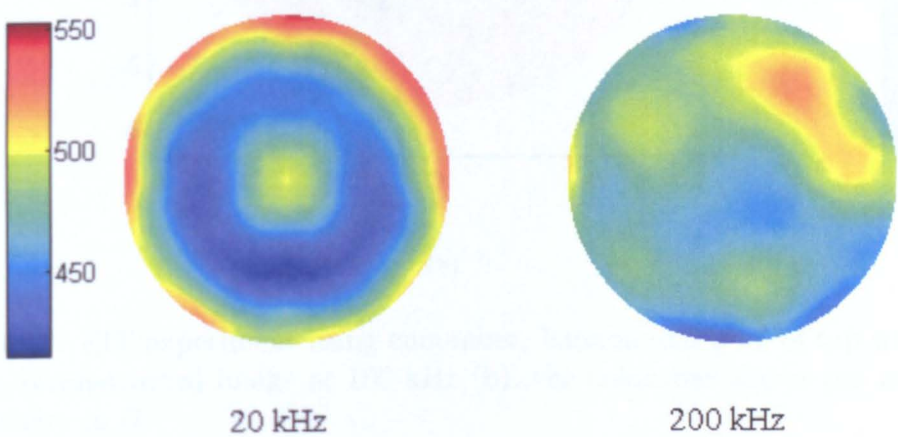

Figure 6.16: Tomography images at frequencies 20 kHz (left) and 200 kHz (right) when the EIT rig was containing thick gelatine, the colour bar shows the resistivity scale in Ω.

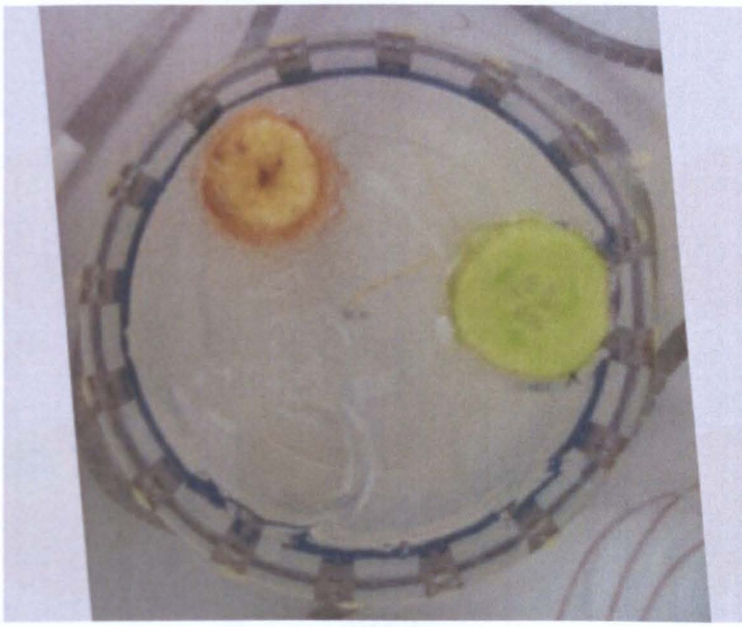

(a)

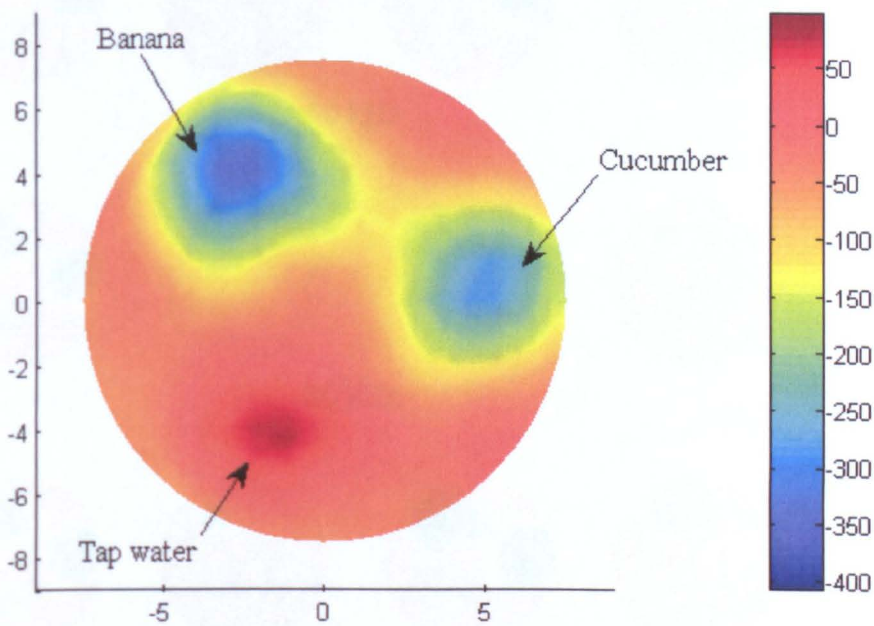

(b)

Figure 6.17: EIT experiment using cucumber, banana and pool of tap water (a) and the reconstructed image at 100 kHz (b), the colourbar shows the variation of resistivity in Ω.

figure 6.20a, (corresponding to the two fruit sections, pool of saline or tap water and the background gelatine) were calculated by using the tomographic data provided by the difference images. Each selected region on the tomography images

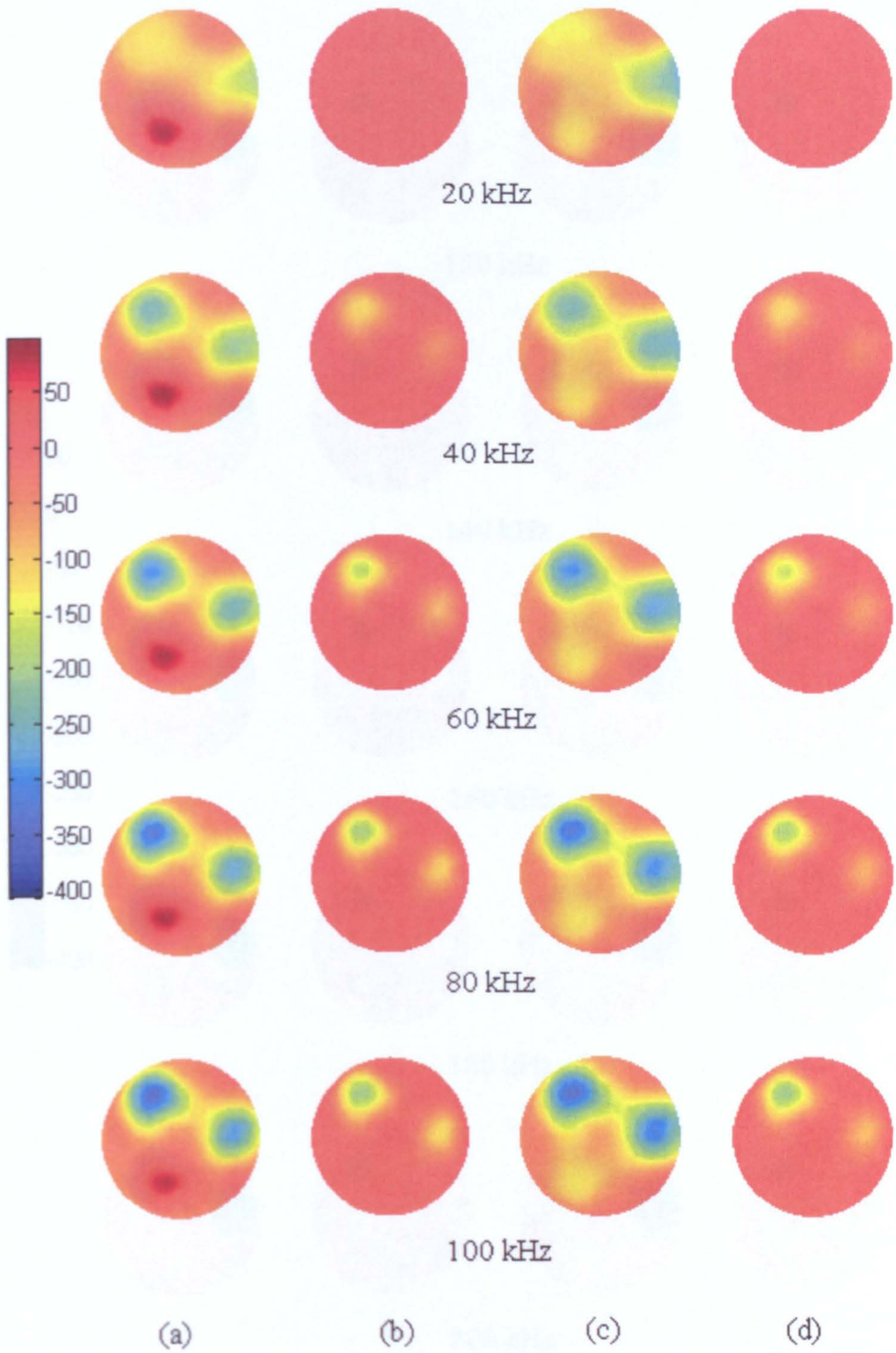

Figure 6.18: Images resulted from subtraction of homogeneous and non-homogeneous using cucumber, banana and tap water at frequencies from 20 kHz to 100 kHz (a) and their difference images in respect to images at 20 kHz (b), images resulted from subtraction of homogeneous and non-homogeneous using cucumber, banana and saline (c) and their difference images in respect to images at 20 kHz(d), the colourbar shows the variation of resistivity in Ω.

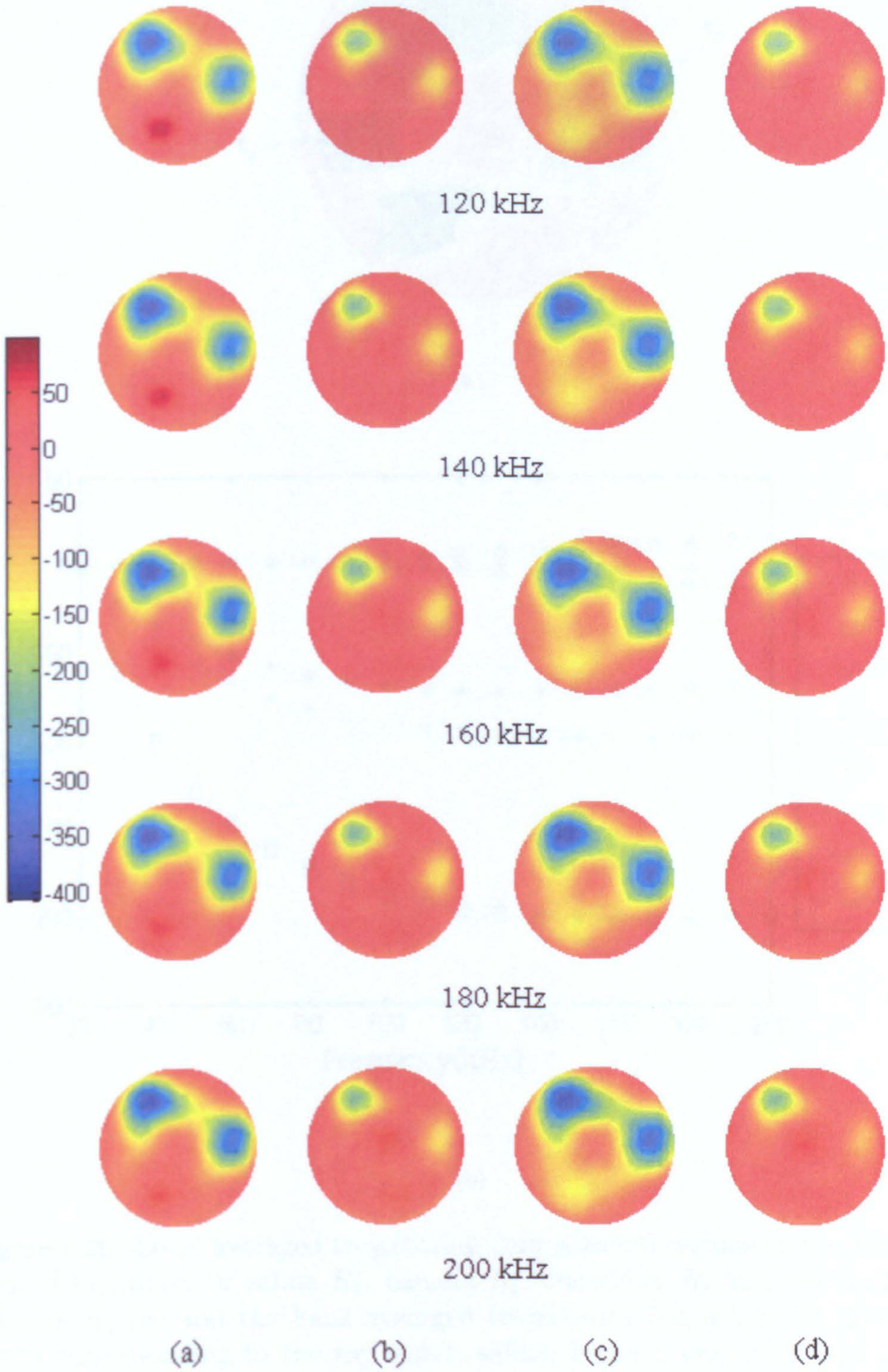

Figure 6.19: The continue of figure 6.18 for the frequencies from 120 kHz to 200 kHz

consisted of 16 elements. Figure 6.20b demonstrates that the materials in the

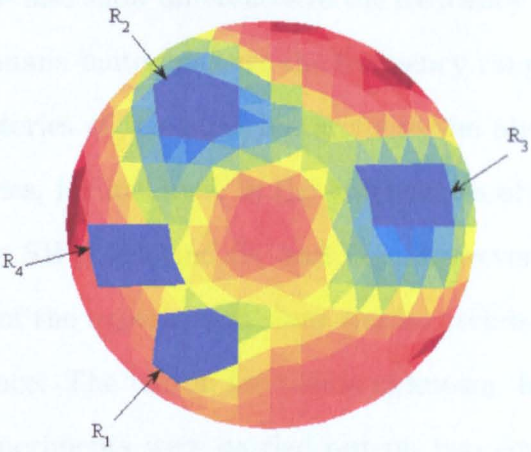

(a)

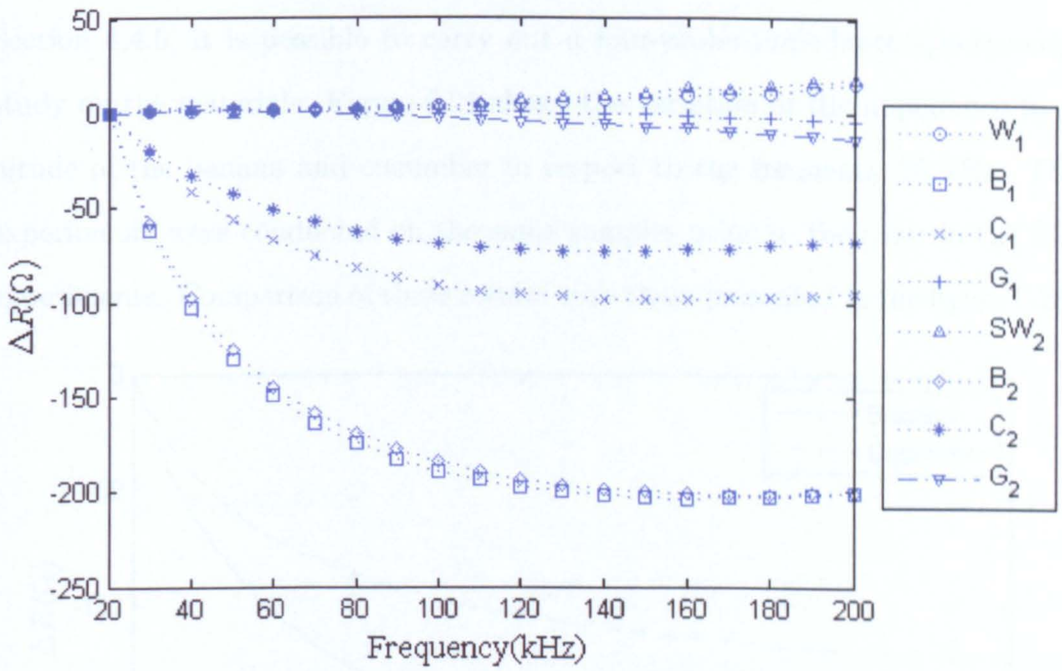

(b)

Figure 6.20: Local averaged trajectories: four selected regions at the location of pool of tap water or saline R_1, banana R_2, cucumber R_3 and the background gelatine R_4 (a) and the local averaged trajectories (b), where W, SW, B, C, G are corresponding to the tap water, saline, banana, cucumber and gelatine, respectively, and subscripts 1 and 2 are corresponding to the two experiments.

above experiments exhibits different trajectories over the frequency range. For instance, when compared to the complex cucumber and banana foodstuff materials, the saline and tap water materials demonstrate less sensitivity to excitation frequency. The figures also show differences in the frequency dependence between the cucumber and banana materials over the frequency range. Furthermore, the comparison of trajectories of the same materials in the above two experiments shows close trajectories, for instance, in the trajectories of banana, B_1 and B_2, tap water W_1, saline SW_2, gelatine G_1 and G_2. However, for the cucumber, although the results of the experiments show similar trends, the trajectories exhibits greater difference. The reason for this is unknown, but a possible reason is that the above experiments were carried out on two consequence days and, consequently, the quality of the materials may have changed.

As mentioned in the Chapter 4, by utilising the algorithm presented in the Section 4.4.5, it is possible to carry out a four-probe impedance spectroscopy study on the materials. Figure 6.21 shows the variation of the impedance magnitude of the banana and cucumber in respect to the frequency 20 kHz. This experiments were conducted on the same samples prior to their use in the EIT experiments. Comparison of these results with those presented in the figure 6.20b

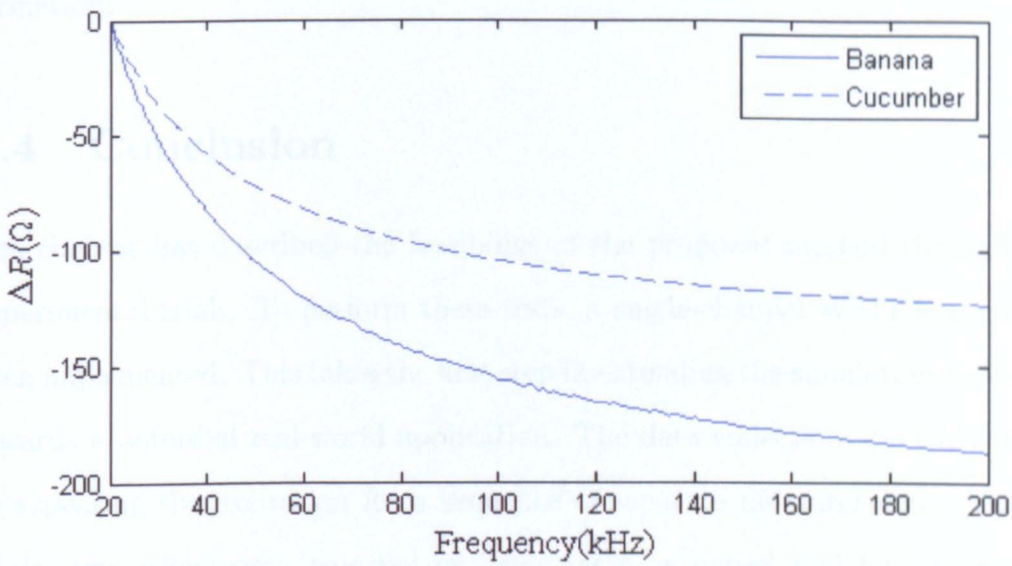

Figure 6.21: Impedance variation of banana and cucumber samples in respect to the frequency 20 kHz.

indicates that, although the results are quantitively different, in general they are in good agreement. They indicate that the trends of the two experiments are similar, and also that in both tests the overall impedance change of the banana is greater than that of cucumber. The differences in the above experiments, for instance for cucumber, may be influenced by various reasons including the variation of the sample quality with time, the performance of hardware, the reconstruction algorithm and the regularisation factor.

These issues have been investigated in the literature. For instance, the implications of the performance of EIT hardware is investigated in [134], and also the impact of reconstruction algorithms and their parameters have been studied in [135, 125]. In the experiments conducted for this research, it is evident that the implementation of a complete parallel WEIT system will decrease the errors, for instance, due to experiment duration, systematic errors, and noise. These improvements will enhance the accuracy of measurements and, thereby, lead to more accurate tomography information. Further investigations are also required regarding the impact of the reconstruction procedure and regularisation factor on the material spectral characterisation obtained by using the tomographic information.

6.4 Conclusion

The chapter has described the feasibility of the proposed method through the experimental trials. To perform these tests, a single-channel WEIT system has been implemented. This takes the first step in extending the simulation approach towards a potential real-world application. The data collection was carried out by repeating the excitation for a sequence of separate measurements. Various static simulations were reported by using resistive paper, and food materials. The quantitive and qualitative results verify the promise of the new method in exploiting sensitivity to variations over the frequency range. They indicate that the described method can support spectroscopic analysis of the process materials. The results presented in the chapter also support the conclusion that utilising

Chirp excitation efficiently facilitates tomographic measurement over a desired frequency range, although this is achieved at the minor cost of extra processing complexity, and a slightly increased average error. The results also encourage the development of a truly parallel data acquisition system. This could be deployed to perform further investigations on more realistic dynamic subjects.

Chapter 7

Conclusions and Future Work

7.1 Conclusions

In this thesis brief overview of general EIT technique has been given in Chapter 2. This included EIT modelling, image reconstruction and hardware. The reminder of the thesis concerns the new development of WEIT. In Chapter 3 an comprehensive review of the potential excitation signals in WEIT system is provided. Chapter 4 deals with the algorithms designed to extract required values from Chirp signals, in order to perform image reconstruction. In Chapter 5 a simulation study of the proposed WEIT method has been presented by exploiting the Chirp as an excitation signal. In Chapter 6 the feasibility of the novel method has been demonstrated by utilising practical experiments. In conclusion, the primary contributions carried out in this research thesis are summarised in the following sections:

- **Excitation signals for MFEIT**

  In a WEIT system the choice of the excitation signal is very important. Excitation in MFEIT has been reviewed with a focus on the key signal factors. These have been classified into two forms consisting of discrete sequential form, and the simultaneous form. A group of signal candidates, appropriate for use in MFEIT, has been considered including: Pulse, Sinc, PRBS, and Chirp. Their dynamic application characteristics are assessed using a simple RC network simulation to challenge their real-time limitations. In a specific application several signal forms may be useful, but it is likely that there will be an optimal selection that enhances spectral information. It has been concluded that exploiting the Chirp signal is superior to other wide band signals. This signal offers advantages for the WEIT systems, which target the most demanding real-time applications that exhibit broad spectral characteristics. In particular, this sophisticated signal form delivers the requisite measurement speed while providing major flexibility to tailor the measurement duration, bandwidth and frequency resolution. In conclusion the Chapter presents a coherent analysis of wide band excitation signals to aid research, design and development in wide band systems that in turn aim to probe deeper application structure and function through EIT measurement.

- **Chirp signal analysis**

In this research, the Chirp signal has been selected as the appropriate wideband signal for the WEIT system. Based upon this, Chapter 4 has demonstrated the algorithms developed in order to determine the required values from the Chirp signal, in order to perform image reconstruction. For this purpose, STFT and CWT were examined. The simulation results have indicated that an algorithm based on the CWT provides better accuracy for the extracted temporal amplitude and phase of simulated Chirp waveforms. This algorithm is developed based on the ridge phenomenon [116, 108] and using the CWT. It has been demonstrated that accurate extraction of the temporal values is dependent upon the characteristics of the Chirp signal, and the wavelet parameters utilised. For this, based on the conditions stated by Mallat in [108], the appropriate constraints have been derived. By using this and also by the determination of the optimum wavelet parameters, the algorithm for the accurate estimation of temporal values has been designed. The results in this chapter demonstrate the precise estimation of the temporal values, but they also show there is an absolute relative error between analytical and estimated values.

- **WEIT simulation study**

Chapter 5 presents a novel method for WEIT using Chirp excitation based on the wavelet analysis. Aspects of the new method have been investigated by various simulations performed on synthetic data sets. These data sets were generated by using an appropriate 2D mesh model. The reconstructed tomography images of the true complex admittivity distribution at the discrete frequency points, shows that the proposed method is able to estimate the local spectral admittivity information. The error analysis demonstrates the propagation of the generated errors from the wavelet algorithm, into the tomographic images. The simulations, however, indicate that these minor errors in the tomographic data are tolerable and offset by the corresponding gain of process spectral information. The noise study also reveals the robustness of the method deployed in the presence of noise, and indicates a significant improvement in the noise performance. In conclusion, the results verify that deploying Chirp excitation facilitates tomographic measurement over a desired frequency range, but with the minor cost of extra processing complexity and error. It can also be concluded that WEIT is able to simultaneously reveal local spectral characteristics and structural information which, in turn, can enhance the identification of process materials or in the estimation of process parameters.

- **Experimental feasibility study**

The thesis demonstrates the feasibility of the proposed method by using real measurements. For this purpose, single-channel EIT system has been implemented. This has revealed that the synthesis of the Chirp signal can be efficiently achieved by deploying available high performance DDS devices [107]. The most challenging part of the WEIT system, however, appears to be the wideband current source that would provide the stable current over the desired bandwidth.

Practical data sets have been collected in various simple static experimental scenarios created using resistive paper, and an EIT rig containing food materials. These feasibility study results demonstrate the promise of the proposed composite approach in exploiting variations of local admittivity with frequency. They indicate that the described method can support spectroscopic analysis of the process materials. Results in the chapter also support the conclusion that utilising chirp excitation efficiently facilitates tomographic measurement over a desired frequency range. Finally, it must be stressed that since the simple tests conducted are the first step towards a real-world application, further investigation on an actual process should be carried out, preceded with the development of a complete parallel data acquisition system.

7.2 Future Work

The thesis has demonstrated various aspects of the novel WEIT system that exploits the Chirp as an excitation signal. The research that has been carried out provides sufficient results to support reliable conclusion described above . However, the author acknowledges that due to time consideration, there are aspects of work could be further improved and continued. These aspects are listed as follow:

- **Implementation 3-D parallel WEIT system**

  In this thesis the experimental feasibility study has been conducted by implementing a single-channel EIT system. This has facilitated simple pseudo-static tests. However, to gain the advantages of the proposed WEIT to capture the spectral information in a practical dynamic process, it is necessary to implement a 3-D parallel WEIT system. This sophisticated system will then support trials on actual complex processes where the ability of the proposed method to operate within process dynamic can be thoroughly studied. To implement this system requires the use of fast data acquisition modules able to comply with sampling requirement in the limited measurement time duration available. The challenging part of implementing such a WEIT system would be in the development of the wide bandwidth current source. This must be retain stable and accurate performance over the wide range of load dynamics in industrial applications.

- **Validation of presented method in an actual process**

  In this research the practical verification of the proposed method has been presented by performing various simple trials on resistive paper and food materials. Since the these experiments were simple static trials for initial feasibility studies, there is a need to perform further more realistic experiments. For this it is necessary to exploit a complete 3-D parallel WEIT system mentioned in the previous section. After conducting appropriate calibration, the results may then be validated by comparing with those obtained by available commercial EIT system. These investigations can be associated with a priori information of the known spectral responses of the process or its materials.

- **Visualisation of spectro-tomographs**

  In this thesis, the spectral tomographic images have been presented using the simple conventional styles such as the separate demonstration of images at each discrete frequency point. This approach may give the basic information of local spectral admittivity over frequency range, but, instead, proposing an approach to fuse the spectral information into one spectral image can efficiently provide a more powerful visual perspective of the process spectral characteristics. To gain this insight it is necessary to do further work on the implemention an appropriate visualisation method for the integration of multi-frequency tomography images.

- **Feasibility study of new method for medical application**

  In section 5.2, it was mentioned that human tissues exhibits frequency-dependent properties [89] and that characterisation of human tissue, and also diagnosis of particular clinical conditions, using electrical properties has been of particular interest in the medical field[12, 11, 89]. Since the proposed method in this thesis is very flexible in terms of measurement duration and bandwidth, deploying it could improve the medical multi-frequency studies. In addition to these advantages, this would decrease the errors arising from dynamic issues such as patient movements. As described in Chapter 3, utilising the Chirp excitation also overcomes the drawback of the large peaks in the conventional composite or multi-sinusoidal forms that are undesirable due to the safety concerns [136] in medical application.

Appendix A

List of Publications

[1] M. Nahvi and B. S. Hoyle, "Process impedance spectroscopy through chirp waveform excitation," in *Proceedings of the 5th World Congress on Industrial Process Tomography*, Bergen, Norway, pp. 630-637, September 2007.

[2] M. Nahvi and B. S. Hoyle, " Wideband electrical impedance tomography simulation study," in *Proceedings of the 5th World Congress on Industrial Process Tomography*, Bergen, Norway, pp. 1030-1037, September 2007.

[3] M. Nahvi and B. S. Hoyle, "Wideband electrical impedance tomography," in *Journal of Measurement Science and Technology*, vol. 19, no. 9, p. 094011 (9pp), 2008.

[4] M. Nahvi and B. S. Hoyle, "Wideband Excitation Signals for Electrical Impedance Industrial Process Tomography," in *Proceedings of the 5th International Symposium on Process Tomography*, Zakopane, Poland, August 2008.

[5] Brian S. Hoyle and Manoochehr Nahvi "Spectro-Tomography - an Electrical Sensing Method for Integrated Estimation of Component Identification and Distribution Mapping in Industrial Process ," to be published in *Proceedings of the 7^{th} IEEE Conference on Sensors*, Lecce, Italy, pp. 807-810 , 2008.

References

[1] R. A. Williams and M. S. Beck, eds., *Process tomography principles , techniques and application.* Butterworth-Heinemann, 1995.

[2] B. S. Hoyle, X. Jia, F. J. W. Podd, H. I. Schlaberg, H. S. Tan, M. Wang, R. A. Williams, and T. A. York, "Design and application of a multimodal process tomography system," *Measurement Science and Technology,* vol. 12, no. 8, pp. 1157–1165, 2001.

[3] B. S. Hoyle, H. McCann, and D. M. Scott, *Process Tomography,* ch. 4, pp. 85–126. Process imaging for automatic control, Taylor & Francis,, 2005.

[4] F. Ricard, C. Brechtelsbauer, X. Y. Xu, and C. J. Lawrence, "Monitoring of multiphase pharmaceutical processes using electrical resistance tomography," *Chem. Eng. Res. Design,* vol. 83, pp. 794–805, 2005.

[5] S. J. Stanley, "Tomographic imaging during reactive precipitation: mixing with chemical reaction," *Chem. Eng. Res. Design,* vol. 61, pp. 7850–63, 2006.

[6] M. S. Beck, T. Dyakowski, and R. A. Williams, "Process tomography – the state of the art," *Transactions of the Institute of Measurement and Control,* vol. 20 (4), pp. 163–177, 1998.

[7] T. York, *Electrical tomography for industrial application,* ch. 5, pp. 295–334. Electrical impedance tomography: methods, history and applications, Institute of Physics Publications, 2005.

[8] S. C. Murphy, S. J. Stanley, D. Rhodes, and T. A. York, "Imaging of Solid-liquid Suspensions using Electrical Impedance Tomography (EIT)," in *Proceeding of 5th World Congress on Industrial Process Tomography, Bergen, Norway,* pp. 487–494, 2007.

[9] G. Vilar, R. A. Williams, M. Wang, and R. J. Tweedie, "Mathematical modelling of flow parameters in an oscillatory baffled reactor (obr)," in *Proceeding of 5th World Congress on Industrial Process Tomography, Bergen, Norway,* pp. 715–722, 2007.

[10] J. Y. Xu, M. Wang, B. Munir, H. I. Oluwadarey, H. I. Schlaberg, Y. X. Wu, and R. A. Williams, "Correlation of electromagnetic flow meter, electrical resistance tomography and mechanistic modelling for a new solution of solid slurry measurement," in *Proceeding of 5th World Congress on Industrial Process Tomography, Bergen, Norway,* pp. 1021–1029, 2007.

[11] H. Griffiths and J. Jossinet, "Bioelectrical spectroscopy from multi-frequency eit," *Physiol. Meas.*, vol. 15, no. 2A, pp. A59–A63, 1994.

[12] B. H. Brown, D. C. Barber, W. Wang, L. Lu, A. D. Leathard, R. H. Smallwood, A. R. Hampshire, R. Mackay, and K. Hatzigalanis, "Multi-frequency imaging and modelling of respiratory related electrical impedance changes," *Physiol. Meas.*, vol. 15, pp. A1–A12, 1994.

[13] R. J. Yerworth, R. H. Bayford, B. Brown, P. Milnes, M. Conway, and D. S. Holder, "Electrical impedance tomography spectroscopy (eits) for human head imaging," *Physiol. Meas.*, vol. 24, no. 2, pp. 477–489, 2003.

[14] E. J. W. Tong In Oh and D. Holder, "Multi-frequency eit system with radially symmetric architecture: Khu mark1," *Physiological Measurement*, vol. 28, no. 7, pp. S183–S196, 2007.

[15] T. Kerner, K. Paulsen, A. Hartov, S. Soho, and S. Poplack, "Electrical impedance spectroscopy of the breast: clinical imaging results in 26 subjects," *Medical Imaging, IEEE Transactions on*, vol. 21, no. 6, pp. 638–645, 2002.

[16] R. Halter, A. Hartov, and K. D. Paulsen, "Design and implementation of a high frequency electrical impedance tomography system," *Physiological Measurement*, vol. 25, no. 1, pp. 379–390, 2004.

[17] A. M. Denisov, *Elements of the theory of inverse problems.* Utrecht :: VSP,, 1999. Includes bibliographical references (p. [265]-272).

[18] P. C. Hansen, *Rank-deficient and discrete ill-posed problems.* Philadelphia: SIAM, 1998.

[19] H. W. Engl, *Regularization of inverse problems / by Heinz W. Engl, Martin Hanke, and Andreas Neubauer.* Dordrecht ; Boston :: Kluwer Academic Publishers,, c2000. Includes bibliographical references (p. 299-318) and index.

[20] M. Bertero, *Introduction to inverse problems in imaging.* Bristol :: Institute of Physics,, 1998.

[21] M. Cheney and D. Isaacson, "Issues in electrical impedance imaging," *Computational Science and Engineering, IEEE [see also Computing in Science & Engineering]*, vol. 2, no. 4, pp. 53–62, 1995.

[22] G. Saulnier, R. Blue, J. Newell, D. Isaacson, and P. Edic, "Electrical impedance tomography," *Signal Processing Magazine, IEEE*, vol. 18, no. 6, pp. 31–43, 2001.

[23] M. Vauhkonen, D. Vadsz, P. Karjalainen, E. Somersalo, and J. Kaipio, "Tikhonov regularization and prior information in elctrical impedance tomography," *IEEE Trans. on Medical Imaging*, vol. 17, no. 2, 1998.

[24] W. R. Breckon and M. K. Pidcock, "Mathematical aspects of impedance imaging," *Clinical Physics and Physiological Measurement*, vol. 8, no. 4A, pp. 77–84, 1987.

[25] K.-S. Cheng, D. Isaacson, J. Newell, and D. Gisser, "Electrode models for electric current computed tomography," *Biomedical Engineering, IEEE Transactions on*, vol. 36, no. 9, pp. 918–924, 1989.

[26] K. Paulson, W. Breckon, and M. Pidcock, "Electrode modelling in electrical impedance tomography," *SIAM Journal on Applied Mathematics*, vol. 52, no. 4, pp. 1012–1022, 1992.

[27] N. Ida, *Engineering electromagnetics*. New York ; London :: Springer,, 2nd ed. ed., c2004. Includes bibliographical references and index.

[28] . Lpez Dvalos, Arturo, *Fundamentals of electromagnetism : vacuum electrodynamics, media, and relativity / A. Lpez Dvalos, D. Zanette*. Berlin ; New York :: Springer,, 1999. Includes bibliographical references and index.

[29] A. J. Peyton, M. S. Beck, A. R. Borges, J. E. d. Oliveira, G. M. Lyon, Z. Z. Yu, M. W. Brown, and J. Ferrerra, "Development of electromagnetic tomography (emt) for industrial applications. part 1: Sensor design and instrumentation," in *Proceeding of 1st World Congress on Industrial Process Tomography, Buxton, Greater Manchester*, April 14-17, 1999.

[30] K. Paulson, W. Breckon, and M. Pidcock, "A hybrid phantom for electrical impedance tomography," *Clinical Physics and Physiological Measurement*, vol. 13, no. A, pp. 155–159, 1992.

[31] E. Somersalo, M. Cheney, and D. Isaacson, "Existence and uniqueness for electrode models for electric current computed tomography," *SIAM Journal on Applied Mathematics*, vol. 52, no. 4, pp. 1023–1040, 1992.

[32] M. Vauhkonen, *Electrical impedance tomography and prior information*. PhD thesis, Kuopio, 1997.

[33] J.-M. Jin, *The finite element method in electromagnetics*. New York ; Chichester :: Wiley,, 2nd ed. ed., 2002. Previous ed.: 1993.

[34] N. Polydorides, *Image reconstruction algorithms for soft field tomography*. PhD thesis, UK, 2002.

[35] P. J. Vauhkonen, *Image reconstruction in tree-dimentional electrical impedance tomography*. PhD thesis, University of Kuopio, Kuopio, 2004.

[36] D. S. Holder, ed., *Electrical impedance tomography : methods, history and applications*. Institute of Physics Pub.,, 2005.

[37] M. Vauhkonen, W. R. B. Lionheart, L. M. Heikkinen, P. J. Vauhkonen, and J. P. Kaipio, "A matlab package for the eidors project to reconstruct two-dimensional eit images," *Physiological Measurement*, vol. 22, no. 1, pp. 107–111, 2001.

[38] N. Polydorides and W. R. B. Lionheart, "A matlab toolkit for three-dimensional electrical impedance tomography: a contribution to the electrical impedance and diffuse optical reconstruction software project," *Measurement Science and Technology*, vol. 13, no. 12, pp. 1871–1883, 2002.

[39] *MATLAB*. www.mathsworks.com, 2007.

[40] P. Hua, E. J.Woo, J. G.Webster, and W. J. Tompkins, "Using compound electrodes in electrical impedance tomography," *IEEE Trans. Biomed. Eng*, vol. 40, pp. 29–34, 1993.

[41] F. Dickin and M. Wang, "Electrical resistance tomography for process applications," *Meas. Sci. Technol.*, vol. 7, pp. 247–260, 1996.

[42] D. G. Gisser, D. Isaacson, and J. C. Newell, "Theory and performance of an adaptive current tomography system," *Clinical Physics and Physiological Measurement*, vol. 9, no. 4A, pp. 35–41, 1988.

[43] D. G. Gisser, D. Isaacson, and J. C. Newel, "Current topics in impedance imaging," *Clinical Physics and Physiological Measurement*, vol. 8, no. 4A, pp. 39–46, 1987.

[44] J. Newell, Y. Peng, P. Edic, R. Blue, H. Jaia, and R. Newell, "Effect of electrode size on impedance images of two- and three-dimensional objects," *Biomedical Engineering, IEEE Transactions on*, vol. 45, no. 4, pp. 531–534, 1998.

[45] K.-S. Cheng, S. J. Simske, D. Isaacson, J. C. Newell, and D. G. Gisser, "Errors due to measuring voltage on current-carrying electrodes in electric current computed tomography," *Biomedical Engineering, IEEE Transactions on*, vol. 37, no. 1, pp. 60–65, 1990.

[46] K. Hollaus, C. Gerstenberger, C. Magele, and H. Hutten, "Accurate reconstruction algorithm of the complex conductivity distribution in three dimensions," *IEEE Transactions on Magnetics*, vol. 40, no. 2, pp. 1144–1147, 2004.

[47] M. Cheney, D. Isaacson, J. C. Newell, S. Simske, and J. Goble, "Noser: An algorithm for solving the inverse conductivity problem," *International Journal of Imaging Systems and Technology*, vol. 2, no. 2, pp. 66–75, 1990.

[48] A. Borsic, *Regularization methods for imaging from elctrical measurements.* PhD thesis, Oxford Brookes University, 2002.

[49] P. J. Vauhkonen, S. A. Vauhkonen, M., and J. P. Kaipio, "Image reconstruction in tree-dimentional electrical impedance tomography," in *Inverse Problems, Design and Optimization Symposium, Rio de Janeiro, Brazil*, (Kuopio), 2004.

[50] T. J. Yorkey and J. G. Webster, "A comparison of impedance tomographic reconstruction algorithms," *Clinical Physics and Physiological Measurement*, vol. 8, no. 4A, pp. 55–62, 1987.

[51] T. J. Yorkey, T. J. Yorkey, J. G. Webster, and W. J. Tompkins, "Comparing reconstruction algorithms for electrical impedance tomography," *IEEE Transactions on Biomedical Engineering*, vol. BME-34, no. 11, pp. 843-852, 1987.

[52] D. C. Barber, "A review of image reconstruction techniques for electrical impedance tomography," *Medical Physics*, vol. 16, no. 2, pp. 162–169, 1989.

[53] P. M. Edic, G. J. Saulnier, H. Jain, and J. C. Newell, "An iterative newton-raphson method to solve the admittivity problem," *IEEE Trans. on Biomedical Enegineering*, vol. 45, no. 7, pp. 899–908, 1998.

[54] P. Hua, P. Hua, E. Woo, J. Webster, and W. Tompkins, "Iterative reconstruction methods using regularization and optimal current patterns in electrical impedance tomography," *Medical Imaging, IEEE Transactions on*, vol. 10, no. 4, pp. 621–628, 1991.

[55] W. R. B. Lionheart, N. polydorides, and A. Borsic, *The reconstruction problem*, ch. 1. Electrical impedance tomography : methods, history and applications, Institute of Physics Pub.,, 2005.

[56] H. Griffiths and Z. Zhang, "A dual-frequency electrical impedance tomography system," *Physics in Medicine and Biology*, vol. 34, no. 10, pp. 1465–1476, 1989.

[57] H. Griffiths and A. Ahmed, "A dual-frequency applied potential tomography technique: computer simulations," *Clinical Physics and Physiological Measurement*, vol. 8, no. 4A, pp. 103–107, 1987.

[58] K. S. Cole and R. H. Cole, "Dispersion and absorption in dielectrics ii. direct current characteristics," *The Journal of Chemical Physics*, vol. 10, no. 2, pp. 98–105, 1942.

[59] P. J. Riu, J. Rosell, A. Lozano, and R. Pallàs-Areny, "A broadband system for multifrequency static imaging in electrical impedance tomography," *Clinical Physics and Physiological Measurement*, vol. 13, no. A, pp. 61–65, 1992.

[60] P. J. Riu, R. Bragos, and J. Rosell, "Broadband quasi-differential multifrequency electrical impedance imaging system," *Physiological Measurement*, vol. 17, no. 4A, pp. A39–A47, 1996.

[61] N. K. Soni, A. Hartov, C. Kogel, S. P. Poplack, and K. D. Paulsen, "Multifrequency electrical impedance tomography of the breast: new clinical results," *Physiological Measurement*, vol. 25, no. 1, pp. 301–314, 2004.

[62] O. Casas, J. Rosell, R. Bragós, A. Lozano, and P. J. Riu, "A parallel broadband real-time system for electrical impedance tomography," *Physiological Measurement*, vol. 17, no. 4A, pp. A1–A6, 1996.

[63] K. Primrose and C. Qiu, "Performance and application studies of an electrical resistance tomography system," in *1st World Congress on Industrial Process Tomography*, 1999.

[64] M. Wang, Y. Ma, N. Holliday, Y. Dai, R. Williams, and G. Lucas, "A high-performance eit system," *Sensors Journal, IEEE*, vol. 5, no. 2, pp. 289–299, 2005.

[65] G. J. Saulnier, *EIT Instrumentation*, ch. 2, pp. 67–104. Electrical impedance tomography : methods, history and applications, Institute of Physics Pub.,, 2005.

[66] Q. S. Zhu, C. N. McLeod, C. W. Denyer, F. J. Lidgey, and W. R. B. Lionheart, "Development of a real-time adaptive current tomograph," *Physiological Measurement*, vol. 15, no. 2A, pp. A37–A43, 1994.

[67] R. Cook, G. Saulnier, D. Gisser, J. Goble, J. Newell, and D. Isaacson, "Act3: a high-speed, high-precision electrical impedance tomograph," *Biomedical Engineering, IEEE Transactions on*, vol. 41, no. 8, pp. 713–722, 1994.

[68] T. E. Kerner, A. Hartov, K. S. Osterman, C. DeLorenzo, and K. D. Paulsen, "An improved data acquisition method for electrical impedance tomography," *Physiological Measurement*, vol. 22, no. 1, pp. 31–38, 2001.

[69] M. Wang, F. J. Dickin, and R. A. Williams, "The grouped node technique as a means of handling large electrode surfaces in electrical impedance tomography," *Physiological Measurement*, vol. 16, no. 3A, pp. A219–A226, 1995.

[70] F. G. Dickin and M. Wang, *Impedance sensors - conducting systems*, ch. 5, pp. 63–84. Process tomography principles , techniques and application, Butterworth–Heinemann, 1995.

[71] D. Jennings and I. D. Schneider, "Front-end architecture for a multifrequency electrical impedance tomography system," *Medical and Biological Engineering and Computing*, vol. 39, pp. 368–374, May 2001.

[72] Analogue Devices, *A Technical Tutorial on Digital Signal Synthesis*, 1999.

[73] L. Cordesses, "Direct digital synthesis: a tool for periodic wave generation (part 1)," *Signal Processing Magazine, IEEE*, vol. 21, no. 4, pp. 50–54, 2004.

[74] L. O. Chua, C. A. Desoer, and E. S. Kuh, *Linear and nonlinear circuits.* New York: McGraw-Hill,, 1987.

[75] B. Blad, K. Lindstrom, L. Bertenstam, B. R. R. Persson, and N. G. Holmer, "A current injecting device for electrical impedance tomography," *Physiological Measurement*, vol. 15, no. 2A, pp. A69–A77, 1994.

[76] C. Denyer, F. Lidgey, Q. Zhu, and C. McLeod, "High output impedance voltage controlled current source for bio-impedance instrumentation," in *Engineering in Medicine and Biology Society, 1993. Proceedings of the 15th Annual International Conference of the IEEE*, pp. 1026–1027, 1993.

[77] C. W. Denyer, F. J. Lidgey, Q. S. Zhu, and C. N. McLeod, "A high output impedance current source," *Physiological Measurement*, vol. 15, no. 2A, pp. A79–A82, 1994.

[78] A. S. Ross, G. J. Saulnier, J. C. Newell, and D. Isaacson, "Current source design for electrical impedance tomography," *Physiological Measurement*, vol. 24, no. 2, pp. 509–516, 2003.

[79] A. J. Wilson, P. Milnes, A. R. Waterworth, R. H. Smallwood, and B. H. Brown, "Mk3.5: a modular, multi-frequency successor to the mk3a eis/eit system," *Physiological Measurement*, vol. 22, no. 1, pp. 49–54, 2001.

[80] Analogue Devices, *AD844 Data Sheet*, 2003.

[81] R. Bragos, J. Rosell, and P. Riu, "A wide-band ac-coupled current source for electrical impedance tomography," *Physiological Measurement*, vol. 15, no. 2A, pp. A91–A99, 1994.

[82] A. Hartov, R. Mazzarese, F. Reiss, T. Kerner, K. Osterman, D. Williams, and K. Paulsen, "A multichannel continuously selectable multifrequency electrical impedance spectroscopy measurement system," *Biomedical Engineering, IEEE Transactions on*, vol. 47, no. 1, pp. 49–58, 2000.

[83] W. Sansen, B. Geeraerts, W. V. Petegem, and M. Steyaert, "Electrical impedance tomography systems based on voltage drive," *Clinical Physics and Physiological Measurement*, vol. 13, no. A, pp. 39–42, 1992.

[84] P. M. Record, "Single-plane multifrequency electrical impedance instrumentation," *Physiological Measurement*, vol. 15, no. 2A, pp. A29–A35, 1994.

[85] B. H. Brown and A. D. Seagar, "The sheffield data collection system," *Clinical Physics and Physiological Measurement*, vol. 8, no. 4A, pp. 91–97, 1987.

[86] K. G. Boone and D. S. Holder, "Current approaches to analogue instrumentation design in electrical impedance tomography," *Physiological Measurement*, vol. 17, no. 4, pp. 229–247, 1996.

[87] R. Smith, I. Freeston, and B. Brown, "Digital demodulator for electrical impedance imaging," in *Engineering in Medicine and Biology Society, 1989. Images of the Twenty-First Century. Proceedings of the Annual International Conference of the IEEE Engineering in*, pp. 1744–1745 vol.6, 1989.

[88] R. W. M. Smith, I. L. Freeston, B. H. Brown, and A. M. Sinton, "Design of a phase-sensitive detector to maximize signal-to-noise ratio in the presence of gaussian wideband noise," *Measurement Science and Technology*, vol. 3, no. 11, pp. 1054–1062, 1992.

[89] S. Gabriel, R. W. Lau, and C. Gabriel, "The dielectric properties of biological tissues: Ii. measurements in the frequency range 10 hz to 20 ghz," *Phys. Med. Biol.*, vol. 41, pp. 2271–2293, 1996.

[90] A. Romsauerova, A. McEwan, L. Horesh, R. Yerworth, R. H. Bayford, and D. S. Holder, "Multi-frequency electrical impedance tomography (eit) of the adult human head: initial findings in brain tumours, arteriovenous malformations and chronic stroke, development of an analysis method and calibration," *Physiological Measurement*, vol. 27, no. 5, pp. S147–S161, 2006.

[91] R. K. Barlow, R. A. Williams, J. Bond, K. T. Oliver, and P. Hunt, "Composition analysis of mixed mineral suspensions using impedance spectroscopy," in *Frontiers in Industrial Process Tomography II*, 1997.

[92] E. Zimmermann, A. Kemna, J. Berwix, and W. Glaas, "Eit measurement system with high phase accuracy for the imaging of spectral induced polarization properties of soils and sediments," in *5th World Congress on Industrial Process Tomography, Bergen, Norway*, pp. 51–58, 2007.

[93] P. Metherall, D. C. Barber, R. H. Smallwood, and B. H. Brown, "Three-dimensional electrical impedance tomography," *Nature*, vol. 380, pp. 509–512, Apr. 1996.

[94] V. Arpinar and B. Eyuboglu, "Microcontroller controlled, multifrequency electrical impedance tomograph," in *Engineering in Medicine and Biology Society, 2001. Proceedings of the 23rd Annual International Conference of the IEEE*, vol. 3, pp. 2289–2291 vol.3, 2001. this paper is a example hardware design using microcontroller.

[95] C. Qiu, B. S. Hoyle, and F. J. W. . Podd, "Engineering and application of a dual-modality process tomography system," *Journal of Flow measurement and Instrumentation* ., vol. 18, pp. 247–254, 2007.

[96] D. Rivera, S. Gaikwad, and X. Chen, "Control-id: a demonstration prototype for control-relevant identification," in *American Control Conference, 1994*, vol. 2, pp. 2055–2059 vol.2, 1994.

[97] E. Van der Ouderaa, J. Schoukens, and J. Renneboog, "Peak factor minimization using a time-frequency domain swapping algorithm," *Instrumentation and Measurement, IEEE Transactions on*, vol. 37, no. 1, pp. 145–147, 1988. Multisin and the problem of minimization of peak factor minimizatiion.

[98] M. Schroeder, "Synthesis of low-peak-factor signals and binary sequences with low autocorrelation (corresp.)," *Information Theory, IEEE Transactions on*, vol. 16, no. 1, pp. 85–89, 1970.

[99] W. Yin, S. J. Dickinson, and A. J. Peyton, "A multi-frequency impedance analysing instrument for eddy current testing," *Measurement Science and Technology*, vol. 17, no. 2, pp. 393–402, 2006.

[100] A. V. Oppenheim, A. S. Willsky, and S. H. Nawab., *Signals and systems*. London :: Prentice-Hall International,, 2nd ed. ed., 1997. Bibliography: p. 778-782.

[101] D. Georgakopoulos, W. Q. Yang, and R. C. Waterfall, "Best value design of electerical tomography systems," in *3rd World Congress on Industrial Process Tomography*, (Banff, Canada), pp. 11–19, 2003.

[102] P. Eykhoff, *System identification parameter and state estimation.* Wiley,, 1974.

[103] L. Ljung, *System identification : theory for the user.* Prentice Hall, 1999. Includes bibliographical references and indexes.

[104] L. Ljung and T. Glad, *Modeling of dynamic systems.* US: Prentice Hall, 1994.

[105] I. Schneider, "Broadband signals for electrical impedance measurements of long bone fractures," in *Engineering in Medicine and Biology Society, 1996. Bridging Disciplines for Biomedicine. Proceedings of the 18th Annual International Conference of the IEEE*, vol. 5, pp. 1934–1935 vol.5, 1996.

[106] C. E. C. E. Cook, *Radar signals : an introduction to theory and application.* New York: Academic Press,, 1967.

[107] Analogue Devices, *AD9852 Data Sheet*, 2005.

[108] S. Mallat, *A wavelet tour of signal processing.* UK: Academic Press, 1998.

[109] L. Cohen, *Time-frequency analysis.* Upper Saddle River, N.J: Prentice Hall PTR,, c1995. Includes bibliographical references and index.

[110] S. Qian and D. Chen., *Joint time-frequency analysis : methods and applications.* Upper Saddle River, N.J. :: Prentice Hall,, c1996. Includes bibliographical references (p. 287-296) and index.

[111] B. Boashash, *Time frequency signal analysis and processing : a comprehensive reference.* Amsterdam ; London: Elsevier, 2003. Includes bibliographical references and index.

[112] C. K. Chui, *Wavelets : a mathematical tool for signal processing / Charles K. Chui.* Philadelphia: SIAM, 1997.

[113] K. Darowicki and P. Slepski, "Influence of the analyzing window on electrode impedance measurement by the continuous frequency scanning method," *Electroanalytical Chemistry*, vol. 533, no. 9, pp. 25–31, 2002.

[114] A. V. Oppenheim and R. W. Schafer., *Discrete-time signal processing.* USA: Prentice Hall, 1989.

[115] R. M. Rao and A. S. Bopardikar, *Wavelet transforms: introduction to theory and application.* Singapore: Pearson Education, 2004.

[116] I. Delprat, "Asymptotic wavelet and gabor analysis: extraction of instantaneous frequencies," *IEEE Trans. Inf. Theory*, vol. 38, no. 2, pp. 644–664, 1992.

[117] A. Teolis, *Computational signal processing with wavelets.* USA: Birkhauser, 1998.

[118] I. Daubechies, "The wavelet transform, time-frequency localization and signal analysis," *Information Theory, IEEE Transactions on*, vol. 36, no. 5, pp. 961–1005, 1990.

[119] J. D. Harrop, S. N. Taraskin, and S. R. Elliott, "Instantaneous frequency and amplitude identification using wavelets: Application to glass structure," *Physical Review E*, vol. 66, 2002.

[120] M. Misiti, Y. Misiti, G. Oppenheim, and J. Poggi, *Matlab wavelet toolbox*, 3 ed., 2004.

[121] D. L. Donoho, "De-noising by soft thresholding," *IEEE Trans. On Inf. Theory*, vol. 41, no. 3, 1995.

[122] B. Brown, "Measurement of the electrical properties of tissue: new developments in impedance imaging and spectroscopy," *IEICE Trans. Inf. & Syst.*, vol. E85-D, no. 1, pp. 2–4, 2002.

[123] D. Q. M. Craig, *Dielectric analysis of pharamaceutical systems.* Taylor & Francis, 1995.

[124] T. Murai and Y. Kagawa, "Electrical impedance copmputed tomography based on afinite elemnet model," *IEEE Trans. on Biomedical Enegineering*, vol. BME-32., no. 3, 1985.

[125] W. R. B. Lionheart, "Eit reconstruction algorithms: pitfalls, challenges and recent developments," *Physiological Measurement*, vol. 25, no. 1, pp. 125–142, 2004.

[126] M. Vetterli and J. Kovacevic, *Wavelets and subband coding.* USA: Prentice Hall, 1995.

[127] O. Casas, R. Bragos, P. J. Riu, and J. Rosell, "Algorithms for parametric images in meit systems," *Physiological Measurement*, vol. 21, no. 1, pp. 35–43, 2000.

[128] A. D. Seagar, D. C. Barber, and B. H. Brown, "Theoretical limits to sensitivity and resolution in impedance imaging," *Clinical Physics and Physiological Measurement*, vol. 8, no. 4A, pp. 13–31, 1987.

[129] P. Riu, J. Rosell, and R. Pall&s-Areny, *Tomographic Techniques for Process Design and Operation*, ch. Multifrequency electrical impedance tomography as an aletrnative to absolute imaging, pp. 53–62. Computational mechanics publications, 1993.

[130] Linear Technology, *LT1228 Data Sheet*, 2006.

[131] P. Denbigh, *System analysis and signal processing : with emphasis on the use of MATLAB / Philip Denbigh.* Addison-Wesley,, 1998.

[132] J. Schlappa, E. Annese, and H. Griffiths, "Systematic errors in multi-frequency eit," *Physiological Measurement*, vol. 21, no. 1, pp. 111–118, 2000.

[133] P. H. G. Allen, "Field mapping with conducting paper," *Physics Education*, vol. 3, pp. 266–272, 1968.

[134] D. R. Stephenson, T. A. York, and R. Mann, "Performance and requirements of process ert instruments," in *5th World Congress on Industrial Process Tomography, Bergen, Norway*, 2007.

[135] D. R. Stephenson, T. A. York, and R. Mann, "Choices and implications in practical eit," in *5th World Congress on Industrial Process Tomography, Bergen, Norway*, 2007.

[136] A. McEwan, G. Cusick, and D. S. Holder, "A review of errors in multi-frequency eit instrumentation," *Physiological Measurement*, vol. 28, no. 7, pp. S197–S215, 2007.